University of Alberta

Low Frequency Plasma Response to Intense Laser Beams

by

Ivan Ourdev

A thesis submitted to the Faculty of Graduate Studies and Research in partial fulfillment of the requirements for the degree of Doctor of Philosophy

Department of Physics

Edmonton, Alberta

Spring 2002

National Library of Canada
Acquisitions and Bibliographic Services
395 Wellington Street
Ottawa ON K1A 0N4
Canada

Bibliothèque nationale du Canada
Acquisitions et services bibliographiques
395, rue Wellington
Ottawa ON K1A 0N4
Canada

Your file Votre référence

Our file Notre référence

The author has granted a non-exclusive licence allowing the National Library of Canada to reproduce, loan, distribute or sell copies of this thesis in microform, paper or electronic formats.

L'auteur a accordé une licence non exclusive permettant à la Bibliothèque nationale du Canada de reproduire, prêter, distribuer ou vendre des copies de cette thèse sous la forme de microfiche/film, de reproduction sur papier ou sur format électronique.

The author retains ownership of the copyright in this thesis. Neither the thesis nor substantial extracts from it may be printed or otherwise reproduced without the author's permission.

L'auteur conserve la propriété du droit d'auteur qui protège cette thèse. Ni la thèse ni des extraits substantiels de celle-ci ne doivent être imprimés ou autrement reproduits sans son autorisation.

0-612-68611-6

Canada

University of Alberta

Library Release Form

NAME OF AUTHOR:	Ivan Ourdev
TITLE OF THESIS:	Low Frequency Plasma Response to Intense Laser Beams
DEGREE:	Doctor of Philosophy
YEAR THIS DEGREE GRANTED:	2002

Permission is hereby granted to the University of Alberta Library to reproduce single copies of this thesis and to lend or sell such copies for private, scholarly or scientific research purposes only.

The author reserves all other publication and other rights in association with the copyright in the thesis, and except as hereinbefore provided neither the thesis nor any substantial portion thereof may be printed or otherwise reproduced in any material form whatever without the author's prior written permission.

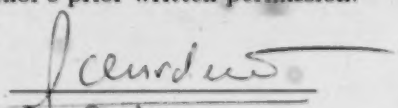

Ivan Ourdev
Suite 305
10610 83th av.
Edmonton Alberta
CANADA T6E 2E2
ivan.ourdev@ualberta.ca

Jan 31, 2002

University of Alberta

Faculty of Graduate Studies and Research

The undersigned certify that they have read, and recommend to the Faculty of Graduate Studies and Research for acceptance, a thesis entitled **Low Frequency Plasma Response to Intense Laser Beams** submitted by **Ivan Ourdev** in partial fulfillment of the requirements for the degree of Doctor of Philosophy.

Wojciech Rozmus (Supervisor)

Andrei Smolyakov (External)

Walter Jones (Chairman)

Faqir Khanna

Richard Sydora

Clarence Capjack

DATE: 21 Dec 2001

Toto, I've a feeling we are not in Kansas anymore.

– Dorothy Gale, *Wizard of Oz*

To my mother

Abstract

Numerical and theoretical studies of laser beam interaction with under-dense plasmas involving ion wave instabilities are presented. The theoretical model that is used involves a realistic distribution of laser intensity and a non-paraxial electromagnetic wave equation coupled to the ion acoustic wave equation in a two-dimensional geometry.

Three different cases of laser beams are considered, a single hot spot beam, a random phase plate (RPP) beam and two crossed RPP beams. In all the three cases, a close connection with the experiment is established.

For the case of a single hot spot beam the stability of laser light filaments in a homogeneous isothermal plasma with respect to coupled electromagnetic and density perturbations is considered. At early times, in addition to the known modulational instability of a guided electromagnetic mode, a new fast growing resonant instability is found. At later times, a weak correlation between backscattered stimulated Brillouin scattering (SBS) reflectivity and filamentation or self-focusing instabilities is established. It is demonstrated that the transmitted light angular spreading and frequency shifts are consistent with near-forward SBS.

In the case of a single RPP beam, the angular divergence and temporal bandwidth are shown to correspond to additional spatial and temporal incoherence in the regime where the average laser intensity exceeds the self-focusing threshold. The transverse and longitudinal sizes of the laser speckles inside the plasma are related in a way that makes it possible to define a local effective beam f-number as a measure of the effective speckle length and for the plasma induced temporal incoherence. The numerical simulations show that the effective f-number decreases as light propagates through plasma.

In the case of two crossed RPP beams a significant nonlinear enhancement of large angle forward scattering is observed. The spectral analysis of the transmit-

ted light shows two components, one of which is unshifted with respect to the initial laser light frequency, and the other is red-shifted. The red-shifted component is found to be strongly enhanced in the case of crossed beam interaction in comparison with that of one beam illumination. The numerical simulations show that this enhancement is due to large angle forward stimulated Brillouin scattering.

Acknowledgements

This thesis is a result of the joint efforts of so many people. I hope I wouldn't miss somebody. First of all I have to acknowledge the support of my family thru hundreds of late nights and weekend of absence and particularly my mother's who was so adamant about getting it finished.

Then I have to thank W. Rozmus for taking me as a graduate student and for being so relentless in his requests for constantly obtaining new results. There are certain things one can only appreciate in a long run.

There are so many brilliant physicists with whom I've worked and from whom I've learned. I can single out only A. Maximov for his immeasurable support both scientifically and as a friend. The others I would rather list alphabetically – A. Shivarova, A. Zelnikov, C. Capjack, D. Pesme, D. Grozev, H. Baldis, V. Tikhonchuk.

Certainly a very big thanx goes to Research Support group – Ron Senda, Wally Lysz, Denise Thornton, Diego Novillo and Roel Van der Goot – always ready to help and willing to make an exception.

Last but not least I would like to thank the members of my committee for catching the numerous grammatical errors, and contributing significantly for the quality of this text.

Preface

The work presented in this dissertation was carried out at the Department of Physics at the University of Alberta, Edmonton between January 1995 and February 2001. The work was done under the supervision of W. Rozmus. The main results have been published in the following articles:

- "Plasma induced smoothing of a spatially incoherent laser beam and reduction of backward stimulated Brillouin scattering", A. V. Maximov, I. G. Ourdev, D. Pesme, W. Rozmus, V. T. Tikhonchuk, and C. E. Capjack, *Phys. Plasmas*, **8**, 2001, 1319.

- "Enhanced forward scattering in the presence of two laser beams", C. Labaune, H. Baldis, E. Schifano, B. S. Bauer, A. Maximov, I. Ourdev, W. Rozmus, and D. Pesme, *Phys. Rev. Letters*, **85**,2000, 1658-1661.

- "Resonant instability of laser filaments in a plasma", D. Pesme, W. Rozmus, V. T. Tikhonchuk, A. Maximov, I. Ourdev, and C. H. Still, *Phys. Rev. Letters*, **84**, 2000, 278-281.

- "Ion wave response to intense laser beams in underdense plasmas", V.Eliseev, I. Ourdev, W.Rozmus, V.Tikhonchuk, C.Capjack and P.Young, *Phys. Plasmas*, **4**, 1997, 4333-4346.

Various aspects of the investigated problems have been presented on the following conferences and workshops and included in the conferences' proceedings:

- "Nonlinear propagation of spatially incoherent laser beam: self-induced smoothing and reduction of scattering instabilities", A. Maximov, I. Ourdev, D. Pesme, W. Rozmus, V. Tikhonchuk, C. Capjack, Ph. Mounaix, L. Divol, and S.Huller, in *Inertial Fusion Sciences and Applications*, 324-330, eds. C. Labaune, W. Hogan, K. Tanaka, Paris, 1999.

- "Interaction of two crossed RPP beams with a plasma", A. Maximov, I. Ourdev, W. Rozmus, D. Pesme, H. Baldis, and C. Labaune, 29^{th} *Annual Anomalous Absorption Conference*, Jun 14-18, 1999, Pacific Grove, California.

- "Self-induced smoothing of spatially incoherent laser beams and reduction of backward stimulated Brillouin scattering", A. Maximov, I. Ourdev, D. Pesme, W. Rozmus, V. Tikhonchuk and C. Capjack, *III-rd International Workshop on Laser Plasma Interaction Physics*, Feb 17-20, 1999, Banff, Canada.

- "Forward scattering as a potential self-smoothing phenomena", H. Baldis, C. Labaune, W. Rozmus, A. Maximov and I. Ourdev, *III-rd International Workshop on Laser Plasma Interaction Physics*, Feb 17-20, 1999, Banff, Canada.

- "Stimulated Brillouin scattering and spatial incoherence of laser beams", I. Ourdev, D. Pesme, W. Rozmus, V. Tikhonchuk and C. Capjack, *III-rd Carolus Magnus Summer School on Plasma Physics*, Sep 8-19, 1997, Spa, Belgium.

- "Numerical simulations of self-induced plasma smoothing of spatially incoherent laser beams", I. Ourdev, D. Pesme, W. Rozmus, V. Tikhonchuk, C. Capjack and R. Senda, *Proceedings of Advanced photonics with second order optically nonlinear processes*, Sept 21 - Oct 3, 1997, Sozopol, Bulgaria.

- "Self-induced plasma smoothing of laser beams", I. Ourdev, D. Pesme, W. Rozmus, V. Tikhonchuk and C. Capjack, *Proceedings of the 39th Annual Meeting of the Division of Plasma Physics of the APS*, Nov 17-21, 1997, Pittsburgh, USA.

- "Smoothing effects of the propagation of a stochastic laser beam in underdense plasmas", I. Ourdev, D. Pesme, W. Rozmus, V. Tikhonchuk and C. Capjack, *Proceedings of the 26th Annual Anomalous Absorption Conference*, 1996.

- "Role of near-forward stimulated Brillouin scattering and filamentation instability in laser-plasma interactions with underdense plasmas", W. Rozmus, V. Eliseev, I. Ourdev, V. Tikhonchuk, C. Capjack and P. Young, *II-nd International Workshop on Laser Plasma Interaction Physics*, Feb 19-22, 1997, Banff, Canada.

- "Simulations of low-frequency plasma response to laser beams with a realistic intensity distribution", V. Eliseev, I. Ourdev, W. Rozmus, V. Tikhonchuk, C. Capjack and P. Young, *II-nd Canadian International Workshop on High-Field Laser Plasma Interaction Physics*, Feb 22-25, 1995, Banff,Canada.

In addition, some of the features of the numerical code ant its modifications were reported in:

- "Spectral method simulations of light scattering by biological cells", Y. Shao, A. V. Maximov, I. G. Ourdev, W. Rozmus, and C. E. Capjack, *submitted to IEEE Journal of Quantum Electronics.*

- "Induced spatial incoherence effects on the stimulated Brillouin scattering", I. Ourdev, D. Pesme, W. Rozmus, V. Tikhonchuk, C. Capjack and R. Senda, *Advanced technologies based on wave and beam generated plasmas*, May 22 - Jun 1, 1998, Sozopol, Bulgaria.

- "Parallel spectral domain decomposition method for simulations of laser-plasma interaction", I. Ourdev, D. Pesme, W. Rozmus, V. Tikhonchuk, C. Capjack and R. Senda, *The 12th Annual International Symposium on*

High Performance Computing Systems and Applications, May 20 - 22, 1998, Edmonton, Alberta, Canada.

List of Symbols and Abbreviations

$2D$	Two-dimensional
$3D$	Three-dimensional
FI	Fillamentation instability
$FWHM$	Full-width half-maximum
NLS	Nonlinear Shröedinger (equation)
ODE	Ordinary differential equation
PDE	Partial differential equation
RPP	Random phase plate
SFI	Self focusing instability
$SPMD$	Single-program multiple-data
SBS	Stimulated Brillouin scattering
α	Particle type: $\alpha = e$ for electrons and $\alpha = i$ for ions
$\mathbf{A}$	Magnetic vector potential
a_{3D}	Waist of hot spot
$\beta = c_s/c$	Dimensionless sound velocity
$\mathbf{B}$	Magnetic field
c	Speed of light
$C_{T,\theta}$	Time correlation function
C_T	Angle correlation function
$c_s = \sqrt{ZT_e/M}$	Ion acoustic velocity
δ	Dirac delta function
e	Electron charge
$\mathbf{E}$	Electric field
E	Amplitude of reflected light
ϕ	Electrostatic potential
F	Focal length
f_α	Distribution function
$\mathbf{F}_p$	Ponderomotive force
G_{hs}	Gain in a hot spot
γ_α	Ratio of specific heats
γ_s	Ion acoustic damping
γ_E	Damping of electromagnetic waves
$\mathbf{J}$	Current density
I_0	Intensity of laser light
$k_D = \sqrt{4\pi n_{e0} e^2/T_e}$	Debye wavenumber
$\mathbf{k}_0$	Wave vector of laser light
$\mathbf{k}_1$	Wave vector of reflected light
$\mathbf{k}_L$	Wave vector of Langmuir waves

$\mathbf{k}_s$	Wave vector of ion acoustic waves
$\lambda_0 = 2\pi/k_0$	Laser wave light in vacuum
$L_R = 2\pi f^2 \lambda_0 \sqrt{1 - n_0/n_c}$	Rayleigh length
m	Mass of electron
M	Mass of ion
M_G	Gaussian abundance function
N	Number of degrees of freedom
n_α	Plasma density
$n_{\alpha 0}$	Background plasma density
$n_c = \sqrt{\omega_0^2 m_e / 4\pi e^2}$	Critical plasma density
$n_{ref} = \sqrt{1 - (n_0/n_c)^2}$	Index of refraction
δn_α	Density fluctuation
ν_{ei}	Electron-ion collision frequency
$\Delta\nu$	Bandwidth
p	Pressure
p_{3D}	Three dimensional self-focusing parameter
P_c	Critical power
q_α	Electric charge
R	Reflectivity
ρ	Charge density
T	Time
T_α	Temperature
T_k	Chebyshev's polynomial
θ_c	Correlation angle
θ_{inc}	Incident light convergence angle
τ_α	Mean collision time
$\tau_c = 1/\Delta\nu$	Coherence time
t_{sf}	Characteristic self-focusing time
$v_g = \omega_{pe}/2k_0 c_s$	Group velocity of electromagnetic wave
$\mathbf{v}_{os} = e\mathbf{A}/mc$	Electron quiver velocity
$v_{T\alpha} = \sqrt{T_\alpha / m_\alpha}$	Thermal velocity
$\mathbf{u}_\alpha$	Ensemble averaged flow velocity
ω_0	Frequency of the laser light
ω_1	Frequency of scattered light
ω_L	Frequency of Langmuir wave
ω_s	Frequency of ion acoustic waves
$\Delta\omega_s = k_0 c_s / f_0$	Ion acoustic waves temporal bandwidth
$\omega_{pe} = \sqrt{4\pi n_{e0} e^2 / m_e}$	Electron plasma frequency
$\omega_{pi} = \omega_{pi}\sqrt{Zm/M}$	Ion plasma frequency
Z	Ion charge number

Contents

1 Introduction 1

Bibliography for Chapter 1 20

2 Basic concepts 27
- 2.1 Theoretical foundations . . . 28
- 2.2 Electromagnetic wave equation . . . 30
- 2.3 Ion-acoustic wave equation . . . 32
- 2.4 Parametric processes . . . 34
  - 2.4.1 Stimulated Brillouin scattering . . . 37
  - 2.4.2 Ponderomotive self-focussing and filamentation . . . 41
- 2.5 Dispersion Relation . . . 44
  - 2.5.1 Stimulated Brillouin scattering . . . 47
  - 2.5.2 Filamentation instability . . . 48
- 2.6 Numerical Code . . . 50
  - 2.6.1 Model Equations . . . 51
  - 2.6.2 Discretization scheme . . . 52
- 2.7 Laser beam characteristics . . . 55

Bibliography for Chapter 2 61

3 Instability of nonlinear filaments 65
- 3.1 Basic equations and stationary solutions . . . 68
- 3.2 Stability analysis of an equilibrium filament . . . 72
- 3.3 Numerical simulations of the filament instability . . . 78

Bibliography for Chapter 3 82

4 Interactions in a single hot spot 84
- 4.1 Laser pump model . . . 87
- 4.2 Simulation plasma parameters . . . 90
- 4.3 Early time behavior . . . 91

4.4 Filamentation instability of the wide laser beam 95
4.5 Near-forward SBS 97
4.6 Late time evolution 99
4.7 Reflected and transmitted light as function of plasma density . . . 105
4.8 Spatio-temporal evolution of near-forward SBS and FI 106
4.8.1 Near-forward stimulated Brillouin scattering 107
4.8.2 Effect of the finite transverse size laser pump 113
4.8.3 Filamentation instability 118

Bibliography for Chapter 4 **121**

5 RPP beam interactions **124**
5.1 Optical smoothing techniques 127
5.2 RPP pump model 130
5.3 Parameters of the model 133
5.4 Spatial and temporal incoherence 135
5.5 Laser beam effective f-number 138
5.6 Beam angular spreading 140
5.7 Hot spot statistics 142
5.8 Random Phase Approximation 144
5.9 Spectral shift of the transmitted light 148
5.10 Reduction of backward SBS 155

Bibliography for Chapter 5 **158**

6 Two crossed RPP beams **161**
6.1 Crossed beams in experiments 163
6.2 Pump model 164
6.3 Evolution in time 168
6.4 Frequency spectra of transmitted light 172
6.5 Density fluctuation spectra 175
6.6 Crossed beams with different wavelengths 176
6.6.1 Beams with equal intensities 178
6.6.2 Beams with different intensities 181

Bibliography for Chapter 6 **184**

7 Summary and conclusions **187**

List of Figures

1.1 Schematic diagram of an ignition capsule. The sizes are typical for a NIF design for a 1.3 MJ total energy laser. 3

1.2 Inertial confinement fusion schemes: (a) direct drive, (b) indirect drive. 5

1.3 Principle of smoothing by overlapping speckle patterns by spectral dispersion. Different copies of the pattern are shifted in space, so that the peaks of some fill the valleys of others resulting in a smooth profile when averaged in time. 9

1.4 Effect of overlapping a large number of pattern realizations. The nonuniformity varies with the number of overlapped realizations N as $1/\sqrt{N}$. 10

1.5 Schematic plot of the ISI concept in 2D. The echelon splits the broadband laser beam of coherence time t_c into mutually incoherent beamlets introducing time delays $t_k - t_{k-1}$. The beamlets are focused onto the target producing a smooth time averaged profile for times $\gg t_c$. 11

1.6 Schematic diagram of a polarization smoothing using a wedge of birefringent material. The laser beam is split equally into two beamlets with orthogonal polarizations, which are deflected by the wedge at slightly different angles resulting in two shifted patterns at the focal plane. 13

1.7 Scattering processes: (a) scattering of wave by particle, (b) scattering with emission of an intermediate wave. 14

1.8 Diagram of the operation regions for different parametric instabilities. Shown as points are the TPD and the oscillating two-stream instability (OTS). 15

2.1 Intensity contour plots for a single Gaussian beam at different moments in time: $T = 0$ (a) and $T = 7ps$ (b). Parameters of the run are $I_0 = 1.46 \times 10^{15} W/cm^2, n_e/n_c = 0.4, f_\# = 4$. 35

2.2 Schematic representation of the stimulated Brillouin scattering process. 38

2.3 Frequency and wave vector matching conditions for the stimulated Brillouin scattering process. 39
2.4 Polar plot of the stimulated Brillouin scattering process. 39
2.5 Polar plot of the stimulated Brillouin scattering growth rate as a function of scattering angle. 40
2.6 Sequence of events comprising ponderomotive self-focussing. Here δI is the nonuniform intensity of the electromagnetic field, $\mathbf{F}_p$ is the ponderomotive force and δn_e is the change in plasma density. 41
2.7 Typical experimental intensity cross section profile of filament driving beam. Reprinted from H. A. Baldis [5]. 42
2.8 Comparison between self-focusing, (a), and filamentation, (b). Intensity contour plots for a single Gaussian beam at different moments in time: $T = 0$ (a) and $T = 7ps$ (b). Parameters of the run are $I_0 = 1.46 \times 10^{15} W/cm^2, n_e/n_c = 0.4, f_\# = 4$. 43
2.9 Schematic representation of the filamentation process. 44
2.10 Geometry of the computational box used for the numerical calculations. 54
2.11 Basic optical processing system. 57
2.12 Focusing of light by a lens of aperture L and focal length F. . . . 60

3.1 Dependence of beam waist a_{eq} from the P/P_{cr}. 72
3.2 Dependence of eigenvalue λ on P/P_{cr}. 73
3.3 a) Dependence of the excited level λ_1 in the filament and the coupling coefficient B (magnified 10 times) for the resonance instability on the filament power, P/P_c. b) Radial profile of the eigenfunction of the excited state $m = 1$ for $P/P_c = 4.24$. 76
3.4 Intensity contours and angular distributions of transmitted light at different times: (a) 14.5 ps, (b) 18.2 ps, (c) 21.8 ps. At time t=0 ps the 1 μm Gaussian beam has been focussed in the center of the simulation box $100 \times 160\,\mu m^2$ with maximum intensity 1.46×10^{15} W/cm^2 and FWHM 6 μm. The background plasma parameters are: $n_0/n_c = 0.4$ and $T_e = 1$ keV. 79
3.5 Frequency spectrum of the transmitted light, which has been calculated within the window of 6 ps at different moments of time. Frequency is given in units of $k_0 c_s = 1$ ps^{-1} which corresponds to the wavelength shift of 0.57 nm. 81

4.1 Circular focus, a) intensity cross section at best focus position at the initial moment in time and b) intensity contour plot at the initial moment in time. The figure on the left shows a comparison between the experimental measurements (small circles) and the theoretical distribution (solid line) used in simulations. 88
4.2 Line focus, a) intensity cross section at best focus position at the initial moment in time. Shows a comparison between the experimental measurements (small circles) and the theoretical distribution (solid line) used in simulations. 88
4.3 Circular focus – a comparison between the measured FWHM spot diameter as a function of the axial position (circles and dashed line) and the theoretical calculations (solid line) based on Eq. (4.1). 89
4.4 Circular focus – typical time dependence of backward SBS reflectivity. The parameters of the run are $I_0 = 1.7\times10^{15}W/cm^2, n_e/n_c = 0.1$. 91
4.5 Circular focus – contour plot of the near field intensity distribution at $t = 10ps$. 92
4.6 Circular focus – density cross section at best focus position at $t = 10ps$. 93
4.7 Near field intensity distribution along the axis of the laser beam propagation at different time moments: (a) $20ps$, (b) $30ps$, (c) $40ps$. 94
4.8 Far field angular distribution of (a) transmitted light at $t = 10ps$ (solid line) and at $t = 0ps$ (dashed line), and (b) reflected light at $t = 10ps$ for the parameters of Fig.(4.4). 96
4.9 Circular focus – far field angular distribution of the transmitted light at $t = 28ps$ (a) and $t = 50ps$ (b) for the parameters of Fig. (4.4). 98
4.10 Line focus – far field angular distribution of the transmitted light at $t = 10ps$ (a) and $t = 28ps$ (b) for the parameters of Fig. (4.4). . 98
4.11 Circular focus – frequency spectra of the transmitted light propagating at different angles from the direction of the laser pump (dotted line) for the parameters of Fig. (4.4). The spectra have been calculated by taking Fourier transform of the data collected over the duration of the run, i.e. $\sim 100ps$ 100
4.12 Circular focus – near field intensity(a) and density (b) distributions at $t = 100ps$ for the parameters of Fig. (4.4). 101
4.13 Circular focus – far field angular distribution of the transmitted and reflected light at $t = 100ps$ for the parameters of Fig. (4.4). . 102
4.14 Line focus – near field intensity(a) and density (b) distributions at $t = 50ps$ for the parameters of Fig. (4.4). 104
4.15 Line focus – far field angular distribution of the transmitted and reflected light at $t = 100ps$ for the parameters of Fig. (4.4). 105

4.16 Circular focus – transmitted and reflected light integrated within the 14° cone as a function of density for intensity $I_0 = 1.7 \times 10^{15} W/cm^2$. 106

4.17 Characteristic regimes of the linear evolution of the near-forward SBS, based on Eq. (4.19) and Eq. (4.20), shown for two sets of parameters: (a) $I = 1.7 \times 10^{15} W/cm^2$,$n_e/n_c = 0.2$, $l = 100\mu m$, (b) $I = 5 \times 10^{16} W/cm^2$,$n_e/n_c = 0.05$, $l = 100\mu m$. Dashed lines show the time when the instability reaches the strongly driven SBS threshold, lines 2 show the transition time between the weakly and strongly driven SBS, and lines 1 display possible saturation time, due to the convection of sound waves in transverse direction. . . . 110

4.18 Comparison between the normalized spectra, calculated fromEq. (4.15) for strongly driven SBS (line 1) for $I = 1 \times 10^{16} W/cm^2$, $n_e/n_c = 0.2$, and for weakly driven SBS (line 2) for $I = 2 \times 10^{15} W/cm^2$, $n_e/n_c = 0.2$. The frequency is normalize to $\omega_2 = 2k_0 c_s \sin\theta/2$. . . 111

4.19 Experimental frequency spectrum at $\theta = 23°$ for the laser peak intensity $I = 5 \times 10^{16} W/cm^2$,$n_e/n_c = 0.2$ and peak plasma density is $0.28 n_c$. 112

4.20 Comparison between the simulations results (small circles) and analytical results (solid line), based on Eq. (4.29) for circular focus (a) and line focus (b). The transmitted light propagates at 20^0 off the forward direction. Parameters are $I = 1.7 \times 10^{15} W/cm^2$, $n_e/n_c = 0.2$. 115

4.21 Results of the SBS gain calculations from Fig. (4.20) for different angles, shown for circular focus (a) and line focus (b). The parameters are as in Fig.(4.20). 116

4.22 Circular focus. Results of the linear theory calculations of the near-forward SBS gain Eq. (4.29)) as a function of deflection angle for different densities (a): n_e/n_c : (1)0.1, (2)0.2, (3)0.3, for intensity $I = 1.7 \times 10^{15} W/cm^2$ at time $t = 50ps$ Similar gain calculations for different laser intensities (b): I : (1)$1.7 \times 10^{15} W/cm^2$, (2)$5 \times 10^{15} W/cm^2$, (3)$10 \times 10^{15} W/cm^2$. for density $n_e/n_c = 0.05$. . 117

4.23 Characteristic regimes of the linear evolution of FI based on Eq. (4.34) and Eq. (4.35), shown for two sets of parameters: (a) $I = 1.7 \times 10^{15} W/cm^2$, $n_e/n_c = 0.2$, $L = 100\mu m$, (b) $I = 5 \times 10^{16} W/cm^2$, $n_e/n_c = 0.05$, $L = 100\mu m$. The dashed line define thresholds, $\sigma_i t = 1, (i = 1, 2)$. Line 1 shows the time, defined by the relation $\sigma_2(t)t = k_s L$, when the FI growth reaches maximum defined by a stationary gain. Line 2 indicates the transition time between the regimes of strong and weak coupling. 120

5.1 Typical contour plot of the intensity of the laser beam. Definition of the hot spot sizes. 125
5.2 Typical intensity cross section at best focus position,(a), and intensity contour plot of part of the computational box,(b), at $T = 0ps$. Parameters of the run are $f_{\#} = 4$, $I_0 = 0.85 \times 10^{15} W/cm^2$, $n_e/n_c = 0.1$. 129
5.3 Random phase plate configuration. 132
5.4 Angle correlation function of the transmitted light propagating at angle $\theta = 10°$ for three time intervals with the interval center at $T = 33$ ps (solid line), 66 ps (dashed line), 100 ps (dotted line); the averaging time interval $\Delta t = 27$ ps, the average beam intensity 0.7×10^{15} W/cm^2. 137
5.5 Time correlation function of the transmitted light propagating at angle $\theta = 10°$ (a) and angle $\theta = 0°$ (b) for three time intervals with the interval center at $T = 33$ ps (solid line), 66 ps (dashed line), and 100 ps (dotted line); the averaging time interval $\Delta t = 27$ ps, the average beam intensity 0.7×10^{15} W/cm^2. 138
5.6 Variation of the laser RPP beam effective beam f-numbers $f_{\perp}$ (dashed line) and $f_{\parallel}$(solid line) in time for the average beam intensity 0.7×10^{15} W/cm^2. 139
5.7 The distribution of laser field intensity at time 50 ps for the average beam intensity 0.6×10^{15} W/cm^2. 140
5.8 Dependence of the angular width of the transmitted light $< \theta >$ at time $T = 70ps$ on the average intensity of the incident beam. . 141
5.9 Typical evolution of beam spreading in different moments of time: (a) 14ps, (b) 58ps, (c)116, (c) 211ps. The average beam intensity is 0.7×10^{15} W/cm^2. 143
5.10 Variation of the laser RPP beam parameters in time for the average beam intensity 0.7×10^{15} W/cm^2: (a) angular width of the transmitted light; (b) fraction of the incident beam power: transmitted (dashed line), transmitted into incident beam convergence angle (dotted line), and reflected (solid line); 144
5.11 Normalized abundance of hot spots $M(I)/M(2\langle I \rangle)$ versus hot spot maximum intensity for the average beam intensity 0.7×10^{15} W/cm^2 at time 70 ps in the simulations (solid line) compared to the theoretical formula for the Gaussian speckle statistics $M_G(I)$ (dashed line). 145
5.12 The frequency spectrum of transmitted light as a function of time and frequency ω_t for: (a) all scattering angles θ, (b), $|\theta| \leq 10°$. The averaging time interval is 35 ps. The average beam intensity is 0.7×10^{15} W/cm^2. 150

5.13 The frequency spectrum of transmitted light as a function of time and frequency ω_t for: (c) $10° < |\theta| < 20°$, (d), $|\theta| \geq 20°$. The averaging time interval is 35 ps. The average beam intensity is 0.7×10^{15} W/cm^2. 151
5.14 Angular dependence of the frequency shift of transmitted light for $P/P_{cr} = 1.2$ and 1.7 compared with the linear theory result $\omega_l(\theta)$ (dashed line). 154

6.1 Time-resolved spectra of the transmitted light collected in the experiment by the optics located along the direction of beam 1, when both beams, 1 and 2, have equal average intensities. 165
6.2 Layout of the interaction region between beam 1 and beam 2. . . 166
6.3 Intensity cross sections and the corresponding intensity contour plots of the crossed RPP beams at time $T = 0$ for (a) beam 1, (b) beam 2 and (c) sum of beam 1 plus beam 2. 167
6.4 Time profile of the laser beam intensity imposed on the left boundary of the computational box, $x = 0$. 168
6.5 Typical evolution of beams spreading in different moments of time: (a) 0ps, (b) 102ps, (c)205ps, (d) 300ps. The two laser beams have equal average beam intensity of $I = 5.4 \times 10^{13} W/cm^2$ and $f = 6$; $n/n_c = 0.3$. 169
6.6 Time evolution of crossed beams with equal intensities, (a) transmitted and reflected light for beam 1 (solid line) and beam 2 (dotted line), (b) change of the angle between the beams, (c) beams angular width. The parameters of the run are the same as in Fig. (6.5). 171
6.7 Frequency spectra of the transmitted light obtained from the simulations for two equal intensity crossed beams. The parameters of the run are T_e =0.5 keV and n_e =0.3n_c. 173
6.8 Frequency spectra of the transmitted light obtained from the simulations for a single beam interaction and the same parameters as in Fig.(6.7). 174
6.9 Density fluctuation spectra at early time (a) corresponding to the moment of time of cuts 1 in Figs. (6.1) and (6.7). (b) corresponds to the late time moment of cuts 3 in the same figures. 177
6.10 Time evolution of crossed beams with equal intensities and different frequencies, (a) transmitted and reflected light for beam 1 (solid line and beam 2 (dotted line), (b) change of the angle between the beams, (c) beams angular width. The parameters of the run are the same as in Fig. (6.5) the frequency of beam 1 is 0.6 of the frequency of beam 2. 179

6.11 Frequency spectrum of the transmitted light in the case of crossed beams with equal intensities and $\omega_1 = 0.6\omega_2$. 180
6.12 Time evolution of crossed beams with different frequencies. (a) transmitted and reflected light for beam 1 (solid line and beam 2 (dotted line), (b) change of the angle between the beams, (c) beams angular width. The parameters of the run are $I_1 = 2 \times 10^{14} W/cm^2$, $I_2 = 0.1I_1$, $f = 4$, $n/n_c = 0.1$, $\omega_1 = 0.6\omega_2$. 182
6.13 Frequency spectrum of the transmitted light for the case of beams with different intensities and different frequencies. The parameters of the run are as in Fig. (6.12). 183

Chapter 1

Introduction

Plasma physics is the study of the collective processes in many-body charged particle systems interacting via long-range Coulomb force. The discipline includes areas as diverse as low-temperature plasmas, non-neutral plasmas, inertial and magnetic confinement fusion, space and astrophysical plasmas, beams and accelerators. The physical processes include wave-particle interactions, plasma heating, chaos, turbulence, transport and parametric instabilities to name just a few. The mathematical foundation of plasma physics is based upon the Liouville equations for the electron and ion distribution functions in a multidimensional phase space and Maxwell's equations describing electromagnetic fields, which originate from the source terms given by moments of the distribution functions.

Plasma theory has a well developed mathematical apparatus for analytical description of various plasma configurations and relatively complex interactions. However, the accurate study of highly nonlinear processes has become possible only via the application of *numerical simulations*. The progress in this area has mainly been a result of the revolutionary developments in computer hardware leading to the advent of powerful computer architectures (workstations, supercomputers, clusters) that have high computational speed and large memory at relatively low cost. The ongoing hardware evolution is coupled with marked advances in software development, involving the creation of new computer lan-

guages, development tools (such as fast compilers, debuggers and profilers), parallel design and visualization applications. Part of this general trend has been the development of advanced numerical techniques, such as high fidelity discretization schemes, efficient memory management, fast algorithms, vector and parallel processing. The primary investigation tool in this work has been large scale parallel computer simulations.

Much of the motivation for this study is based on experiments related to the *inertial confinement fusion* (ICF) program. ICF is one of the possible ways of obtaining energy from the reactions between light nuclei (fusion reactions). When the sum of the masses of those nuclei exceeds the mass of the resultant nucleus by an amount of Δm, the released energy W is given by Einstein's relation

$$W = \Delta m c^2,$$

and is of the order of few MeV per nucleon. For such a reaction to take place, the nuclei have to be compressed within the range of nuclear forces, overcoming the Coulomb barrier. This means that the reacting particles have to be confined at high density for sufficiently long time, so that the energy transfer between the nuclei can take place. The temperature required for barrier penetration is in the range of keV. At such temperatures the matter is completely ionized and is in the form of a gas of positively charged nuclei and an equivalent number of electrons, i.e. plasma.

The basic criterion for building a fusion power generator was established by Lawson and states that the product of the number of reacting nuclei per cm^3 and the time τ in seconds has to be greater that a critical number $(n\tau)_{crit}$ [30].

The principle of ICF is based on heating and compressing a pellet of thermonuclear fuel by laser or particle beams and using the fuel mass inertia to provide confinement. Figure (1.1) shows a schematic diagram of an ignition capsule

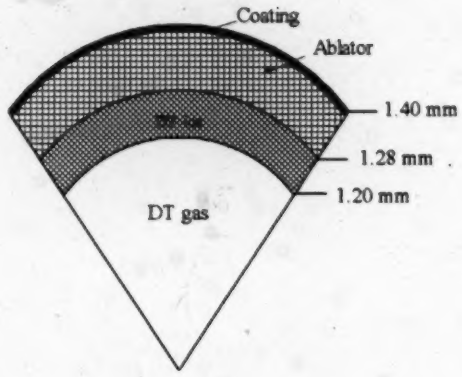

Figure 1.1: Schematic diagram of an ignition capsule. The sizes are typical for a NIF design for a 1.3 MJ total energy laser.

with sizes typical for a National Ignition Facility (NIF) * design [7]. The capsule is typically a spherical shell filled with low density deuterium-tritium (DT) gas. The shell consists of an outer part, called an ablator, which is sometimes covered with a coating, and an inner part of frozen or liquid deuterium-tritium that forms the main fuel. The fuel is usually made of deuterium-tritium because of its high energy gain

$$D + T \rightarrow He^4(3.52MeV) + n(14.06MeV),$$

which yields released total energy, $E_{tot} = 17.58MeV$.

The intense laser light energy couples to the surface of the target and heats the ablator. Part of the light is absorbed and evaporates the pellet surface, forming a rapidly expanding plasma corona. There is an additional evaporation due to heat transfer to the pellet. This process is called *ablation*. It results in a shock wave launched into the pellet and its producing fast compression. As the ablator expands outward, the inner part of the target implodes inward. During the compression process, the kinetic energy of implosion is converted into internal

*National Ignition Facility [38] is currently being built at the Lawrence Livermore National Laboratory with a nominal laser energy of $1.8MJ$ and is expected to achieve ignition in both direct and indirect drive configurations.

thermal energy of the high density fuel and the target is compressed to conditions of density and temperature, high enough to trigger fusion reactions. One of the most important characteristics of the implosion process is the so called in-flight aspect ratio (IFAR), defined as the ratio of the shell radius R as it implodes to shell thickness ΔR. To amplify the externally applied ablative pressure, a high IFAR shell is required. If a shell of initial radius R_0 is uniformly accelerated at g to radius $R_0/2$ by an ablation pressure P_A it has a velocity [40]

$$v_{sh}^2 = \frac{P_A R_0}{\rho_{sh} \Delta R}.$$

The final pressure of the fuel is then given by

$$P \approx \rho_{sh} v_{sh}^2 = P_A \frac{R_0}{\Delta R}.$$

This formula shows that indeed a high IFAR is required to achieve the desired high fuel pressure. At the same time, as we shall see below, the situation in which a low density ablation fluid accelerates a heavy shell fluid is susceptible to hydrodynamic instabilities, such as Rayleigh-Taylor (RT) instability and so places an upper limit on the IFAR.

There are two main schemes for laser fusion – direct drive and indirect drive. In the *direct drive* [4], shown schematically in Fig.(1.2)(a), the laser beam(s) are aimed directly at the target. The laser energy is transferred to electrons via inverse bremsstrahlung or different collective plasma processes. In the *indirect drive* [30], shown in Fig.(1.2)(b), the laser energy is first absorbed in a high-Z enclosure, called an *hohlraum*, which emits X-rays driving the target implosion. In general the hohlraums have an elongated shape, designed to compensate for the absence of X-ray emissions from the laser entrance holes

The conversion of laser energy to energy of compression and heating is a complicated process, involving emission and absorption of light by the inhomogeneous plasma surrounding the pellet. Light emission is an energy loss process

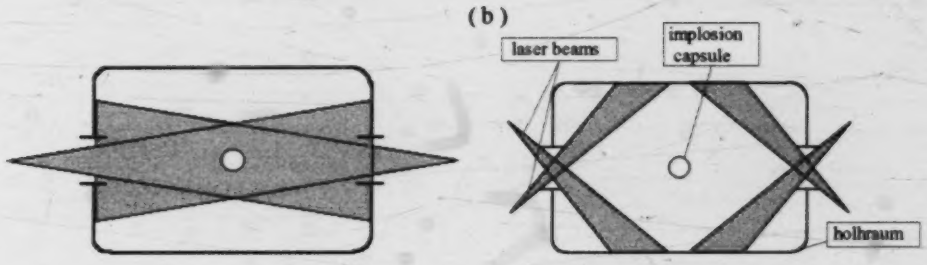

Figure 1.2: Inertial confinement fusion schemes: (a) direct drive, (b) indirect drive.

that occurs in the form of *bremsstrahlung*. This is a continuous radiation emitted by the electrons as a result of their deflection by the Coulomb field of other charged particles. The inverse process results in light absorption and is called *inverse bremsstrahlung*. For laser energy density that is low compared to the thermal energy density, the absorbed fraction of the laser light is proportional to the laser intensity. For higher intensities this linear relation is no longer valid because of the effects of parametric instabilities, such as stimulated Brillouin scattering (SBS), stimulated Raman scattering (SRS) and filamentation, to be reviewed in greater detail below.

One of the actively studied topics in laser plasma interaction physics deals with the reduction of the parametric instabilities by introducing a spatial and temporal incoherence in the laser beams. *Spatial incoherence*, can be viewed as a result of the spread in angle of the wave vectors, $\mathbf{k}_0$, of the incident light. In this case all the wave vectors have the same length. In the case of only *temporal incoherence* all the wave vectors have the same direction, but their lengths are spread over an interval $\Delta k_0 = \Delta\omega_0/V_{g0}$, where $\Delta\omega_0$ is the frequency bandwidth and V_{g0} is the group velocity of the laser light.

The method of induced laser beam incoherence is also used to improve the uniformity of the laser illumination, which affects both the laser-plasma coupling and the symmetry of target implosion. Highly uniform irradiation of the surface

of the fuel-filled capsules is one of the most important prerequisites for efficient energy transfer and consequently – a successful ICF implosion. Intensity non-uniformities can produce ablation pressure variations resulting in an asymmetric implosion and possible failure of the target. For indirect drive ICF the problem is somewhat reduced because the target is illuminated by a "bath" of X-rays emitted from the hohlraum. One disadvantage of this technique is the relatively low conversion efficiency of the laser light to X-rays absorbed by the pellet, resulting in a lower overall gain.

There are several sources of asymmetry, such as imperfections in target fabrication, individual laser irradiation nonuniformity and nonuniformity as a result of errors in beam pointing, focusing and power balance in multi-beam systems. It has been shown [43, 34] that the illumination nonuniformity of multiple beam systems [42, 5] can be decomposed into a single beam factor and a geometrical factor for each mode. Thus, most of the effort is directed towards achieving a smooth focal intensity distribution of individual laser beams. Irradiation non-uniformities can imprint themselves onto the target, thereby seeding the Rayleigh-Taylor instability during the acceleration phase [21]. This is especially important early in the pulse when the target has not yet developed the large blow-off plasma that helps smooth the spatial non-uniformities by thermal diffusion [12]. This instability can be reduced by preheating of the fuel, but the preheat reduces the efficiency of the thermonuclear burn and thus the target gain. Alternatively, it has been found that the perturbation level from the initial shock can be reduced by multiple wavelength lasers and shallow angles of incidence [11].

To introduce the Rayleigh-Taylor instability let us consider an initial perturbation of wavelength λ, at the interface of a dense fluid of density ρ_{hi}, on top of a lighter fluid of density ρ_{lo}. Ignoring finite thickness effects, the exponential

growth rate of RT instability of an interface perturbation is given by

$$\gamma_{RT} = \sqrt{Akg},$$

where $k = 2\pi/\lambda$ is the wave number of the perturbation, g is the acceleration and A is the Atwood number given by $(\rho_{hi}-\rho_{lo})/(\rho_{hi}+\rho_{lo})$. For a spherical implosion, the normal modes are spherical harmonics and for large mode number, l, we can substitute k with l/R. Thus, the higher the mode number, the larger the growth rate of the instability. However, the very large mode numbers saturate before breaking through the shell of the pellet. As a result the most damaging modes are those with wavelengths comparable to the shell thickness, ΔR. So, the number of e-foldings of the classical growth factor is

$$n = \int \gamma_{RT} dt \approx \sqrt{R_0/\Delta R},$$

i.e. large IFAR leads to large RT growth. To reduce the growth of the most dangerous RT modes various pellet designs are implemented that minimize the IFAR and achieve high gain, using foam ablators and/or shock and radiation preheat [4, 51, 52, 10, 11].

The instability can be stabilized by the process of ablative acceleration in which the ablation "burns-off" the perturbations [30, 21]. This reduces the net growth of RT instability by a factor of kv_A, where v_A is the velocity of the flow across the interface.

Various techniques for beam smoothing that employ incoherence have been developed. In most laser-plasma experiments of interest to ICF, laser beams are phase converted by being passed through *random phase plates* (RPP) [19]. RPP are transparent plates divided into a large number of identical area elements, each adding a random phase delay to the transmitted light. This random distribution of phase delays splits the beam into spatially incoherent beamlets, which in the focal region have a typical diameter of $2\lambda f/D$ and a length along

the direction of propagation of $4\lambda f^2/D^2$, where D is the laser beam diameter, f is the focal distance and λ is the wavelength. The resulting irradiation pattern consists of many spots of higher intensity, called speckles or hot-spots and is determined by the shape and size of the individual phase-plate elements. The mutual interference between the beamlets results in an intensity profile, with a speckle modulation smoother than found from a beam without RPP, where strong short-range spatial correlations in the beam phase profile lead to strong long-scale structure in the intensity pattern. The intensity distribution $I(x, y)$ in the focal plane has an envelope function given by the square of the *sinc* function. The zeroth-order diffraction square bounded by $x_0, y_0 = \pm\lambda f/d$ contains 84% of the laser energy, where d is the length of phase element of the phase plate. The intensity fluctuations are averaged along the direction of laser beam propagation as a result of the finite lengths of the beamlets. Also, for spherical targets, a significant uniformity is attainable as a result of lateral smoothing, even though the intensity pattern is stationary in time.

However a RPP produced intensity structure remains stationary during the whole pulse duration so that the intensity contrast is high. In dynamical approaches to laser beam smoothing the speckle location changes during a time which is shorter than the plasma response time. The most direct application of this approach is to keep the RPP and use a broadband pulse with modulated phase coupled with a disperser [44], which will be reviewed below. A drawback of this technique is the energy loss through diffraction by the elementary plate elements and the strong intensity modulation of the electric field, forbidding the use of any optics between the RPP and the target. One additional drawback is that the intensity profile is essentially restricted to the central maximum of the envelope profile [cf. Fig.(1.4)]. As long as it has the shape of an Airy function the energy content is limited to 84%. To overcome this limitation a method of

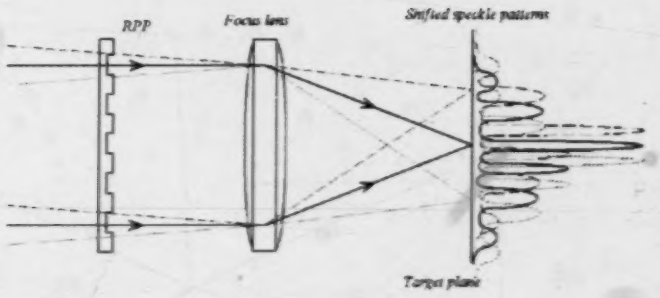

Figure 1.3: Principle of smoothing by overlapping speckle patterns by spectral dispersion. Different copies of the pattern are shifted in space, so that the peaks of some fill the valleys of others resulting in a smooth profile when averaged in time.

continuous phase screen has been designed and is called *kinoform phase plates* (KPP), which produces arbitrary shaped far-field profiles with high efficiency [8, 9].

To eliminate the intensity fluctuations, produced by the interference between rays originating from different phase-plate elements, a combination of a phase plate and a polarization rotator, called *zero correlation mask* (ZCM) is sometimes used [45]. The phase plate in this case is an array of non-randomly distributed binary phase elements that break up the spatial coherence of the laser by imposing discrete phase delays, chosen to yield a zero autocorrelation function for all spatial wavelengths. The polarization plate rotates the polarization across half the beam and so eliminates the interference between half of the phase elements, so that the intensities from each half add incoherently on the focal plane. The method requires highly uniform laser beams, because phase aberrations introduce far field intensity modulations. However the remaining speckle nonuniformity is still bigger than the maximum allowable level for ICF, which in terms of ablation pressure nonuniformity is $1\% - 2\% rms$.

To achieve a high degree of irradiation uniformity, smoothing by overlapping different speckle patterns is usually employed. It relies on the observation that

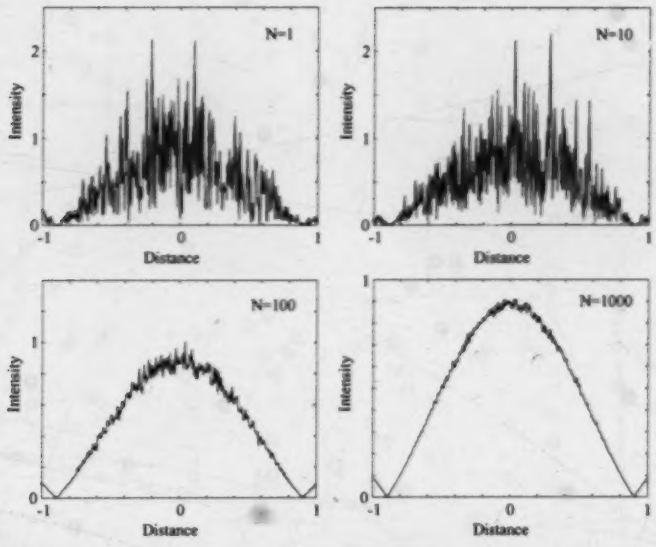

Figure 1.4: Effect of overlapping a large number of pattern realizations. The nonuniformity varies with the number of overlapped realizations N as $1/\sqrt{N}$.

any effect that causes changes in the irradiation intensity distribution will bring a reduction of the effective irradiation nonuniformity by time averaging. Figure (1.3) illustrates the principle of smoothing by overlapping speckle patterns by spectral dispersion. Different copies of the pattern are shifted in space, so that the peaks of some fill the valleys of others resulting in a smooth profile when averaged in time. The approach is statistical in nature so the overlap of N random speckle patterns reduces the root-mean-square (rms) nonuniformity σ_{rms} by $1/\sqrt{N}$. Figures (1.4)(b),(c) and (d) show time averaged intensity profiles, obtained by overlapping 10, 100 and 1000 speckle patterns respectively. The initial rms nonuniformity $\sigma_{rms} = \sigma_0 = 100\%$, Fig.(1.4)(a), is reduced to 10% in the second case, Fig.(1.4)(b), and 3% for the last case, Fig.(1.4)(c).

A number of schemes have been developed that cause the irradiation pattern to change rapidly in time so that its effect on the plasma will average out in time. The *induced spatial incoherence* (ISI) was the first beam smoothing technique of

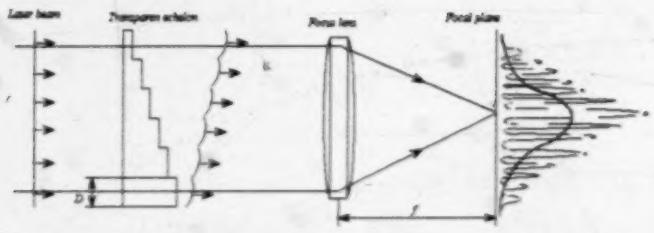

Figure 1.5: Schematic plot of the ISI concept in 2D. The echelon splits the broadband laser beam of coherence time t_c into mutually incoherent beamlets introducing time delays $t_k - t_{k-1}$. The beamlets are focused onto the target producing a smooth time averaged profile for times $\gg t_c$.

this type to be developed. The ISI concept in its conventional (far-field) [25, 26] version is illustrated in Fig.(1.5). A broadband laser beam (bandwidth $\Delta\nu \gg 1/t_{pulse}$ is passed through an echelon structure, which imposes different optical delays upon different transverse sections of the beam. If the delay increments $\Delta t = t_k - t_{k-1}$ are bigger than the optical coherence time $t_c = 1/\Delta\nu$. The beam is thus sliced into a large number of mutually incoherent beamlets. At the focal plane they overlap, producing a complicated interference pattern, modulated by a smooth envelope. On time scales larger than the coherence time t_c, the interference pattern averages out, leaving only the smooth diffraction envelope. If the hydrodynamic response time of the target, t_h, is such that $t_h \gg t_c$, the rapidly changing interference pattern will effectively be ignored.

These techniques, when applied to gas lasers are usually called *partially coherent light* (PCL) techniques. In this approach the spatial coherence of the laser light is altered at the front end of the laser, before the beam is injected into the main amplifying chain. The reduction of the beam coherence in the front end of the laser minimizes the risk of self-focusing responsible for the formation of high frequency spatial modulations.

The experiments [50] and theoretical analysis [28] showed, though, that nonlinear optical effects can distort the envelope of the focal spot profile, even at

low power. The distortion involves "scraping" of the laser pulse and subsequent appearance of a wide low-level pedestal in the light spectrum. Thus the amplification of partially incoherent light in large, high-power glass lasers is likely to be limited by a combination of nonlinear effects such as self-focusing, self-phase modulation and two-plasmon decay. The limit was found to result mainly from the spatial incoherence (extended source), rather than from the temporal incoherence (spectral bandwidth). This is the reason that the ISI/PCL approach was discarded as a smoothing technique for the NIF.

The proposed technique for NIF is that of smoothing by spectral dispersion (SSD). The general concept of SSD is to spectrally disperse broad-bandwidth light onto a phase plate so that each element of the RPP is irradiated by a different frequency. The relative phase between beamlets from different phase-plate elements will then vary in time according to their frequency differences. The larger the bandwidth, the more rapidly the structure will change and the more rapidly the smoothing will take place.

There are two variations of the SSD experimental setup. In the first one, referred to as *one-dimensional* (1D) SSD [44] the laser light is spectrally broadened by phase modulation using an electro-optic crystal. A pair of diffraction gratings are used to angularly disperse the frequencies across the beam, without distorting the temporal pulse shape. The beam is split into beamlets with RPP, such that the beamlet diffraction-limited focal spot is the size of the target. Because of the frequency differences this results in shifted patterns that average out in the focal plane. In the two-dimensional (2D) scheme [46] two modulators of different frequencies are used together with two diffraction gratings perpendicular to each other.

Recently, SSD has been used in combination with another technique, called *polarization smoothing* (PS) [13, 33]. The polarization smoothing [47, 48] divides

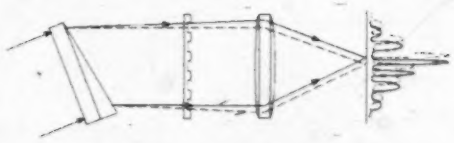

Figure 1.6: Schematic diagram of a polarization smoothing using a wedge of birefringent material. The laser beam is split equally into two beamlets with orthogonal polarizations, which are deflected by the wedge at slightly different angles resulting in two shifted patterns at the focal plane.

the light power into two beams with crossed polarization and slightly shifted focal speckle patterns.

In many experiments, combinations of different smoothing techniques are explored. Examples include SSD + PS [46, 1], RPP+PS [18, 13] and SSD+KPP [20, 33]. In all of them RPP is an integral part of the laser chain.

Although initial studies of the effects of spatial and temporal incoherence were concentrated on hydrodynamic instabilities such as RT, it became clear that the incoherence also contributes to suppression of parametric instabilities such as Raman [41, 17, 16], Brillouin [31, 13, 15, 16] and filamentation [22, 33].

The emission and absorption of light are strongly affected by scattering processes. In the absence of plasma effects, a wave may be scattered by Thomson or Compton scattering, in which the wave field causes the particle to oscillate and as a result there is an emission of dipole radiation. If we use the language of quantum physics, the elementary scattering process can be illustrated as in Fig.(1.7)(a). Here, a photon, represented by the dashed line, is absorbed by a particle, the solid line, and another photon is emitted. According to the law of energy conservation, the particle energy loss is transformed to a change of wave frequency. In plasma, the wave changes the properties of the medium, leading to more complicated nonlinear scattering, Fig.(1.7)(b). In this case we observe a three-wave process, reviewed below.

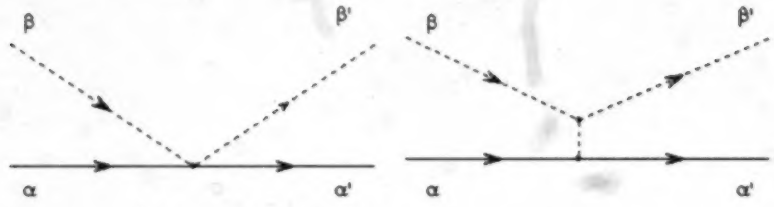

Figure 1.7: Scattering processes: (a) scattering of wave by particle, (b) scattering with emission of an intermediate wave.

A plasma is an inherently nonlinear medium capable of sustaining a wide variety of waves and instabilities. Figure (1.8) shows the operation regions for different parametric instabilities for an electromagnetic wave incident on a plasma with a linear density gradient.

SRS is the process in which the incident wave decays into another electromagnetic wave and electron plasma wave. For a linear density profile, Raman backscattering is a convective instability except in the vicinity of N/4, where it merges with two-plasmon decay (TPD) instability to form an absolute instability. The threshold for convective backscattering SRS is given by:

$$I_{SRS} \geq \frac{40}{L_N \lambda_0},$$

where I is in units of $10^{14} W/cm^2$, L_N is the density scale in units of $100\mu m$ and the wavelength λ_0 is measured in μm.

SBS is the process where the incident wave decays into another electromagnetic wave and an ion-acoustic wave, with threshold

$$I_{SBS} \geq 1.7 \frac{T_e}{(n/n_c) L_u \lambda_0},$$

where the velocity scale length is in units of $100\mu m$ and the electron temperature, T_e, is measured in keV.

Filamentation instability is a four-wave interaction. The traveling wave, $(\omega_0, \mathbf{k}_0)$, emits ion acoustic waves in opposite directions coupling two reflected

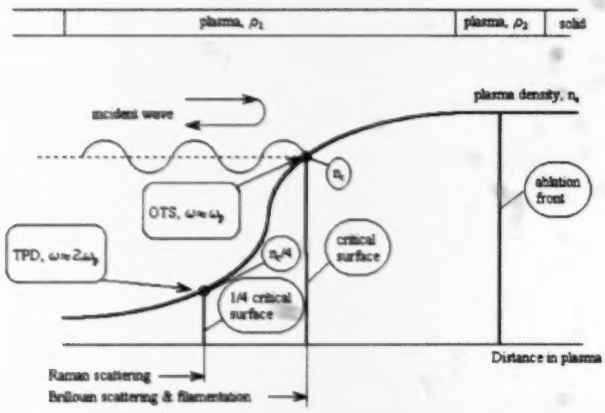

Figure 1.8: Diagram of the operation regions for different parametric instabilities. Shown as points are the TPD and the oscillating two-stream instability (OTS).

electromagnetic waves. The waves with up-shifted and down-shifted k-components are called Stokes and anti-Stokes waves respectively. A purely growing instability occurs that deflects the wave energy into the transverse direction, which leads to the formation of long filaments.

The TPD process is one in which the incident wave decays into two Langmuir waves. Its threshold condition is

$$I_{TPD} \geq 0.54 \frac{T_e}{L_N \lambda_0}.$$

When laser light propagates through a two-species plasma composed of electrons and ions, a variety of physical processes takes place. They can be cast into two groups, low and high frequency respectively, depending on which species, ion or electron, play the the primary role in these processes.

This study addresses the low frequency ion response on propagation of long (hundreds of picoseconds) and intense laser pulses through underdense plasma. It examines in particular the effect of plasma induced smoothing and its effect on parametric instabilities such as stimulated Brillouin scattering, filamentation instability, and the self-focusing instability (SFI).

Several experiments have shown that a laser beam propagating in an underdense plasma develops angular spreading and spectral broadening with a shift toward longer wavelengths [57, 56, 65]. Similar plasma induced angular spreading and red shift have been observed in simulations [64, 54] describing the interaction of a coherent beam with a plasma. These results were explained in terms of forward SBS and filamentation instabilities. On the other hand, numerical studies [63] with RPP laser beams have shown that both the angular divergence and temporal bandwidth of the transmitted light are larger than those of the incident light in regimes where filamentation does not reach a steady state. This ability of an underdense plasma to induce temporal incoherence together with an additional spatial incoherence to a propagating laser beam is called *plasma induced smoothing.*

The angular and spectral broadening of the laser beam can be related to spatial and temporal statistical characteristics of the laser field. We give the following interpretation of its origin in the regime where the average power in a speckle approaches the self-focusing threshold for laser filaments to form in the front part of the plasma. The high-intensity filaments are unstable [62, 61, 55, 60] and the instability corresponds to forward SBS growing inside the cavity formed by the density depletion associated with the filament. The temporal growth rate is characteristic of the so-called strong coupling regime [55, 60]. This instability gives rise, in the front part of the plasma, to scattered waves, which are temporally incoherent and characterized by a large spectral red shift and a broad angular distribution. This waves can then be spatially amplified during their propagation through the plasma by the forward SBS instability in the so-called *incoherent* regime of three-wave coupling. This incoherent spatial amplification corresponds to a collective process in the sense that it involves a spatial domain larger than the size of a single hot spot. In Fourier space, it gives

rise to an increase of the angular width and of the spectral broadening while propagating further inside the plasma. In real space, it results in speckle size and correlation time both decreasing with the longitudinal coordinate. In the low intensity regime these effects result from a single scattering process only. In the case of higher laser beam intensities, the scattered waves can themselves be unstable with regard to forward SBS, leading to a multiple forward SBS process. This leads to further angular and spectral broadening of the transmitted light.

The ability of the plasma to introduce additional incoherence to a propagating laser beam has important implications concerning the growth of backscattering instabilities. We show that additional spatial incoherence by itself is able to reduce backward instabilities, because the gain factor is smaller in the shorter speckles. In addition, it has recently been shown [53] that even a small level of temporal incoherence is able to dramatically reduce backscatter instabilities. Namely, in contradiction with usual estimates [58, 59], it is found that a correlation time as long as a few growth times can reduce the reflectivity by several orders of magnitude.

To summarize, in the case of single beam interactions, plasma self-induced smoothing gives rise to angular broadening, spectral broadening and red shift of the transmitted light. It involves the self-focusing instability of speckles containing more power than the critical power for self-focusing, and the subsequent dynamical evolution of laser filaments, coupled to forward SBS. In the case of crossed beam illumination, we have found that plasma self-induced smoothing in addition to these single beam effects dramatically enhances large angle forward SBS by which the energy of one beam can be transferred to the other. It is a very important feature because the energy transfer between crossed-beams can destroy the carefully designed energy balance between the multiple laser beams in the inertial confinement fusion experiments, thus affecting the symmetry of a

pellet illumination.

The content of the thesis is organized as follows. In Chapter 2 we specify the theoretical model used in our simulations. The mathematical formalism based on the hydrodynamic approach is used to derive the electromagnetic and ion-acoustic wave equations. We employ these equations in two ways. Firstly, after a concise discussion of physical mechanisms and the characteristics of SBS and ponderomotive self-focusing in the framework of the parametric processes, we derive the dispersion relation for those two instabilities and extract some simple linear characteristics that are used to identify the parametric processes in the following chapters. Secondly, we describe the model equations used in the numerical simulations and their discretization and parallelization.

In Chapter 3 we explore the early-time evolution of a single hot spot laser beam. We derive the basic equations for the single speckle resonant instability. Theoretical analysis and numerical simulations of the filament instability are presented.

In Chapter 4 we construct a theoretical model of a realistic single hot spot laser beam using a combination of two Gaussian distributions fitted to the experimental data for for beam profile and use it in a series of numerical simulations. Some of the presented results include the FI of a wide laser beam, the beam evolution in time, and the reflected and transmitted light as a function of plasma density. Special attention is given to the spatial-temporal evolution of near-forward SBS and FI and their mutual interplay.

In Chapter 5 we consider a single spatially incoherent laser beam. After an overview of the different optical smoothing techniques, we derive the model of our laser beam on the basis of random phase plate. Next, we analyze the spatial and temporal incoherence of the propagating beam with the help of suitably defined correlation functions. We characterize quantitatively the ability of an

underdense plasma to induce temporal incoherence together with an additional spatial incoherence to a propagating laser beam and quantitatively characterize the plasma induced smoothing by introducing a local (in space and time) f-number of the laser beam. We explore the development of plasma induced angular spreading and spectral broadening with a shift toward longer wavelengths. We derive a theoretical model for single forward Brillouin scattering from a spatially incoherent beam, present simulation results for the spectral shift of the transmitted light, and explain the reduction of backward SBS

In Chapter 6 we present a model for two crossed spatially incoherent laser beams. We describe the set of experiments that formed the basis for our numerical simulations and the typical parameter sets of the computational runs. We show the results from the numerical simulations for the time evolution of the system characteristics such as beam power and angle between beams for crossed beams with equal intensities. We discuss the frequency spectra of the transmitted light in detail and perform a close comparison between experiment and simulation. We also discuss the density fluctuation spectra for the same case. Lastly, we consider the energy transfer between crossed beams with colors in the case of beams with equal intensities and beams with different intensities.

Bibliography

[1] R. L. Berger, E. Lefebvre, A. B. Langdon, J. E. Rothenberg, C. H. Still, and E. A. Williams, Phys. Plasmas **6**, 1043 (1999).

[2] T. R. Boehly, D. L. Brown, R. S. Craxton, R. L. Keck, J. P. Knauer, J. H. Kelly, T. J. Kessler, S. A. Kumpan, S. J. Loucks, S. A. Letzring, F. J. Marxhall, R. L. McCrory, S. F. B. Morse, W. Seka, J. M. Soures, and C. P. Verdon, Opt. Commun. **133**, 495 (1997).

[3] T. R. Boehly, V. A. Smalyuk, D. D. Meyerhofer, J. P. Knauer, D. K. Bradley, R. S. Craxton, M. J. Guardalben, S. Skupsky, and T. J. Kessler, J. Appl. Phys. **85**, 3444 (1999).

[4] S. E. Bodner, D. G. Golmbant, J. H. Gardner, R. H. Lehmberg, S. P. Obenschain, L. Phillips, A. J. Schmitt, J. D. Sethian, R. L. McCrory, W. Seka, C. P. Verdon, J. P. Knauer, B. B. Afeyan, and H. T. Powell, Phys. of Plasmas **5**, 1901 (1998).

[5] A. V. Chirokikh, R. S. Craxton, W. Seka, A. Simon, and V. T. Tikhonchuk, Phys. Plasmas **5**, 1104 (1998).

[6] A.V. Deniz, T. Lehecka, R.H. Lehmberg and S.P. Obenschain, Opt. Commun. **147**, 402 (2000).

[7] T. R. Dittrich, S. W. Haan, M. M. Marinak, S. M. Pollaine, D. E. Hinkel, D. H. Munro, C. P. Verdon, G. L. Strobel, R. McEachern, R. C. Cook, and C. C. Roberts, Phys. Plasmas **6**, 2164 (1999).

[8] S. N. Dixit, J. K. Lawson, K. R. Manes, H. T. Powell, and K. A. Nugent, Optics Lett. **19**, 417 (1994).

[9] S. N. Dixit, M. D. Feit, M. D. Perry, and H. T. Powell, Optics Lett. **21**, 1715 (1996).

[10] M. Dunne, M. Borghesi, A. Iwase, M. W. Jones, R. Taylor, and O. Willi, Phys. Rev. Lett. **75**, 3858 (1995).

[11] M. H. Emery, J. H. Gardner, R. H. Lehmberg, and S. P. Obenschain, Phys. Fluids B **3**, 2640 (1991).

[12] R. Epstein, J. Appl. Phys. **82**, 2123 (1997).

[13] J. Fuchs, C. Labaune, S. Depierreux, H. A. Baldis, and A. Michard, Phys. Rev. Lett. **84**, 3089 (2000).

[14] J. Fuchs, C. Labaune, S. Depierreux, H. A. Baldis, A. Michard, and G. James, Phys. Rev. Lett. **86**, 432 (2001).

[15] S. H. Glenzer, L. J. Suter, R. E. Turner, B. J. MacGowan, K. G. Estabrook, M. A. Blain, S. N. Dixit, B. A. Hammel, R. L. Kauffman, R. K. Kirkwood, O. L. Landen, M.-C. Monteil, J. D. Moody, T. J. Orzechovski, D. M. Pennington. G. F. Stone, and T. L. Weiland, Phys. Rev. Lett. **80**, 2845 (1998).

[16] S. H. Glenzer, L. J. Suter, R. L. Berger, K. G. Estabrook, B. A. Hammel, R. L. Kauffman, R. K. Kirkwood, B. J. MacGowan, J. D. Moody, J. E. Rothenberg, and R. E. Turner, Phys. Plasmas **7**, 2585 (2000).

[17] P. N. Guzdar, C. S. Liu, and R. H. Lehmberg, Phys. Fluids B **5**, 910 (1993).

[18] S. Hüller, Ph. Mounaix, and V. T. Tikhonchuk, Phys. Plasmas **5**, 2706 (1998).

[19] Y. Kato, K. Mima, N. Miyanaga, S. Arinaga, Y. Kitagava, M. Nakatsuka, and C. Yamanaka, Phys. Rev. Lett. **53**, 1057 (1984).

[20] R. L. Kauffman, L. V. Powers, S. N. Dixit, S. G. Glendinning, S. H. Glenzer, R. K. Kirkwood, O. L. Landen, B. J. MacGowan, J. D. Moody, T. J. Orzechowski, D. M. Pennington, G. F. Stone, L. J. Suter, R. E. Turner, T. L. Weiland, A. L. Richard and M. A. Blain, Phys. Plasmas **5**, 1927 (1998).

[21] J. D. Kilkenny, S. G. Glendinning, S. W. Haan, B. A. Hammel, J. D. Lindl, D. Munro, B. A. Remington, S. V. Weber, J. P. Knauer, and C. P. Verdon, Phys. Plasmas **1**, 1379 (1994).

[22] C. Labaune, S. Baton, T. Jalinaud, H. A. Baldis, and D. Pesme, Phys. Fluids B **4**, 2224 (1992).

[23] E. Lefebvre, R. L. Berger, A. B. Langdon, B. J. MacGowan, J. E. Rothenberg, and E. A. Williams, Phys. Plasmas **5**, 2701 (1998).

[24] T. Lehecka, R. H. Lehmberg, A. V. Deniz, K. A. Gerber, S.P. Obenschain, C. J. Pawley, M. S. Pronko and C. A. Sullivan, Opt. Commun. **117**, 485 (1995).

[25] R. H. Lehmberg, and S. P. Obenschain, Opt. Commun. **46**, 27 (1983).

[26] R. H. Lehmberg, A. J. Schmitt, and S. E. Bodner, J. Appl. Phys. **62**, 2680 (1987).

[27] R. H. Lehmberg, and J. Goldhar, Fusion Tech. **11**, 532 (1987).

[28] R. H. Lehmberg, Opt. Commun. **130**, 51 (1996).

[29] R. H. Lehmberg, and J. E. Rothenberg, J. Appl. Phys. **87**, 1012 (2000).

[30] J. Lindl, Phys. Plasmas **2**, 3933 (1995).

[31] J. D. Moody, H. A. Baldis, D. S. Montgomery, R. L. Berger, K. Estabrook, W. L. Kruer, B. F. Lasinski, E. A. Williams, S. Dixit, and C. Labaune, Phys. Plasmas **2**, 4285 (1995).

[32] J. D. Moody, B. J. MacGowan, S. H. Glenzer, R. K. Kirkwood, W. L. Kruer, D. S. Montgomery, A. J. Schmitt, E. A. Williams, and G. F. Stone, Phys. Plasmas **7**, 2114 (2000).

[33] J. D. Moody, B. J. MacGowan, J. E. Rothenberg, R. L. Berger, L. Divol, S. H. Glenzer, R. K. Kirkwood, E. A. Williams, and P. E. Young, Phys. Rev. Lett. **86**, 2810 (2001).

[34] M. Murakami, K. Nishihara, and H. Azechi, J. Appl. Phys. **74**, 802 (1993).

[35] H. Nakano, K. Tsubakimoto, N. Miyanaga, M. Nakatsuka, T. Kanabe, H. Azechi, T. Jitsuno, and S. Nakai, J. Appl. Phys. **73**, 2122 (1993).

[36] K. Nishihara, M. Murakami, H. Azechi, T. Jitsuno, T. Kanabe, M. Katayama, N. Miyanaga, M. Nakai, M. Nakatsuka, K. Tsubakimoto, and S. Nakai, Phys. Plasmas **1**, 1653 (1994).

[37] Qiaofeng Tan, Yingbai Yan, Guofan Jin, and Minxian Wu, Opt. Commun. **175**, 13 (2000).

[38] S. P. Regan, D. K. Bradley, A. V. Chirokikh, R. S. Craxton, D. D. Meyerhofer, W. Seka, R. W. Short, A. Simon, R. P. J. Town, B. Yaakobi, J. J. Caroll, and R. P. Drake, Phys. Plasmas **6**, 2072 (1999).

[39] J. E. Rothenberg, J. Opt. Soc. Am. B, **14**, 1664 (1997).

[40] M. D. Rosen, Phys. Plasmas **6**, 1690 (1990).

[41] W. Seka, R. E. Bahr, R. W. Short, A. Simon, R. S. Craxton, D. S. Montgomery, and A. E. Rubenchik, Phys. Fluids B **4**, 2232 (1992).

[42] J. D. Schnittman, and R. S. Craxton, Phys. Plasmas **3**, 3786 (1996).

[43] S. Skupsky, and K. Lee, J. Appl. Phys. **54**, 3662 (1983).

[44] S. Skupsky, R. W. Short, T. Kessler, R. S. Craxton, S. Letzring, and J. M. Soures, J. Appl. Phys. **66**, 3456 (1989).

[45] S. Skupsky, and T. Kessler, J. Appl. Phys. **74**, 802 (1993).

[46] S. Skupsky, and R. S. Craxton, Phys. Plasmas **6**, 2157 (1999).

[47] K. Tsubakimoto, M. Nakatsuka, H. Nakano, T. Kanabe, T. Jitsuno, and S. Nakai, Opt. Commun. **91**, 9 (1992).

[48] K. Tsubakimoto, T. Jitsuno, N. Miyanaga, M. Nakatsuka, T. Kanabe, and S. Nakai, Opt. Commun. **103**, 185 (1993).

[49] D. Veron, H. Ayral, C. Gouedard, D. Husson, J. Lauriou, O. Martin, B. Meyer, M.Rostaing, and C. Sauteret, Opt. Commun. **65**, 42 (1988).

[50] D. Veron, G. Thiell, and C. Gouedard, Opt. Commun. **97**, 259 (1993).

[51] R. G. Watt, D. C. Wilson, R. E. Chrien, R. V. Hollis, P. L. Gobby, R. J. Mason, R. A. Kopp, R. A. Lerche, D. H. Kalantar, B. MacGowan, M. B. Nelson, T. Phillips, P. W. McKenty, and O. Willi, Phys. Plasmas **4**, 1379 (1997).

[52] R. G. Watt, J. Duke, C. J. Fontes, P. L. Gobby, R. V. Hollis, R. A. Kopp, R. J. Mason, D. C. Wilson, C. P. Verdon, T. R. Boehly, J. P. Knauer, D. D. Meyehofer, V. Smalyuk, R. P. J. Town, A. Iwase, and O. Willi, Phys. Rev. Lett. **81**, 4644 (1998).

[53] L. Divol and Ph. Mounaix, Phys. Plasmas **6**, 4037 (1999).

[54] V. V. Eliseev, I. Ourdev, W. Rozmus, V. T. Tikhonchuk, C. E. Capjack, and P. E. Young, Phys. Plasmas **4**, 4333 (1997).

[55] V. Eliseev, D. Pesme, W. Rozmus, V. T. Tikhonchuk, and C. E. Capjack, Phys. Scripta **T75**, 112 (1998).

[56] C. Labaune, H. A. Baldis, B. Cohen, W. Rozmus, S. Depierreux, E. Schifano, B. S. Bauer, and A. Michard, Phys. Plasmas **5**, 2048 (1999).

[57] J. D. Moody, B. J. MacGowan, S. H. Glenzer, R. K. Kirkwood, W. L. Kruer, A. J. Schmitt, E. A. Williams, and G. F. Stone, Phys. Rev. Lett. **83**, 1783 (1999).

[58] D. Pesme, Annual Report CNRS: Interaction Laser Matiere – LULI **29**, 1 (1987),

[59] D. Pesme, in *La Fusion Thermonucleaire Inertielle par Laser*, edited by R. Dautray and J.-P. Watteau (Eyrolles, Paris, 1993), Vol. 1.

[60] D. Pesme, W. Rozmus, V. T. Tikhonchuk, A. V. Maximov, I. Ourdev, and C. H. Still, Phys. Rev. Lett. **84**, 278 (2000).

[61] E. Valeo, Phys. Fluids **17**, 1391 (1974).

[62] V. E. Zakharov and A. M. Rubenchik, Sov. Phys. JETP **38**, 494 (1974).

[63] A. J. Schmitt and B. B. Afeyan, Phys. Plasmas **5**, 503 (1998).

[64] S. C. Wilks, P. E. Young, J. Hammer, M. Tabak, and W. L. Kruer, Phys. Rev. Lett. **73**, 2994 (1994).

[65] P. E. Young, J. H. Hammer, S. C. Wilks, and W. L. Kruer, Phys. Plasmas **2**, 2825 (1995).

Chapter 2

Basic concepts

A plasma is a many-particle system and it is natural to use methods of Statistical Physics to describe it[7, 13, 26]. Although such an approach allows consideration of kinetic effects like Landau damping, it requires the use of complicated mathematical apparatus and so is difficult for numerical implementation.

An alternative approach, adopted in this study, is the method of multi-component hydrodynamics, see as ex.[14, 38]. For a two-component plasma, consisting of electrons and a single species of (positively charged) ions, the large difference in the masses of the two components does not allow for fast energy exchange between the electrons and the ions. This makes it possible to consider the plasma as a collection of "fluids" – as many as there are plasma components.

The connection between the two approaches is well known [4, 38]. Using the kinetic theory formalism and taking the first two moments of Boltzmann's equation for the distribution functions $f_\alpha(\mathbf{v}_\alpha, \mathbf{r}_\alpha, t)$ for each of the components, α, one can obtain the continuity and fluid force equations, which are the basis of the hydrodynamical approach.

In the following Section, 2.1, we lay out the theoretical foundation of the hydrodynamic approach. The mathematical formalism specified there is then used to derive the electromagnetic and ion-acoustic wave equations in Sections 2.2 and 2.3 respectively. In Section 2.4 we discuss the physical mechanisms and

the characteristics of SBS and ponderomotive self-focusing in the framework of the parametric processes. In Section 2.5 we present a detailed derivation of the dispersion relation for those two instabilities and derive some simple linear characteristics that are used to identify the parametric processes in the following chapters. Section 2.6 contains a description of the model equations used in the numerical simulations and their discretization and parallelization. The last Section of this chapter, 2.7, presents the Gaussian laser beam model that is used extensively in the numerical calculations.

2.1 Theoretical foundations

The propagation of light is described by Maxwell's equations:

$$\nabla \times \mathbf{E} = -\frac{1}{c}\frac{\partial \mathbf{B}}{\partial t}, \tag{2.1}$$

$$\nabla \times \mathbf{B} = \frac{1}{c}\frac{\partial E}{\partial t} + \frac{4\pi}{c}\mathbf{J}, \tag{2.2}$$

$$\nabla \cdot \mathbf{E} = 4\pi\rho, \tag{2.3}$$

$$\nabla \cdot \mathbf{B} = 0, \tag{2.4}$$

where c is the speed of light. The *total charge density* ρ

$$\rho = \sum_{\alpha} n_\alpha q_\alpha, \tag{2.5}$$

and the *total current density* $\mathbf{J}$

$$\mathbf{J} = \sum_{\alpha} n_\alpha q_\alpha \mathbf{u}_\alpha, \tag{2.6}$$

are related by the *charge conservation equation*

$$\frac{\partial \rho}{\partial t} + \nabla \cdot \mathbf{J} = 0. \tag{2.7}$$

Here n_α is the density of α-type particles, $\mathbf{u}_\alpha$ is the ensemble-averaged flow velocity and the subscript $\alpha = e, i$ denotes the electron and ion species respectively.

All considerations of this study are based on the general model of an ion wave response to the ponderomotive force of an electromagnetic wave in a two-dimensional Cartesian geometry. The model is inferred from the two-fluid model, which treats electrons and ions as conducting fluids coupled through collisions and Maxwell's equations. In this approach, plasma is described by the *continuity equation*

$$\frac{\partial n_\alpha}{\partial t} + \nabla \cdot (n_\alpha \mathbf{u}) = 0, \tag{2.8}$$

and an *equation of motion*

$$n_\alpha m_\alpha \left(\frac{\partial}{\partial t} + \mathbf{u}_\alpha \cdot \nabla \right) \mathbf{u}_\alpha = n_\alpha q_\alpha \left(\mathbf{E} + \frac{1}{c} \mathbf{u}_\alpha \times \mathbf{B} \right) - \nabla p_\alpha, \tag{2.9}$$

where m_α is the mass of α-type particles *. The last equation is often called the *momentum transfer equation* [33]. Its left hand side is the full time derivative of the velocity $\mathbf{u}_\alpha$ and represents the change of momentum (per unit volume per unit time) in a plasma element moving with velocity $\mathbf{u}_\alpha$. The next term is the change of momentum due to the force of the average fields. The last term represents the force related to the scalar pressure p_α due to spatial inhomogeneity.

The above set of moment equations is not closed, because each equation includes higher velocity moments. In order to close the system of hydrodynamic equations we use the thermodynamic *equation of state*, which connects the dynamic change of pressure p with the change of particle density ρ †.

There are two different cases with respect to the description of the pressure term, ∇p_α, which are of interest for us. In the first, *isothermal* case, when the temperature of species α is varying slowly compared to the wave period, one

*The r.h.s. of the equation of motion, Eq. (2.9), can be easily adapted to account for the presence of a magnetic field (via the term $\nabla \cdot \mathbf{P}$ for the stress-tensor $\mathbf{P}$) or collisions (via the term $m_\alpha n_\alpha (\mathbf{u}_\alpha - \mathbf{u}_0)/\tau_\alpha$, where $\mathbf{u}_0$ is the velocity of the neutral plasma component and τ_α is the mean collision time for type α species.

†This is similar to the reduction of the BBKGY hierarchy chain of N-particle distribution functions to a one-particles distribution function of Vlasov's equation by neglecting the higher order correlations [36].

obtains

$$\nabla p_\alpha = \nabla(n_\alpha T_\alpha) = T_\alpha \nabla n_\alpha. \tag{2.10}$$

On the other hand, for rapidly varying compression, i.e. *adiabatic*

$$\nabla p_\alpha = \nabla(n_\alpha T_\alpha) = T_\alpha \nabla n_\alpha + n_\alpha \nabla T_\alpha = \gamma_\alpha T_\alpha \nabla n_\alpha, \tag{2.11}$$

where $\gamma_\alpha = (2 + N)/N$ is the ratio of specific heats and N is the number of degrees of freedom.

This lays out the basic groundwork for the derivation of electromagnetic and ion-acoustic wave equations in the next two subsections.

2.2 Electromagnetic wave equation

Choosing to work in terms of a *vector potential*, $\mathbf{A}$, and an electrostatic potential, ϕ, the electric nd magnetic fields can be written as:

$$\mathbf{E} = -\frac{1}{c}\frac{\partial \mathbf{A}}{\partial t} - \nabla\phi, \tag{2.12}$$

$$\mathbf{B} = \nabla \times \mathbf{A}. \tag{2.13}$$

Eq. (2.2) takes the form

$$\nabla \times \nabla \times \mathbf{A} = \frac{4\pi}{c}\mathbf{J} - \frac{1}{c^2}\frac{\partial^2 \mathbf{A}}{\partial t^2} - \frac{1}{c}\frac{\partial}{\partial t}\nabla\phi. \tag{2.14}$$

For the l.h.s. we can use the vector identity

$$\nabla \times \nabla \times \mathbf{A} = \nabla(\nabla \cdot \mathbf{A}) - \nabla^2 \mathbf{A}, \tag{2.15}$$

which can be simplified using the Coulomb gauge $\nabla \cdot \mathbf{A} = 0$, so Eq. (2.14) becomes

$$\left(\frac{1}{c^2}\frac{\partial^2}{\partial t^2} - \nabla^2\right)\mathbf{A} = \frac{4\pi}{c}\mathbf{J} - \frac{1}{c}\frac{\partial}{\partial t}\nabla\phi. \tag{2.16}$$

To simplify the r.h.s. we derive the Poisson equation by substituting for the electric field in Eq. (2.3) and obtain

$$\nabla^2\phi = -4\pi\rho. \tag{2.17}$$

Using Eq. (2.17) and Eq. (2.7) gives

$$\nabla \cdot \left(\frac{\partial}{\partial t} \nabla \phi - 4\pi \mathbf{J} \right) = 0. \tag{2.18}$$

Separating the current density $\mathbf{J}$ into transverse $\mathbf{J}_\perp$ and longitudinal $\mathbf{J}_\parallel$ parts

$$\mathbf{J} = \mathbf{J}_\perp + \mathbf{J}_\parallel, \tag{2.19}$$

and taking into account that $\nabla \cdot \mathbf{J}_\perp = 0$, Eq. (2.18) gives

$$\frac{\partial}{\partial t} \nabla \phi = 4\pi \mathbf{J}_\parallel \tag{2.20}$$

so the RHS of Eq. (2.16) reduces to $4\pi \mathbf{J}_\perp / c$. To substitute for $\mathbf{J}_\perp$ in this expression we neglect the ion contribution in the current density, Eq. (2.6), and linearize the equation of motion, Eq. (2.9), for the electrons, using plasma homogeneity (i.e. $n_e(x) = n_{e0}$) to set $\nabla p = 0$. The result is

$$\frac{\partial \mathbf{u}_e}{\partial t} = -\frac{e}{m} \mathbf{E}. \tag{2.21}$$

Hence

$$\mathbf{u}_\perp = \frac{e}{mc} \mathbf{A}, \tag{2.22}$$

and we obtain the following equation for the vector potential $\mathbf{A}$ of the light wave

$$\left(\frac{\partial^2}{\partial t^2} - c^2 \nabla^2 \right) \mathbf{A} = -\frac{4\pi e^2}{m} n_e \mathbf{A}. \tag{2.23}$$

The next step of the derivation is based on the fact that the problem has two different time scales due to the large mass difference between electrons and ions forming the plasma. In order to separate the two scales, we represent the quantities of interest as a linear combination of terms having fast and slow time dependence and perform *averaging over the fast time scale.* Taking into account that $\omega_0 \gg \omega_{pe}$ we choose the laser frequency ω_0 to establish the fast scale. We use the observation that the slow time-scale variables are practically constant

over the short time interval $2\pi/\omega_0$ to integrate the corresponding equation from any time t to $t + 2\pi/\omega_0$. For this purpose we substitute into Eq. (2.23) for

$$\mathbf{A} = \mathbf{A}_h \tag{2.24}$$

$$n_e = n_{e0} + \delta n_{el} + \delta n_{eh} \tag{2.25}$$

where the electron density n_e contains both high $\delta n_{eh} \sim \delta n_h(\tau)e^{-i\omega_0 t}$ and low $\delta n_{el} \sim \delta n_e(\tau)$ density fluctuations around the uniform background density n_{e0}. The vector potential, $\mathbf{A}$, has only a high frequency component for the processes under consideration in this work. The averaging over the fast time scale is defined as

$$< g >= \frac{\omega_0}{2\pi}\int_t^{t+2\pi/\omega_0}[\, g\,]dt.$$

It gives for example $< \delta n_{el} >= \delta n_e$ and $< \delta n_{eh} >= 0$. So to retain only the slowly varying terms we first multiply Eq. (2.23) by the factor $\exp(i\omega_0 t)$. The result after averaging is

$$\left(\frac{\partial^2}{\partial t^2} - c^2\nabla^2 + \omega_{pe}^2\right)\mathbf{A}_h = -\omega_{pe}^2\frac{\delta n_e}{n_{e0}}\mathbf{A}_h, \tag{2.26}$$

which describes the scattering of a large amplitude high frequency light wave $\mathbf{A}_h$ by a small amplitude low frequency density fluctuation δn_e.

2.3 Ion-acoustic wave equation

To derive an equation for the plasma density fluctuations we begin with the equation of motion, Eq. (2.9), for the electrons and use the vector identity

$$(\mathbf{u}\cdot\nabla)\mathbf{u} = \frac{1}{2}\nabla(\mathbf{u}^2) - \mathbf{u}\times(\nabla\times\mathbf{u}), \tag{2.27}$$

to obtain

$$\frac{\partial \mathbf{u}_e}{\partial t} = \mathbf{u}_e\times\left(\nabla\times\mathbf{u}_e - \frac{e}{mc}\mathbf{B}\right) - \frac{1}{2}\nabla(\mathbf{u}_e^2) - \frac{e}{m}\mathbf{E} - \frac{\nabla \mathbf{p}_e}{n_e m}. \tag{2.28}$$

The first term in the r.h.s. vanishes because the expression in brackets is a constant vector. To show this we take a derivative and substitute from Eq. (2.21) and Ampère's law Eq. (2.1).

$$\nabla \times \frac{\partial \mathbf{u}_e}{\partial t} - \frac{e}{m}\frac{1}{c}\frac{\partial \mathbf{B}}{\partial t} = -\frac{e}{m}\nabla \times \mathbf{E} + \frac{e}{m}\nabla \times \mathbf{E} = 0. \tag{2.29}$$

Hence the equation of motion, Eq. (2.28), simplifies to

$$\frac{\partial \mathbf{u}_e}{\partial t} = -\frac{1}{2}\nabla(\mathbf{u}_e^2) - \frac{e}{m}\mathbf{E} - \frac{\nabla \mathbf{p}_e}{n_e m}. \tag{2.30}$$

Separating the velocity $\mathbf{u}_e$ into longitudinal $\mathbf{u}_{\|}$ and transverse components

$$\mathbf{u}_e = \mathbf{u}_{\|} + \frac{e\mathbf{A}}{mc}, \tag{2.31}$$

and substituting for the electric field from Eq. (2.13) we obtain:

$$\frac{\partial \mathbf{u}_{\|}}{\partial t} = -\frac{e}{m}\nabla\phi - \frac{1}{2}\nabla\left(\mathbf{u}_{\|} + \frac{e\mathbf{A}}{mc}\right)^2 - \frac{\nabla \mathbf{p}_e}{n_e m}. \tag{2.32}$$

Since we are considering low frequency fluctuations, we neglect the electron inertia ($\partial u_{\|}/\partial t \to 0$) and use the isothermal equation of state Eq. (2.10)

$$\frac{e}{m}\nabla\phi = -\frac{1}{2}\nabla\left(\mathbf{u}_{\|} + \frac{e\mathbf{A}}{mc}\right)^2 - v_{Te}^2\frac{\nabla n_e}{n_e}, \tag{2.33}$$

where

$$v_{Te} = \sqrt{T_e/m}, \tag{2.34}$$

is the electron thermal velocity. Separating the fast and slow time scales as in the previous Section 2.2, using Eq. (2.25) and letting $\phi = \delta\phi_l$, averaging over the fast time scale gives

$$\frac{e}{m}\nabla\delta\phi_l = \frac{e^2}{m^2c^2}\nabla\left\langle \mathbf{A}_h^2 \right\rangle + \frac{v_{Te}^2}{n_{e0}}\nabla\delta n_e. \tag{2.35}$$

To account for the ion response we linearize the continuity equation, Eq. (2.8), and the equation of motion for the ions, Eq. (2.9), by letting

$$n_i = n_{i0} + \delta n_{il}, \tag{2.36}$$

$$\mathbf{u}_i = \delta \mathbf{u}_{il}, \tag{2.37}$$

end neglecting the ion pressure

$$\frac{\partial \delta n_{il}}{\partial t} + n_{i0} \nabla \cdot \delta \mathbf{u}_{il} = 0, \tag{2.38}$$

$$\frac{\partial \delta \mathbf{u}_{il}}{\partial t} + \frac{Ze}{M} \nabla \delta \phi_l = 0. \tag{2.39}$$

Combining the time derivative of Eq. (2.38) with the divergence of Eq. (2.39) we obtain

$$\frac{\partial^2 \delta n_{il}}{\partial t^2} - \frac{n_{i0} Ze}{M} \nabla^2 \delta \phi_l = 0. \tag{2.40}$$

For the final step in the derivation we take the divergence of Eq. (2.35) and substitute for $\nabla^2 \delta \phi_l$ in Eq. (2.40) and use the electro-neutrality conditions

$$Z n_{i0} = n_{e0}, \tag{2.41}$$

$$Z \delta n_{il} = \delta n_e. \tag{2.42}$$

Denoting the ion-acoustic velocity as

$$c_s = \sqrt{ZT_e/M}, \tag{2.43}$$

we obtain the following equation for the low frequency density fluctuations

$$\left(\frac{\partial^2}{\partial t^2} - c_s^2 \nabla^2 \right) \delta n_e = \frac{Z n_{e0} e^2}{mMc^2} \nabla^2 \left\langle \mathbf{A}_h^2 \right\rangle, \tag{2.44}$$

Before extracting some important quantitative information from the electromagnetic and ion-acoustic equations, in the following section we present the physical picture of the processes.

2.4 Parametric processes

The plasma response to an externally applied force is realized through its natural (normal, principal) modes. The excitation and amplification of these plasma modes by an electromagnetic pump wave can be described in terms of *parametric processes*. The pump wave modifies the plasma parameters that enter the

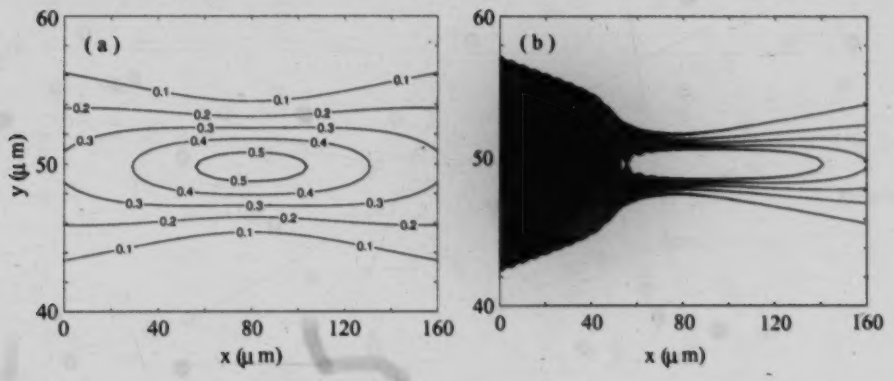

Figure 2.1: Intensity contour plots for a single Gaussian beam at different moments in time: $T = 0$ (a) and $T = 7ps$ (b). Parameters of the run are $I_0 = 1.46 \times 10^{15} W/cm^2, n_e/n_c = 0.4, f_\# = 4$.

dispersion relation of the plasma modes and if the wave intensity is large enough the result is the generation of parametric instabilities with parameter – the wave intensity.

The basic mechanism behind the parametric instabilities is the process of *wave coupling*, in which the incident pump wave drives other wave modes through coupling provided by the plasma. Then the daughter waves beat together so that their sum or difference of frequency and wave-numbers matches the frequency and the wavenumber of the driving wave. The process will be efficient only when the driver is strong enough to overcome the losses of the generated waves.

In an unmagnetized plasma there are three **principal modes** supported by the system:

- transverse electromagnetic wave $(\omega_0, \mathbf{k}_0)$ with frequency ω_0 and wave-vector $\mathbf{k}_0$ related by the dispersion relation:

$$\omega_0^2 = \omega_{pe}^2 + k_0^2 c^2, \tag{2.45}$$

where

$$\omega_{pe}^2 = \frac{4\pi n_{e0} e^2}{m}, \tag{2.46}$$

is the plasma frequency.

- longitudinal Langmuir wave $(\omega_L, \mathbf{k}_L)$ with dispersion relation:

$$\omega_L^2 = \omega_{pe}^2 + 3k_L^2 v_{Te}^2. \tag{2.47}$$

- low-frequency ion-acoustic wave $(\omega_s, \mathbf{k}_s)$ with dispersion relation:

$$\omega_s^2 = k_s^2 c_s^2. \tag{2.48}$$

There are many possible processes in which the driver wave decays into various combinations of principal plasma modes. For parameters where some of these processes can exist simultaneously, they influence each other. Typical examples for such influencing each other processes are SRS+SBS and SBS+FI. Figure (2.1) illustrates laser-plasma interaction that involves both SBS and SFI processes. It shows two intensity contour plots for the case of a Gaussian beam. The parameters for this particular run are $I_0 = 1.46 \times 10^{15} W/cm^2, n_e/n_c = 0.4$, $f_\# = 4$. Figure (2.1)(a) represents the intensity contour plot for the initial time, and Fig. (2.1)(b) is for the later instant at $T = 7ps$. Both contours are plotted for the contour levels indicated on part (a) of the figure. Figure (2.1)(b) shows the self-focussing of the laser beam. The left half of Fig. (2.1)(b) shows the typical picture of backward SBS.

In this study we confine ourselves to consider only low-frequency processes, i.e. processes involving ion dynamics. Such an involvement of the ions in propagation of light through a plasma encompasses both light scattering represented by SBS, and the change of the properties of the light as a result of self-focusing and filamentation. In the next two subsections we describe those instabilities in detail.

2.4.1 Stimulated Brillouin scattering

The first rigorous study of Brillouin scattering was performed for wave propagation in multidimensional lattices [9]. Later, because of its detrimental effect on light propagation in plasma, further extensive explorations by many researchers followed [see as ex. [21, 41, 12, 10] and the references therein].

When light propagates through a medium it scatters because of fluctuations in the optical properties of the medium. There are two groups of scattering processes, *spontaneous* and *stimulated*. Spontaneous scattering occurs when the optical properties of the material system are not changed by the presence of the incident light so the fluctuations that cause the scattering are only excited by thermal or quantum-mechanical effects. On the other hand, when the intensity of the incident light is sufficiently high to modify the optical properties of the medium, then the fluctuations are induced by the light field itself and the scattering process is termed stimulated.

The most important example of a process of stimulated light scattering due to induced density variations of the plasma is stimulated Brillouin scattering. The SBS process belongs to the family of parametric instabilities that can occur in the sub-critical region of a plasma irradiated by an incident laser beam. Common to all these processes is that the incident (pump) wave decays into two other waves through the coupling provided by the plasma.

As shown in Fig. (2.2) stimulated Brillouin scattering is a resonant process of three-wave coupling in which an incident wave of amplitude E_0, angular frequency ω_0, and wave vector $\mathbf{k}_0$, scatters off an ion-acoustic wave of amplitude δn_e, frequency ω_s, and wave vector $\mathbf{k}_0$, to form a reflected electromagnetic wave with amplitude E_1, and lower frequency ω_1 and wave vector $\mathbf{k}_1$.

The three waves involved in the interaction obey the laws of conservation of wave energy and momentum, as they are expressed in frequency and wavenumber

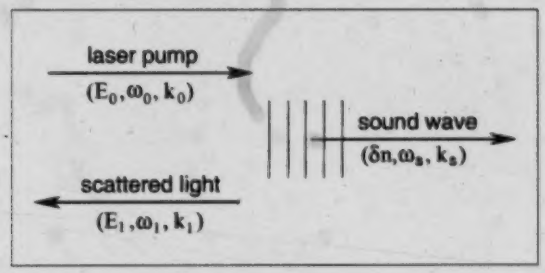

Figure 2.2: Schematic representation of the stimulated Brillouin scattering process.

matching conditions respectively:

$$\omega_0 = \omega_1 + \omega_s, \tag{2.49}$$

$$\mathbf{k}_0 = \mathbf{k}_1 + \mathbf{k}_s, \tag{2.50}$$

where $(\omega_0, \mathbf{k}_0)$ are the frequency and wave number of the pump wave, $(\omega_1, \mathbf{k}_1)$ – of the scattered wave and $(\omega_s, \mathbf{k}_s)$ – of the ion acoustic wave. Whether or not the resonant three-wave interaction will occur depends on the simultaneously satisfying of both the resonance conditions (2.49,2.50) and the dispersion relations (2.45,2.48). These conditions are conveniently represented in the dispersion $(\omega, \mathbf{k})$ diagram, Fig. (2.3).

The physical mechanism of SBS can be described as follows. The incident electromagnetic wave, E_0, couples to the initial plasma density perturbations, δn, leading to a scattered wave, E_1. The resulting field, E_0E_1, drives the electron oscillations via ponderomotive force, creating local charge imbalances. Ions, due to their large mass, do not respond directly to the driving field, but only through Coulomb coupling to the electrons. The local charge imbalances, because of the particle inertia, lead to a density ripple, δn, i.e. an ion acoustic wave. The enhanced density perturbation, δn couples to the incident pump wave, thus closing the instability loop. If the pump wave is intense enough, so that some threshold value is reached, the result will be back and side scattering from this

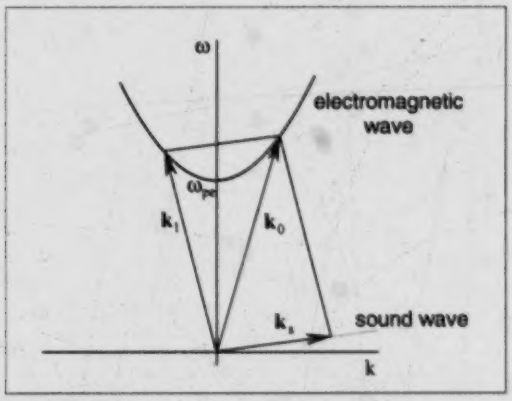

Figure 2.3: Frequency and wave vector matching conditions for the stimulated Brillouin scattering process.

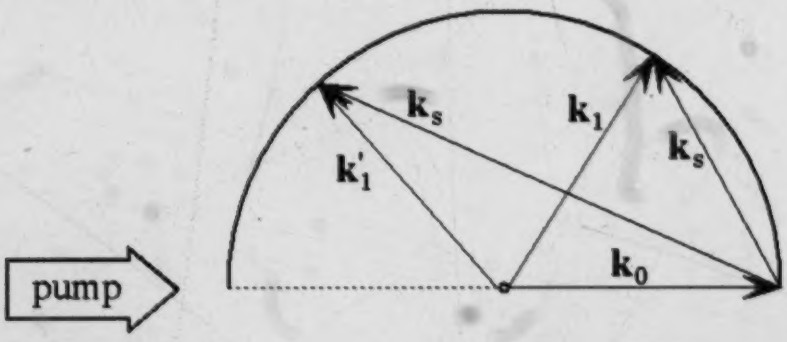

Figure 2.4: Polar plot of the stimulated Brillouin scattering process.

ion-acoustic wave (IAW) [cf. Fig. (2.4)].

Here one important point has to be made, namely that the scattering happens in a wide angle as shown on Fig. (2.4). The importance of an adequate description of the side scattering will be stressed later in Chapter 4.

Figure (2.5) shows the polar diagram of the growth rate in homogeneous infinite plasmas as a function of the scattering angle. It is clear that the maximum growth rate is for the backscattering direction. To initiate the instability, the presence of at least one of the two decay waves is needed at the beginning. Ac-

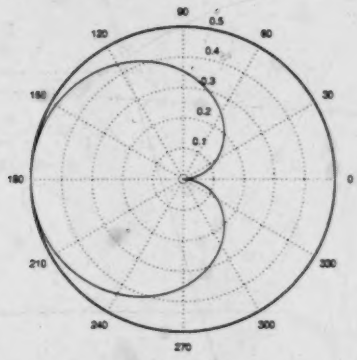

Figure 2.5: Polar plot of the stimulated Brillouin scattering growth rate as a function of scattering angle.

cordingly, if we borrow some terminology from nonlinear optics [8] the following two 'pure' cases are possible, namely SBS *generator* and SBS *amplifier*. In the first case, only the laser beam is applied externally, while both the secondary and the IAW grow from (thermal) noise in the interaction region. The secondary wave is created at frequencies near the one for which the gain coefficient is largest. In the second case, a small electromagnetic seed is applied externally. Strong coupling occurs only if the seed frequency is close to the resonant frequency.

In terms of the nonlinear optics, SBS involves the so called 'optical mixing' in which the pump wave beats with the secondary wave forming an amplitude modulated ('beat') electromagnetic wave. When the ponderomotive force produced by this wave is strong enough to drive the original ion-acoustic mode, then a feedback mechanism is established and the scattered wave and the IAW grow together.[‡]

We will review the effect of the ponderomotive force in greater detail in the next subsection.

[‡]Yet another way to express this process is in quantum- mechanical terms [28, 1] as the following two-way decay:
photon → *photon* + *plasmon*

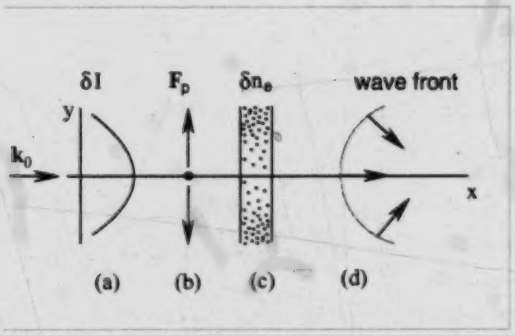

Figure 2.6: Sequence of events comprising ponderomotive self-focussing. Here δI is the nonuniform intensity of the electromagnetic field, $\mathbf{F}_p$ is the ponderomotive force and δn_e is the change in plasma density.

2.4.2 Ponderomotive self-focussing and filamentation

Self-focussing is a consequence of nonlinear plasma response through a change in the refraction index [30]. The nature of the self-focusing process is illustrated schematically in Fig. (2.6). Here an initial local increase of laser beam intensity δI, Fig. (2.6) (a), leads to change in the ponderomotive force, Fig. (2.6) (b),

$$\mathbf{F}_p = -\frac{1}{2}\nabla\left\langle\left(\frac{e\mathbf{A}}{mc}\right)^2\right\rangle. \tag{2.51}$$

The effect of the ponderomotive force is to expel the electrons from the region of higher field intensity, Fig. (2.6) (c), creating a plasma density depression in this region. The depletion of electrons increases the index of refraction [§]

$$n_{ref} = \sqrt{1-\left(\frac{\omega_{pe}}{\omega_0}\right)^2} = \sqrt{1-\left(\frac{n_e}{n_c}\right)^2}, \tag{2.52}$$

in the spot of higher intensity. This slows down the phase velocity of the light wave, increasing the optical thickness and thus creating a convex lens, Fig. (2.6)

[§]The filamentation can result from other mechanisms like *thermal force*, in which local heating leads to the same effect via plasma expansion [18], or *relativistic effects*, where a high 'quiver' velocity from a sufficiently strong laser induces a relativistic increase of the electron mass. In some cases those effects can coexist [34].

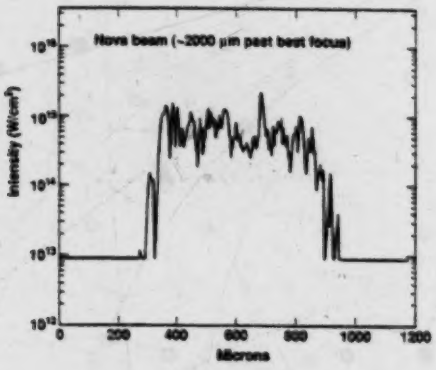

Figure 2.7: Typical experimental intensity cross section profile of filament driving beam. Reprinted from H. A. Baldis [5].

(d), which additionally increases the intensity of the spot. This closes the instability loop because the light intensity increases more in the places where it is higher. The process continues until the electron density is too small to effectively refract the beam [31].

The instability can be launched either by an initial density perturbation or by non-uniformities in the incident laser beam. The latter is possible because the spatial profile of a typical laser beam consists of numerous localized intensity peaks of different size [cf. Fig. (2.7)] that act as seed for filamentation.

Filamentation and self-focusing are two different manifestations of the same process, the former taking place when the beam diameter is larger than the scale of the transverse variations of density. The process of self-focusing as observed in simulations is illustrated on the second half of the contour plot in Fig. (2.1). The drastic decrease of the beam cross section along with the local increase of the beam intensity due to this process is more clearly seen in Fig. (2.8)(a). Figure (2.8)(b) illustrates the filamentation process for the same run at $T = 7ps$.

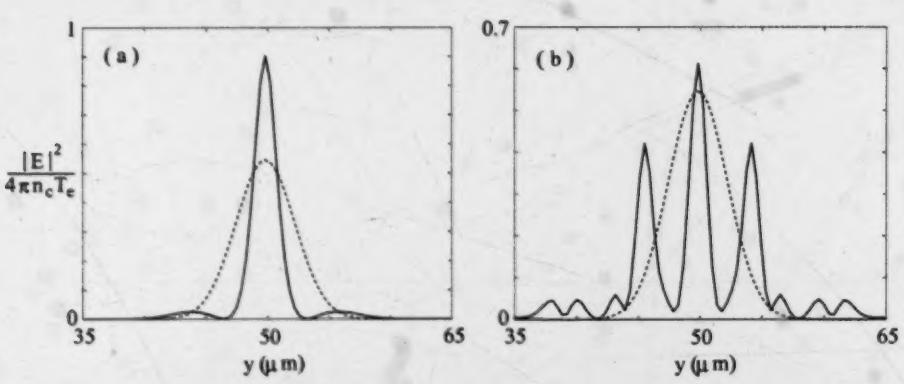

Figure 2.8: Comparison between self-focusing, (a), and filamentation, (b). Intensity contour plots for a single Gaussian beam at different moments in time: $T = 0$ (a) and $T = 7ps$ (b). Parameters of the run are $I_0 = 1.46 \times 10^{15} W/cm^2, n_e/n_c = 0.4$, $f_\# = 4$.

On both parts of Fig. (2.8), *a* and *b*, the beam intensity cross section at the initial time is shown for comparison with dashed lines. As we see, self-focusing leads to contraction of the whole beam cross section, Fig. (2.8)(a), while the filamentation instability result is to break the beam into localized intensity peaks, Fig. (2.8)(b).

Filamentation is a non-resonant four-wave process, (see Fig.(2.9)), in which the incident light wave, $\mathbf{k}_0$, decays into two counter-propagating ion waves, $\mathbf{k}_s'$ and $\mathbf{k}_s''$, and a forward-propagating light wave,$\mathbf{k}_1$. The ion waves have the same frequency and lead to a spatial modulation of the laser light.

Self-focusing can occur only if the beam power is sufficiently large. Otherwise the tendency of the beam to contract because the nonlinear change in refractive index will be suppressed by the tendency of the beam to spread due to diffraction effects.

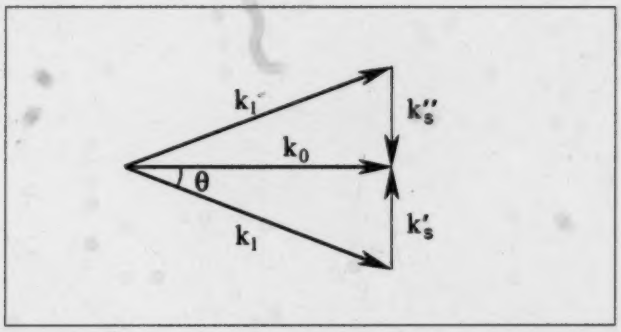

Figure 2.9: Schematic representation of the filamentation process.

2.5 Dispersion Relation

To derive the dispersion relation [16, 35] we use the Fourier transform defined as:

$$f(\mathbf{r},t) = \frac{1}{(2\pi)^2}\int d\mathbf{k}d\omega\, e^{i(\mathbf{k}\cdot\mathbf{r}-\omega t)}\tilde{f}(\mathbf{k},\omega), \tag{2.53}$$

$$\tilde{f}(\mathbf{k},\omega) = \frac{1}{(2\pi)^2}\int d\mathbf{r}dt\, e^{-i(\mathbf{k}\cdot\mathbf{r}-\omega t)}f(\mathbf{r},t), \tag{2.54}$$

Introducing the following linear differential operators

$$\hat{D}(\mathbf{r},t) = \frac{\partial^2}{\partial t^2} - c^2\nabla^2 + \omega_{pe}^2 + 2\gamma_E\frac{\partial}{\partial t}, \tag{2.55}$$

$$\hat{L}(\mathbf{r},t) = \frac{\partial^2}{\partial t^2} - c_s^2\nabla^2 + 2\gamma_{IA}\frac{\partial}{\partial t}, \tag{2.56}$$

where γ_E is the damping of the electromagnetic wave and γ_{IA} is the damping of the ion acoustic wave. We rewrite Eq. (2.26) and Eq. (2.44) with explicit variable dependence as

$$\hat{D}(\mathbf{r},t)\mathbf{A}_h(\mathbf{r},t) = -\omega_{pe}^2\delta n_e(\mathbf{r},t)\mathbf{A}_h(\mathbf{r},t), \tag{2.57}$$

$$\hat{L}(\mathbf{r},t)\delta n_e(\mathbf{r},t) = \frac{n_0Ze^2}{mMc^2}\nabla^2 < \mathbf{A}_h^2 > . \tag{2.58}$$

Representing the functions with their Fourier integrals

$$\hat{D}(\mathbf{r},t)\frac{1}{(2\pi)^2}\int d\mathbf{k}'d\omega'\; e^{i(\mathbf{k}'\cdot\mathbf{r}-\omega' t)}\tilde{\mathbf{A}}(\mathbf{k}',\omega') = \tag{2.59}$$

$$-\omega_{pe}^2\frac{1}{(2\pi)^4}\int d\mathbf{k}'d\omega'\ e^{i(\mathbf{k}'\cdot\mathbf{r}-\omega' t)}\delta\tilde{n}_e(\mathbf{k}',\omega')\int d\mathbf{k}''d\omega''\ e^{i(\mathbf{k}''\cdot\mathbf{r}-\omega'' t)}\tilde{\mathbf{A}}(\mathbf{k}'',\omega''),$$

$$\hat{L}(\mathbf{r},t)\frac{1}{(2\pi)^2}\int d\mathbf{k}'d\omega'\ e^{i(\mathbf{k}'\cdot\mathbf{r}-\omega' t)}\delta\tilde{n}_e(\mathbf{k}',\omega') = \tag{2.60}$$

$$\frac{n_0Ze^2}{mMc^2}\frac{1}{(2\pi)^2}\nabla^2\left\langle\int d\mathbf{k}'d\omega'\ e^{i(\mathbf{k}'\cdot\mathbf{r}-\omega' t)}\tilde{\mathbf{A}}_h(\mathbf{k}',\omega')\cdot\int d\mathbf{k}''d\omega''\ e^{i(\mathbf{k}''\cdot\mathbf{r}-\omega'' t)}\tilde{\mathbf{A}}_h(\mathbf{k}'',\omega'')\right\rangle.$$

The differential operators $\hat{D}$ and $\hat{L}$ in Fourier space yield the quantities:

$$D(k,\omega) = -\omega^2+k^2c^2+\omega_{pe}^2-2i\omega\gamma_E, \tag{2.61}$$

$$L(k,\omega) = -\omega^2+k^2c_s^2-2i\omega\gamma_{IA}. \tag{2.62}$$

where

$$\gamma_E=\frac{\omega_{pe}^2}{\omega^2}\frac{\nu_{ei}}{2},$$

and ν_{ei} is the collision frequency for electron scattering by ions [35]. Taking the inverse Fourier transform of Eq. (2.61) and changing the integration order we obtain

$$D(\mathbf{k},\omega)\tilde{\mathbf{A}}_h(\mathbf{k},\omega) = \tag{2.63}$$

$$-\omega_{pe}^2\frac{1}{(2\pi)^2}\int d\mathbf{k}''d\omega''\ \delta\tilde{n}_e(\mathbf{k}-\mathbf{k}'',\omega-\omega'')\tilde{\mathbf{A}}_h(\mathbf{k}'',\omega''),$$

$$L(\mathbf{k},\omega)\delta\tilde{n}_e(\mathbf{k},\omega) = \tag{2.64}$$

$$\frac{n_0Ze^2}{mMc^2}\frac{1}{(2\pi)^2}(-k^2)\int d\mathbf{k}''d\omega''\ \left\langle\tilde{\mathbf{A}}_h(\mathbf{k}-\mathbf{k}'',\omega-\omega'')\cdot\tilde{\mathbf{A}}_h(\mathbf{k}'',\omega'')\right\rangle,$$

where the definition and properties of the δ-function were used [32]

$$\delta(\mathbf{k},\omega)\equiv\delta(k_x)\delta(k_y)\delta(k_z)\delta(\omega)=\frac{1}{(2\pi)^4}\int d\mathbf{r}dte^{-i(\mathbf{k}\cdot\mathbf{r}-\omega t)}. \tag{2.65}$$

To be able to resolve the integral in the r.h.s. of Eq. (2.63) and Eq. (2.64) we assume that the driver $\mathbf{A}_0$ is a plane wave with wave number $\mathbf{k}_0$ and frequency ω_0

$$\mathbf{A}_h(\mathbf{r},t)=\mathbf{A}_0\cos(\mathbf{k}_0\cdot\mathbf{r}-\omega_0 t)=\frac{\mathbf{A}_0}{2}\left(e^{i(\mathbf{k}_0\cdot\mathbf{r}-\omega_0 t)}+e^{-i(\mathbf{k}_0\cdot\mathbf{r}-\omega_0 t)}\right). \tag{2.66}$$

Its Fourier transform

$$\tilde{\mathbf{A}}_h(\mathbf{k}'',\omega'') = \frac{\mathbf{A}_0}{2}\frac{1}{(2\pi)^2}\int d\mathbf{r}dt\left[e^{i(\mathbf{k}_0-\mathbf{k}'')\cdot\mathbf{r}-i(\omega_0-\omega'')t} + e^{i(-\mathbf{k}_0-\mathbf{k}'')\cdot\mathbf{r}-i(-\omega_0-\omega'')t}\right], \tag{2.67}$$

after the integration takes the form

$$\tilde{\mathbf{A}}_h(\mathbf{k}'',\omega'') = \frac{\mathbf{A}_0}{2}\left(\delta(\mathbf{k}_0-\mathbf{k}'',\omega_0-\omega'') + \delta(\mathbf{k}_0+\mathbf{k}'',\omega_0+\omega'')\right). \tag{2.68}$$

Substituting Eq. (2.68) into Eq. (2.63) and Eq. (2.64) yields

$$D(\mathbf{k},\omega)\tilde{\mathbf{A}}_h(\mathbf{k},\omega) = \tag{2.69}$$
$$-\omega_{pe}^2\frac{\mathbf{A}_0}{2}\left(\delta n_e(\mathbf{k}-\mathbf{k}_0,\omega-\omega_0) + \delta n_e(\mathbf{k}+\mathbf{k}_0,\omega+\omega_0)\right)$$
$$L(\mathbf{k},\omega)\delta\tilde{n}_e(\mathbf{k},\omega) = \tag{2.70}$$
$$\frac{n_0Ze^2}{mMc^2}(-k^2)\frac{\mathbf{A}_0}{2}\cdot\left(\tilde{\mathbf{A}}_h(\mathbf{k}-\mathbf{k}_0,\omega-\omega_0) + \tilde{\mathbf{A}}_h(\mathbf{k}+\mathbf{k}_0,\omega+\omega_0)\right).$$

Adding the expressions of Eq. (2.69) for both down-shifted and up-shifted arguments, $\mathbf{k}\pm\mathbf{k}_0, \omega\pm\omega_0$, and neglecting the non-resonant terms, $\delta\tilde{n}_e(\mathbf{k}\pm2\mathbf{k}_0, \omega\pm2\omega_0)$, we obtain the following sum:

$$\tilde{\mathbf{A}}_h(\mathbf{k}+\mathbf{k}_0,\omega+\omega_0) + \tilde{\mathbf{A}}_h(\mathbf{k}-\mathbf{k}_0,\omega-\omega_0) = \tag{2.71}$$
$$\omega_{pe}^2\frac{\mathbf{A}_0}{2}\delta\tilde{n}_e(\mathbf{k},\omega)\left(\frac{1}{D(\mathbf{k}-\mathbf{k}_0,\omega-\omega_0)} + \frac{1}{D(\mathbf{k}+\mathbf{k}_0,\omega+\omega_0)}\right).$$

We next use this expression to obtain the dispersion relation from Eq. (2.70):

$$\omega^2 - k^2c_s^2 + 2i\omega\gamma_{IA} = \tag{2.72}$$
$$\frac{k^2v_{os}^2}{4}\omega_{pi}^2\left(\frac{1}{D(\mathbf{k}-\mathbf{k}_0,\omega-\omega_0)} + \frac{1}{D(\mathbf{k}+\mathbf{k}_0,\omega+\omega_0)}\right),$$

where

$$\omega_{pi} = \omega_{pe}\sqrt{\frac{Zm}{M}}, \tag{2.73}$$

is the ion plasma frequency and

$$\mathbf{v}_{os} = \frac{e\mathbf{A}_0}{mc}, \tag{2.74}$$

is the electron quiver velocity.

The dispersion relation, Eq. (2.72), describes both SBS and FI. In the next two subsections we derive some important linear characteristics for these, on the basis of this dispersion relation.

2.5.1 Stimulated Brillouin scattering

We concentrate on the backscatter SBS, because it has the largest growth rate. In this case $\mathbf{k} \sim 2\mathbf{k}_0$, $D(\mathbf{k}+\mathbf{k}_0, \omega+\omega_0)$ is non-resonant, so only the down-shifted wave, $D(\mathbf{k}-\mathbf{k}_0, \omega-\omega_0)$, is retained and Eq. (2.72) simplifies to

$$\left(\omega^2 - k^2c_s^2 + 2i\omega\gamma_{IA}\right)\left(\omega^2 - 2\omega\omega_0 + 2\mathbf{k}\cdot\mathbf{k}_0c^2 - k^2c^2 - i\omega_{pe}^2\frac{\nu_{ei}}{\omega-\omega_0}\right) = \frac{k^2v_{os}^2}{4}\omega_{pi}^2, \tag{2.75}$$

where the dispersion relation for the pump wave,Eq. (2.45), was taken into account. The quantities in the first bracket correspond to dispersion relation of free ion-acoustic waves.

In the weakly coupling limit, where the frequency

$$\omega = kc_s + \Delta\omega,$$

is a real quantity, and allowing the wave vector, $\mathbf{k}$, to be a complex quantity

$$k = k_r + ik_i,$$

we can simplify Eq. (2.75) considerably. Taking into account $\omega \ll \omega_0$ the dispersion relation reduces to

$$(2i\gamma kc_s + 2ikc_s\gamma_{IA})\left(-2(kc_s + i\gamma)\omega_0 + 2kk_0c^2 - k^2c^2 + i2\omega_0\gamma_E\right) = \frac{k^2v_{os}^2}{4}\omega_{pi}^2, \tag{2.76}$$

where the damping of the electromagnetic wave, γ_E, is defined as

$$\gamma_E = \frac{\omega_{pe}^2}{\omega_0^2}\frac{\nu_{ei}}{2}$$

The real part of the expression in the second bracket of Eq. (2.76) is zero when

$$\gamma^2 + (\gamma_{IA} + \gamma_E)\gamma + \gamma_{IA}\gamma_E - \frac{k^2 v_{os}^2}{16\omega_0 c_s}\omega_{pi}^2 = 0, \tag{2.77}$$

Solving this quadratic equation for γ leads to the requirement

$$\frac{k^2 v_{os}^2}{16\omega_0 c_s}\omega_{pi}^2 > \gamma_{IA}\gamma_E, \tag{2.78}$$

So the *threshold* value for SBS is given by the condition:

$$v_{os}^2 = 8\frac{\gamma_{IA}\gamma_E}{\omega_{pi}^2}\frac{\omega_0}{k}c_s > 0 \tag{2.79}$$

2.5.2 Filamentation instability

The FI corresponds to growth of zero-frequency perturbations of plasma density in the direction perpendicular to the propagation of the light wave, i.e. $\mathbf{k}\cdot\mathbf{k}_0 = 0$. Assuming

$$\omega = i\gamma \quad \ll \omega_0 \tag{2.80}$$

equation Eq. (2.61) simplifies to

$$D(\mathbf{k} \pm \mathbf{k}_0, \omega \pm \omega_0) = \pm 2i\omega_0(\gamma + \gamma_E) - k^2 c^2, \tag{2.81}$$

and from Eq. (2.72), after some algebraic manipulations we obtain

$$\left(\gamma^2 + k^2 c_s^2\right)\left((\gamma + \gamma_E)^2 + \frac{k^4 c^2}{4\omega_0}\right) = \frac{k^4 v_{os}^2 c^2}{8}\frac{\omega_{pi}^2}{\omega_0^2}. \tag{2.82}$$

In the limit of

$$\gamma \ll k c_s,$$

this equation, Eq. (2.82), can be rewritten as:

$$(\gamma + \gamma_E)^2 = \frac{v_{os}^2}{8}\frac{c^2}{c_s^2}\frac{\omega_{pi}^2}{\omega_0^2}k^2 - \frac{k^4 c^4}{4\omega_0^2}. \tag{2.83}$$

To determine the maximum growth rate, we differentiate the last equation with respect to k and solve for $\partial\gamma/\partial k = 0$. The result is

$$k = \frac{\omega_{pe}}{2c}\frac{v_{os}}{v_{Te}}, \tag{2.84}$$

where we have taken into account the relation Eq. (2.73).

Substituting Eq. (2.84) into Eq. (2.83) and again using the relation $\omega_{pi}/c_s = \omega_{pe}/v_{Te}$ we obtain for the growth rate:

$$\gamma = \sqrt{\frac{1}{8}\left(\frac{v_{os}}{v_{Te}}\right)^2 \frac{\omega_{pe}^2}{\omega_0^2}} - \gamma_E, \tag{2.85}$$

i.e. the density fluctuations are purely growing. The threshold condition $\gamma = 0$ is reached when

$$v_{os}^2 = 8v_{Te}^2 \frac{\omega_0^2}{\omega_{pe}^2}\gamma_E. \tag{2.86}$$

Since there is no resonance with the ion wave, the FI is not very sensitive to plasma inhomogeneity.

Now let us consider again the case where the frequency is real and the wavenumber has real, k_r, and imaginary, k_i, parts

$$k_s = k_r + ik_r.$$

Substituting this expression into Eq. (2.72) we obtain

$$4k_i^2k_0^2 + k_r^4 - k_r^2\frac{\omega_{pe}^2}{c^2}\frac{v_{os}^2}{2v_{Te}^2} = 0.$$

If we solve for k_i

$$k_i^2 = \frac{1}{4k_0^2}\left(k_r^2\frac{\omega_{pe}^2}{c^2}\frac{v_{os}^2}{2v_{Te}^2} - k_r^2\right)$$

and use the condition $\partial k_i/\partial k_r = 0$, then

$$k_i = \frac{1}{8}\left(\frac{v_{os}}{v_{Te}}\right)^2\left(\frac{\omega_{pe}^2}{k_0c^2}\right).$$

Substituting for $k_{r,max}$ we obtain

$$\theta \approx \frac{1}{2}\left(\frac{\omega_{pe}}{\omega_0}\right)\left(\frac{v_{os}}{v_{Te}}\right). \tag{2.87}$$

It can be noted that the angle θ increases with an increase of plasma density ($\omega_{pe}^2/\omega_0 = n_e/n_c$) and with an increase of intensity of the laser beam ($v_{Te} \sim \sqrt{I}$).

This concludes the linear analysis of dispersion relations for SBS and FI. The next section describes the numerical code used in the simulations.

2.6 Numerical Code

The numerical code is based on Eq. (2.26) and Eq. (2.44) written for the time enveloped amplitude of the real field. The discretization scheme uses the mathematical framework of the spectral methods [11] adapted for equations of Zakharov's type [39].

Spectral methods were initially developed for computationally intensive applications in fluid dynamics and showed superior accuracy and very low phase error. They belong to the class of numerical methods based on the method of weighted residuals (MWR) [42]. In MWR a set of infinitely differentiable global *trial functions* serves as a basis for a truncated series expansion of the solution. The error introduced by approximating the complete solution with the truncated expansion, i.e. the residual, is minimized with the help of an additional set of *test functions* and a suitably defined inner product. The choice of those test functions leads to different versions of the spectral method, such as Galerkin, collocation and tau methods and combinations of these.

The particular choice of test functions is usually dictated by the boundary conditions of the problem. In our approach we assume periodicity in the direction perpendicular to the direction of propagation of the laser light, and use of Fourier approximation. In the longitudinal direction we apply the tau method, which

is suitable for non-periodic boundary conditions [25]. The method requires that the integral of the residual times each test function be zero. An additional set of equations is used to incorporate the boundary conditions as described below.

The discretization in time involves a modification of an implicit midpoint scheme supplemented by Euler preconditioning and an iterative improvement of the nonlinear terms.[40]

2.6.1 Model Equations

The mathematical model used in the computer simulations consists of the electromagnetic wave equation, Eq. (2.26), and the ion-acoustic wave equation, Eq. (2.44), written for the electric field amplitude [19, 20].

We consider and electromagnetic wave propagating in z-direction. The electric field of the electromagnetic wave is assumed polarized along the z-axis and enveloped in time with respect to the laser frequency ω_0 [22, 3]

$$E(\mathbf{x},t) = \frac{1}{2}\left\{E(y,z,t)e^{-i\omega_0 t} + c.c.\right\}.$$

Taking into account that the time dependence of the electric field,E, Eq. (2.6.1), is the same as the time dependence of the vector potential, $\mathbf{A}$, Eq. (2.66), we can use Eq. (2.26) and find that the electric field amplitude satisfies the following equation:

$$\left[2i\frac{\omega_0}{c^2}\frac{\partial}{\partial t} + \nabla^2 + \frac{\omega_0^2}{c^2}\left(1 - \frac{n_e}{n_c}\right)\right]E = \frac{\omega_0^2}{c^2}\frac{\delta n_e}{n_c}E, \tag{2.88}$$

which corresponds to a scalar field approximation in 2D and the Laplace's operator has the form

$$\nabla^2 = \partial^2/\partial y^2 + \partial^2/\partial z^2.$$

The electron density perturbation, δn_e,

$$\delta n_e(y,z,t) = n_e(y,z,t) - n_{e0}(y,z), \tag{2.89}$$

where the critical density

$$n_c = \frac{m\omega_0^2}{4\pi e^2}, \tag{2.90}$$

is driven by the ponderomotive force. Similarly, taking into account the relation between the electric field and vector potential, one can obtain from Eq. (2.44) the second equation of the system, namely the acoustic wave equation:

$$\left[\frac{\partial^2}{\partial t^2} + 2\gamma_{IA}\frac{\partial}{\partial t} - c_s^2\nabla^2\right] \ln\left(1 + \frac{\delta n_e}{n_e}\right) = \frac{c_s^2}{16\pi n_c T_e}\nabla^2|E|^2, \tag{2.91}$$

with the logarithmic term introduced to ensure nonlinear saturation of the amplitude of the density perturbations[37, 43, 27]. The term $2\gamma_{IA}$ models the damping of the ion density fluctuations and allows independent control of ion acoustic waves propagating in different directions [2].

The set of equations Eq. (2.88) and Eq. (2.91) describes SBS, filamentation and self-focusing instabilities of the incident laser beam and the interaction between them.

2.6.2 Discretization scheme

We solve equations 2.91 and 2.88 numerically in a two-dimensional (2D) Cartesian geometry region, cf. Fig.(2.10)

$$(y, z) \in [0, L_y] \times [0, L_z].$$

Adopting periodicity in the transverse direction we can define N_y grid points y_j in configuration space by:

$$y_j = j\frac{L_y}{N_y}, \qquad j = 0, ..., N-1.$$

Then we can expand the electric field E and the ion density perturbation δn_e in Fourier series in the perpendicular direction, y, as follows:

$$\begin{aligned} E(y_j, z, t) &= E_j(z, t) = \sum_m E_m(z, t)e^{ik_m y_j}, \\ \delta n_e(y_j, z, t) &= N_j(z, t) = \sum_m N_m(z, t)e^{ik_m y_j}, \end{aligned}$$

where:

$$k_m = m\delta k, \qquad \delta k = \frac{2\pi}{L_y} = \frac{k_0\lambda_0}{L_y},$$

and $\lambda_0 = 2\pi/k_0$ is the free-space wavelength of the incident electromagnetic wave. The index m enumerates all the modes considered in the simulations.

Substituting these into equations and introducing the following dimensionless variables:

$$\begin{aligned} T &= \beta\omega_0 t, \\ Y &= k_0 y, \\ Z &= k_0 z, \\ E &= \frac{E(y,z,t)}{\sqrt{4\pi n_c T_e}}, \end{aligned} \tag{2.92}$$

where $\beta = c_s/c$ is the dimensionless sound velocity, one obtains the following set of PDEs for the Fourier components:

$$\begin{aligned} \left[2i\beta\frac{\partial}{\partial T} + \frac{\partial^2}{\partial Z^2} + K_{zm}^2\right] E_m &= \sum_n E_{m-n}N_n, \\ \left[\frac{\partial^2}{\partial T^2} + 2\gamma_s\frac{\partial}{\partial T} - \frac{\partial^2}{\partial Z^2} + k_{m0}^2\right] N_m &= \frac{N_0}{4}\left[\frac{\partial^2}{\partial Z^2} - k_{m0}^2\right]\sum_n E_{m+n}E_n^*. \end{aligned}$$

The boundary conditions for the E_m field in z direction are given by

$$\begin{aligned} \left(\frac{\partial E_m}{\partial Z}\right)_{Z=0} &= iK_{zm}\left(2E_m^0(T) - E_m(0,T) + \frac{i\beta}{K_{zm}^2}\frac{\partial}{\partial T}\left[E_m^0(T) - E_m(0,T)\right]\right), \\ \left(\frac{\partial E_m}{\partial Z}\right)_{Z=L_z} &= iK_{zm}\left(1 + \frac{i\beta}{K_{zm}^2}\frac{\partial}{\partial T}\right)E_m(L_z,T), \end{aligned}$$

where E_m^0 are the (known) harmonics of the incident electric field and

$$\begin{aligned} K_{zm}^2 &= \cos^2\theta_m - N_0, \\ \cos^2\theta_m &= 1 - (mq/k_0)^2. \end{aligned}$$

The boundary conditions for the ion-acoustic wave equations are:

$$\left(\frac{\partial\delta N_m}{\partial Z}\right)_{Z=0} = \frac{\partial}{\partial T}\delta N_m(0,T) + \Gamma_{IA}^m\delta N_m(0,T)),$$

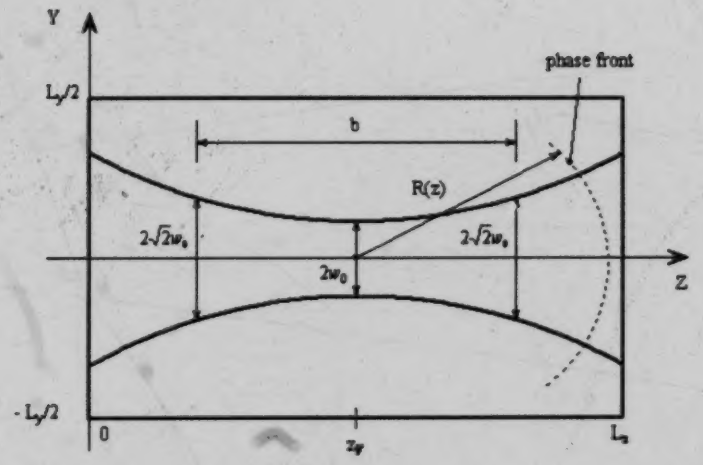

Figure 2.10: Geometry of the computational box used for the numerical calculations.

$$\left(\frac{\partial \delta N_m}{\partial Z}\right)_{Z=L_z} = -\frac{\partial}{\partial T}\delta N_m(L_z,T) - \Gamma_{IA}^m \delta N_m(L_z,T)),$$

where Γ_{IA} models the damping of ion density fluctuations.

The next step is discretization in the z-direction which is performed by employing the spectral Tau method using an expansion in Chebyshev's polynomials. Chebyshev's polynomials of first kind, $T_k(x)$, are cosine functions after a change of independent variable

$$T_k(x) = \cos k\theta, \quad \theta = \arccos x.$$

The Chebyshev's expansion of a function $u \in L_w^2(-1,1)$ is

$$u(x) = \sum_{k=0}^{\infty} \hat{u}_k T_k(x). \tag{2.93}$$

Here $u \in L_w^2(-1,1)$ is the complex Hilbert space with inner product defined as

$$(u,v) = \int_{-1}^{1} u(x)v^*(x)dx, \tag{2.94}$$

over the classes of functions $u : (-1,1) \to \mathcal{C}$ such that $|u|^2$ is Lebesgue-integrable over the interval $(-1,1)$ with a weight w. The expansion coefficients $\hat{u}_k$ are given

by

$$\hat{u}_k = \frac{2}{\pi c_k} \int_{-1}^{1} u(x) T_k(x) w(x) dx, \tag{2.95}$$

where

$$c_k = \begin{cases} 2, & if \quad k = 0 \\ 1, & if \quad k \geq 1. \end{cases}$$

In order to simulate laser beams with complicated distribution of the electric field propagating in large plasmas, it was necessary to develop a parallel version of the code. For this purpose we used the OpenMP Fortran Application Program Interface and implemented a version of the single-program multiple-data (SPMD) parallelism. We applied a large-grain parallelization using dynamic multi-threading and work-sharing directives for splitting the most time-consuming program loops.

2.7 Laser beam characteristics

The characteristics of the laser beam are of primary importance in the laser-plasma interaction process [44]. The principal scheme of an system is shown in Fig.(2.11). The primary light source is a laser beam having a Gaussian intensity profile. To an obtain an analytical expression for a Gaussian beam we begin with the wave equation Eq. (2.23), which in free space has the following form

$$\left(\frac{\partial^2}{\partial t^2} - c^2 \nabla^2 \right) A = 0. \tag{2.96}$$

It has a solution in the form of a plane monochromatic wave of frequency ω and wave vector $\mathbf{k}$:

$$A(\mathbf{r}, t) = const \cdot e^{i(\mathbf{k} \cdot \mathbf{r} - \omega t)}. \tag{2.97}$$

We can use this result to obtain a solution for a laser beam which has a finite diameter by looking for a solution of the form

$$A(\mathbf{r}, t) = V(\mathbf{r}) e^{i(kz - \omega t)}, \tag{2.98}$$

where $V(\mathbf{r})$ is a function that is slowly varying as compared to $\exp(i\mathbf{kr})$ when $\mathbf{k} = (0, 0, k)$. The oscillation frequency is a given by ω. By substituting Eq. (2.98) into Eq. (2.96) we obtain

$$\nabla^2 V + 2ik\frac{\partial V}{\partial z} + \left(\frac{\omega^2}{c^2} - k^2\right) V = 0. \tag{2.99}$$

We can neglect the term $\partial^2 V/\partial z^2$ because

$$\left|\frac{\partial^2 V}{\partial z^2}\right| \ll 2k\left|\frac{\partial V}{\partial z}\right|, \tag{2.100}$$

under the assumption of the slow spatial variation of V. This is the condition for the so-called paraxial approximation. Since k is arbitrary, we can choose it to be $k = \omega/c$, so that Eq. (2.99) simplifies to the paraxial wave equation:

$$i\frac{\partial V}{\partial z} + \frac{1}{2k}\left(\frac{\partial^2 V}{\partial x^2} + \frac{\partial^2 V}{\partial y^2}\right) = 0. \tag{2.101}$$

We will show that the paraxial wave equation, Eq. (2.101), has a solution of the following general Gaussian form:

$$V(\mathbf{r}) = Ce^{iS(z)}e^{-(x^2+y^2)/a(z)}, \tag{2.102}$$

where C is an arbitrary complex constant, and $S(z)$ and $a(z)$ are complex functions to be determined below. Substituting for V into Eq. (2.101) gives

$$\frac{x^2 + y^2}{a^2(z)}\left(2 + ik\frac{da}{dz}\right) + \frac{2}{a(z)} + k\frac{dS}{dz} = 0. \tag{2.103}$$

The assumption that S and a are functions of z only leads to the constraint

$$ikda/dz = -2, \tag{2.104}$$

so that Eq. (2.103) reduces to

$$dS/dz = -(2/k)1/a(z). \tag{2.105}$$

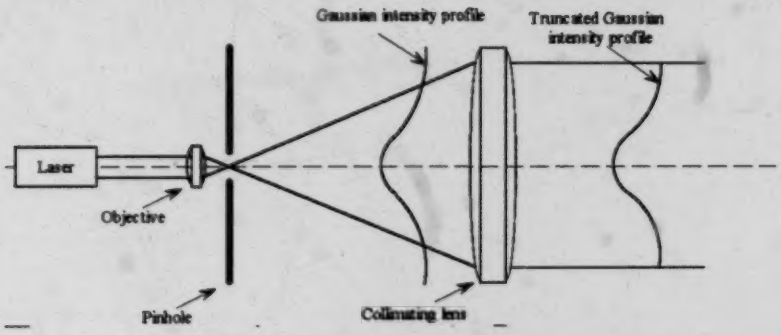

Figure 2.11: Basic optical processing system.

By introducing the notation

$$a(z) = -(2/ik)q(z), \tag{2.106}$$

the last two equations are represented as

$$dq/dz = 1, \tag{2.107}$$

$$dS/dz = i/q. \tag{2.108}$$

From here we obtain by integration:

$$q(z) = z + q_0, \tag{2.109}$$

$$S(z) = i\ln(z + q_0) + S_0, \tag{2.110}$$

where q_0 and S_0 are complex constants. From Eq. (2.109) it follows that for the origin of the coordinate system q is purely imaginary, i.e. can be represented as $q_0 = -i\alpha$, where α is a real quantity. Next we write $1/q$ as a sum of real and imaginary parts

$$\frac{1}{q(z)} = \frac{1}{R(z)} + i\frac{\lambda}{\pi}\frac{1}{w^2(z)} \tag{2.111}$$

where

$$R(z) = \frac{z^2 + \alpha^2}{z},\ w^2(z) = \frac{\lambda}{\pi}\frac{z^2 + \alpha^2}{\alpha}, \tag{2.112}$$

are called the radius of curvature and the radius of field distribution respectively, and $\lambda = 2\pi/k$ is the wavelength of the radiation. From Eq. (2.102) the cross section variation of the beam amplitude is characterized by

$$\exp\left(-\frac{r^2}{a(z)}\right) = \exp\left(-\frac{r^2}{w^2(z)}\right) = \exp\left(-\frac{\pi}{\lambda}r^2\frac{\alpha}{z^2+\alpha^2}\right), \tag{2.113}$$

where $r = \sqrt{x^2+y^2}$ is the radial distance. It is clear that to have a beam of limited diameter, it is necessary for α to be positive. Also, at $w(z) = r$, the beam amplitude decreases by e-times, so $w(z)$ can be considered an effective beam radius. It has a minimum of $\omega_0 = \lambda\alpha/\pi$ at the beam waist. With this value, the radius of curvature, R, and the radius of field distribution,ω, can be represented as

$$R(z) = z[1+(\pi\omega_0^2/\lambda z)^2], \tag{2.114}$$

$$w(z) = w_0[1+(\lambda z)/\pi\omega_0^2)^2]^{1/2}. \tag{2.115}$$

Similarly, from Eq. (2.110) we find:

$$S(z) = i\ln(z - i\pi w_0^2/\lambda) + S_0. \tag{2.116}$$

So the final form of the Gaussian beam looks like

$$A(r,z,t) = C\frac{w_0}{w(z)}exp\left(-\frac{r^2}{w^2(z)}\right)exp\left(i\frac{kr^2}{2R(z)}\right)e^{i\phi(z)}e^{i(kz-\omega t)}, \tag{2.117}$$

where

$$\phi(z) = \arctan(\lambda z/\pi w_0^2), \tag{2.118}$$

represents the spatial variation of the phase of the wave.

Sometimes a more compact form of the Gaussian beam is used

$$A(r,z) = \frac{C}{1-i\zeta}exp\left(-\frac{r^2}{w_0^2(1+i\zeta)}\right), \tag{2.119}$$

where $\zeta = 2z/b$ is a dimensionless coordinate, defined in terms of the confocal parameter $b = kw_0^2$ [cf. Fig.(2.10)].

The total power of the Gaussian beam is proportional to its intensity

$$I = |A|^2 = \frac{C^2}{w^2(z)} exp\left(-\frac{2r^2}{w^2(z)}\right), \tag{2.120}$$

and can be calculated by integrating over the transverse beam cross section

$$P = \int_{-\infty}^{\infty}\int_{-\infty}^{\infty} I dx dy = 2\pi \int_0^{\infty} |A|^2 r dr = \frac{\pi}{2}|C|^2. \tag{2.121}$$

The solution Eq. (2.117) was obtained by neglecting the second derivative in z, Eq. (2.100). By using Eq. (2.117), it can be shown that a Gaussian beam does not well describe the electromagnetic wave focusing in the region where the spot size is comparable to the wavelength of the radiation. In addition, the solution is not accurate for large distances from the z-axis, although the beam power in that distant region is negligible.

For cases when the laser beam diameter is too small for direct use, the light is directed through a beam-expanding module, the objective shown in Fig.(2.11). It consists of a light diverging objective, a pinhole that removes the diffracted light and collimating lens, which converts the divergent wave front into a plane wave. The amount of optical power collected within a collimating lens of radius R is

$$P = I_0 \int_0^R r dr \int_0^{2\pi} d\theta e^{-r^2/2\sigma^2} = 2\pi\sigma^2 I_0 \left(1 - e^{-R^2/2\sigma^2}\right). \tag{2.122}$$

As we see, the finite radius of the collimating lens restricts the amount of available light $2\pi\sigma^2 I_0$ by a factor of $e^{-R^2/2\sigma^2}$.

A commonly used measure for characterizing laser beams stems from lens optics, where $f_\#$ measures the focal length F in units of aperture size

$$f_\# = F/L. \tag{2.123}$$

An alternative definition of $f_\#$ is through the Gaussian intensity distribution [17]. For this purpose we can redefine the latter as follows:

$$I(\mathbf{x}) = I_0 \exp\left(\frac{-|\mathbf{x} - \mathbf{x}_F|^2}{f_\#^2 \lambda_0^2}\right) \tag{2.124}$$

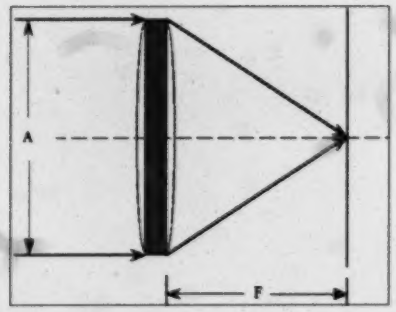

Figure 2.12: Focusing of light by a lens of aperture L and focal length F.

where $\lambda_0 = 2\pi c/\omega_0$ is the laser wavelength in vacuum. So here the dimensionless parameter $f_\#$ is defined as the ratio of the beam waist-radius to the laser vacuum wavelength λ_0. It determines the Rayleigh length, which is given by

$$L_R = 2\pi f_\#^2 \lambda_0 \sqrt{1 - n_e/n_c}. \tag{2.125}$$

This represents the distance from the best focus position to the point along the direction of propagation where the laser beam intensity decreases by a factor of 2 in 3D geometry.

Bibliography

[1] A. A. Abrikosov, L. P. Gorkov, and I. E. Dzyaloshinski Methods of Quantum Field Theory in Statistical Physics, Dover Publications, 1963.

[2] M. R. Amin, D. E. Capjack, P. Frycz, W. Rozmus, and V. T. Tikhonchuk, Phys. Fluids B, **5**, 3748 (1993).

[3] A. A. Andreev, N. E. Andreev, A. N. Sutyagin, V. T. Tikhonchuk, Sov.J.Plasma Phys. **15**, 546 (1989).

[4] A. I. Akhiezer, I. A. Akhiezer, K. V. Polovin, A. G. Sitenko, and K. N. Stepanov, Plasma Electrodynamics, Pergamon Press, 1975.

[5] H. A. Baldis, E. M. Campbell, and W. L. Kruer, Laser Plasma Interactions, preprint, LANL, 1990.

[6] G. C. Baldwin Introduction to Nonlinear Optics, Plenum Press, New York and London, 1969.

[7] R. Balesku, Statistical Mechanics of Charged Particles, John Wiley & Sons, 1963.

[8] R. W. Boyd, Nonlinear Optics, Academic Press, Boston, 1987.

[9] L. Brillouin, Wave Propagation in Periodic Structures, Second edition, Dover Publications, 1953.

[10] J. Candy, W. Rozmus, and V. T. Tikhonchuk, Phys. Rev. Lett, **65**, 1889 (1990).

[11] C. Canuto, M. Y. Hussaini and A. Quarteroni, Spectral Methods in Fluid Dynamics, Springer-Verlag, 1988.

[12] M. Casanova, G. Laval, R. Pellat, and D. Pesme, Phys. Rev. Lett. **54**, 2230 (1985).

[13] P. C. Clemmov, and J. P. Dougherty, Electrodynamics of Particles and Plasmas, Addison-Wesley, 1969.

[14] F. F. Chen Introduction to Plasma Physics and Controlled Fusion, Second edition, Volume 1, Plenum Press,New York and London, 1986.

[15] D. M. Cook, The theory of the electromagnetic field, Prentice-Hall, 1975.

[16] J. F. Drake, P. K. Kaw, Y. C. Lee, G. Schmidt, C. S. Liu, and M. N. Rosenbluth, Phys. Fluids, **17**, 778 (1974).

[17] V. V. Eliseev, W. Rozmus, V. T. Tikhonchuk, and C. E. Capjack, Phys. Plasmas, **2**, 1712 (1995).

[18] K. Estabrook, W. L. Kruer, and D. S. Bailey, Phys. Fluids, **28**, 19 (1985).

[19] D. W. Forslund, J. M. Kindel, and E. L. Lindman, Phys. Fluids, **18**, 1002 (1975).

[20] D. W. Forslund, J. M. Kindel, and E. L. Lindman, Phys. Fluids, **18**, 1017 (1975).

[21] D. W. Forslund, J. M. Kindel, and K. Lee, Phys. Fluids, **22**, 462 (1979).

[22] P. Frycz, W. Rozmus, J. Samson, V. T. Tikhonchuk, and R. Rankin, Comments Plasma Phys. Controlled Fusion, **15**, 19 (1992).

[23] A. A. Galeev, and R. Z. Sagdeev, Nuclear Fusion, **13**, 603 (1973).

[24] J. W. Goodman, Statistical Optics, John Wiley & Sons, 1985.

[25] D. Gottlieb, and S. A. Orszag, Numerical Analysis of Spectral Methods: Theory and Applications, SIAM-CBMS, Philadelphia, 1977.

[26] A. A. Galeev, and R. N. Sudan, Handbook of Plasma Physics, vol.2, North-Holland Physics Publishing, 1984.

[27] S. Hüller, Ph. Mounaix, and D. Pesme, Phys. Scr., **T63**, 151 (1996).

[28] J. C. Inkson Many-body Theory of Solids, Plenum Press, New York and London, 1983.

[29] J. D. Jackson, Classical Electrodynamics, John Wiley, 1962.

[30] B. B. Kadomtzev, Collective phenomena in plasma, Science, Moscow, 1976, *in Russian.*

[31] P. K. Kaw, G. Schmidt, and T. Wilcox, Phys. Fluids, **16**, 1522 (1973).

[32] G. A. Korn, and T. M. Korn, Mathematical Handbook, McGraw-Hill, 1968.

[33] N. A. Krall, and A. W. Trivelpiece, Principles of Plasma Physics, McGraw-Hill, 1973.

[34] W. L. Kruer, Comments Plasma Phys. Controlled Fusion, **9**, 63 (1985).

[35] W. L. Kruer, The Physics of Laser Plasma Interactions, Addison-Wesley, Ney York, 1988.

[36] R. L. Liboff, Kinetic Theory, Prentice-Hall, 1990.

[37] C. E. Max, Phys. Fluids, **19**, 74 (1976).

[38] D. R. Nicholson, Introduction to Plasma Theory, John Wiley & Sons, 1983.

[39] G. L. Payne, D. R. Nicholson, and R. M. Downie, J.Comput.Phys., **50**, 482 (1983).

[40] J. M. Sanz-Serna, and J. G. Verwer, IMA J.Num.Analysis., **6**, 25 (1986).

[41] V. P. Silin, and V. T. Tikhonchuk, Sov. Phys. JETP, **56**, 765 (1982).

[42] K. Rektorys, Variational Methods in Mathematics, Science and Engineering, Second edition, Reidel Publishing Company, Dordrecht, 1980.

[43] A. J. Schmitt, Phys. Fluids, **31**, 3079 (1988).

[44] A. Vanderlugh, Optical Signal Processing, John Wiley & Sons, 1992.

[45] P. E. Young, Phys. Plasmas, **7**, 2815 (1995).

Chapter 3

Instability of nonlinear filaments

As pointed out in the Introduction, Section 1, the nonlinear behavior of an electromagnetic wave interacting with an underdense laser produced plasma is an ongoing concern in inertial confinement fusion studies and in other applications of intense laser pulses including x-ray sources and laser particle accelerators. Different beam smoothing techniques have been designed to improve the uniformity of plasma illumination. All of them involve a random phase plate, which breaks the laser beam into many independent beamlets whose interference pattern in the laser focal spot creates an ensemble of statistically independent speckles. This improves the uniformity of the intensity pattern. However, within the speckle distribution there are always a significant number of hot spots with large intensities, many times above the average value. These very intense hot spots give rise to nonlinear effects which can alter the properties of laser beams at the macroscopic level. Thus, the importance of studying the physics of a single hot spot is magnified by the necessity of understanding the evolution of complex RPP beams.

This chapter explores the evolution of a single hot spot at very early times and provides an insight for understanding the physics of individual hot spots. The basic phenomenon that is considered here is self-trapping. Self-trapping occurs when the tendency of the beam to spread due to diffraction is compensated by

its tendency to contract due to SF. As a result, the beam maintains a constant small diameter over a distance much longer than the usual length of the focal region. The self-trapping process is similar to the propagation of a light wave through a dielectric wave guide. In this case the waveguide is created by the ponderomotive force of the light itself, which locally changes the refractive index. Such a waveguide, though, is usually unstable and small perturbations in the beam diameter can lead to either blow-up due to diffraction or collapse due to the SFI.

Considering the stability of laser light filaments in a homogeneous isothermal plasma with respect to coupled electromagnetic and density perturbations, we found that in addition to the known modulational instability of a guided electromagnetic mode there is a new fast growing resonant instability. It corresponds to the excitation of another waveguide electromagnetic mode strongly coupled to localized density perturbations.

If laser light power in a speckle is above the critical value for the self-focusing [20, 7], the speckle evolves into a filament by forming an elongated density channel with trapped light propagating along its axis. An equilibrium state of a nonlinear filament corresponds to a balance between light ponderomotive and plasma pressures. Equilibrium filaments have been extensively discussed in the stationary approximation described by the nonlinear Schrödinger (NLS) equation [5, 17, 23, 24].

The validity of the stationary approximation is limited by the filament modulational instability, which develops on a long ion-acoustic time scale and involves relatively long wavelength spatial perturbations [25, 21]. It involves a dynamical ion wave response and an absolute growth in time. However, recent three dimensional simulations [11] have shown an instability of a single nonlinear filament which results in its total destruction on a very short time scale. This fast res-

onant instability of a filament has profound ramifications for randomized laser beams. It might repeat itself many times if the laser beam duration is much longer than the filament formation time.

We explain filament destruction by a new kind of a parametric interaction in which a fundamental waveguide mode of trapped electromagnetic radiation is coupled to the next excited state in the waveguide. This coupling involves a supersonic density response and displays similarities to the strongly driven forward SBS. However, contrary to the forward SBS of plane waves or broad laser beams, the scattering in a filament is characterized by a narrow maximum in the growth rate as a function of the wave number. This well defined resonant wave number of the perturbation enables identification of the instability in simulations and allows an experimental verification.

The sensitivity of the resonance instability on the plasma channel depth also offers a possibility for its control with the laser beam temporal smoothing technique. The instability could be suppressed if the beam coherence time is less than the time of filament formation. This effect has also been observed in simulations and experiments. Finally, the filamentation instability also has a significant effect on the backscattering parametric instabilities by diminishing the size of interaction region and the effective pump wave intensity.

The content of this chapter is organized as follows. Section 3.1 presents a discussion of the stationary solutions as excited states in the framework of nonlinear Schrödinger (NLS) equation and reviews the solution by the method of an average Lagrangian. In Section 3.2, a stability analysis of an equilibrium filament is performed on the basis of of the eigenmode equations. The results of the numerical simulation are presented in Section 3.3 demonstrating the filament time evolution.

3.1 Basic equations and stationary solutions

The linearly polarized electromagnetic wave field, $\mathcal{E}$ is enveloped in space and time,

$$\mathcal{E}_y = \frac{1}{2}\left\{E e^{i(k_0 z - \omega_0 t)} + c.c.\right\},$$

where ω_0 is the laser frequency and

$$k_0 = (\omega_0/c)\sqrt{1 - n_0/n_c}, \tag{3.1}$$

is the light wave-vector in plasma.

To describe the dynamical evolution of the electron density perturbation, δn, and the electric field amplitude, E, we use the paraxial approximation of the full system of the model equations Eq. (2.88) and Eq. (2.91)

$$\begin{aligned}\left(i\frac{\partial}{\partial z} - \frac{i}{v_g}\frac{\partial}{\partial t} + \nabla_\perp^2\right) E &= \delta n E, \\ \left(\frac{\partial^2}{\partial t^2} - \nabla_\perp^2\right)\ln(1+\delta n) &= \nabla_\perp^2 |E|^2,\end{aligned} \tag{3.2}$$

where

$$v_g = k_0 c/\omega_0 \tag{3.3}$$

is the electromagnetic wave group velocity, and the total electron density reads

$$n_e = n_0(1 + \delta n).$$

The different structure of the system of PDEs, Eq. (3.2), calls for a different normalization, as compared to Eq. (2.93), namely

$$\begin{aligned} t &= \frac{c_s \omega_{pe}}{c} t', \\ r &= \frac{\omega_{pe}}{c} r', \\ z &= \frac{\omega_{pe}^2}{2k_0 c^2} z', \\ E &= \frac{E'}{\sqrt{16\pi n_c T_e}}, \end{aligned}$$

where the radial coordinate, $r = \sqrt{x^2 + y^2}$ has been introduced.

The logarithmic term in the acoustic equation accounts for the saturation of a density response, which is necessary for the formation of equilibrium filaments.

Setting $E = E_s \exp(i\lambda z)$ and assuming steady state, Eq. (3.2) are reduced to the NLS equation

$$\left(i\frac{\partial}{\partial z} + \epsilon_p \frac{\partial^2}{\partial z^2} + \nabla_\perp^2\right) E_s = n_s(|E_s|^2)E_s, \tag{3.4}$$

where the quantity $\epsilon_p = n_e/4(n_c - n_e)$ is zero in the paraxial limit approximation. Here the equilibrium density perturbation

$$n_s = -1 + \exp(-|E_s|^2),$$

is of the *saturable nonlinearity* type, and describes the slow ponderomotive SF of laser beams in plasmas [13, 12, 8, 16]. The substitution, $n_s = -|E_s|^2$, yields the non-saturated nonlinearity corresponding to the usual Kerr effect.

Eq. (3.4) is one of the basic evolutionary models in physics, describing the slowly varying envelope of a wave-train in conservative dispersive systems [see as ex. Ref.[15]]. It involves the competing effects of diffraction and nonlinearity. When $n_s(|E_s|^2) > 0$, the effect of nonlinearity is dominant and the beam undergoes self-focusing [2] or filamentation [6] (for the beam power exceeding several times some critical value, P_{cr}). When the nonlinearity and diffraction balance each other, the Eq. (3.4) has steady state soliton solutions, describing beam self-trapping [4].

Eq. (3.4) has two well known integrals of motion. One, proportional to the beam power

$$P[E_s] = \int r dr |E_s|^2, \tag{3.5}$$

and the Hamiltonian

$$H[E_s] = \int r dr \left(|\nabla_\perp E_s|^2 - F(|E_s|^2)\right), \tag{3.6}$$

where

$$F(|E_s|^2) = \int_0^{|E_s|^2} n_s(x)dx. \tag{3.7}$$

Eq. (3.4) can be solved either numerically [7] or analytically by using the variational approach [2, 3, 1, 9]. By using the variational approach one can derive the conditions for light trapping and the properties of the equilibrium filaments. It reformulates the initial system PDE's in terms of action integral, $S = \int dx L$, that is stationary with respect to independent, first order variation of the dependent variables. The Lagrangian density, corresponding to Eq. (3.4) is given by

$$L = i\left(E_s^* \frac{\partial E_s}{\partial z} - E_s \frac{\partial E_s^*}{\partial z}\right) - \left|\frac{\partial E_s}{\partial r}\right|^2 + |E_s|^2 - 1 + \exp(-|E_s|^2). \tag{3.8}$$

The approximate solution is obtained by a Ritz optimization procedure. It is based on the assumption that the profile of the initial Gaussian pulse

$$E(0,r) = E_0 \exp(-r^2/2a_0^2), \tag{3.9}$$

is preserved for $z > 0$ and can be described as

$$E(z,r) = E_0(z)e^{i\phi(z)} \exp\left(-\frac{r^2}{2a^2(z)} + ib(z)r^2\right) \tag{3.10}$$

where the amplitude $E_0(z)$, and the pulse width $a(z)$, the frequency chirp $2b(z)r^2$ and the phase $\phi(z)$ are unknown functions. By inserting the trial functions, Eq. (3.10), into the Lagrangian, Eq. (3.8), one obtains the reduced variational problem

$$\delta \int < L > dz = 0, \tag{3.11}$$

where

$$< L >= \int_\infty^\infty L_G dr, \tag{3.12}$$

for the new Lagrangian L_G. The result is a set of coupled ODE's for the Gaussian parameters E, a, b, and ϕ that determine the pulse evolution. The system can

be reduced to a single equation [11]

$$\frac{1}{2}\left(\frac{da}{dz}\right)^2 + V(a) = \frac{4}{P}H(a_0, b_0), \tag{3.13}$$

describing the evolution of a filament of radius a, with initial radius a_0 and initial chirp b_0, along the direction of propagation z. The potential $V(a)$ is given by

$$V(a) = 2/a^2 - 4\mu(a)/P, \tag{3.14}$$

where the first term, $2/a^2$, accounts for the linear diffraction effects, while the second term is related to the nonlinearrity.

The condition for light trapping are found to be

$$P > P_{cr}, \quad H_0 > (P/4)V(a_{eq}), \tag{3.15}$$

where the equilibrium radius a_{eq} is the value at which the potential $V(a)$ has a maximum value. In the average Lagrangian approximation the critical power for light trapping is $P_{cr} = 4$, while the exact value is $P_{cr} = 3.72$.

Computing the equilibrium radius, a_{eq}, one finds

$$a_{eq}^2 \approx \begin{cases} 16/9(P/P_{cr} - 1), & if \quad P/P_{cr} \to 1 \\ 2^{3/2}P/P_{cr}^{1/2}/(\ln(P/P_{cr}) + 0.54)^{1/2}, & if \quad P/P_{cr} \gg 1. \end{cases}$$

Figure (3.1) shows that the beam waist a_{eq} is a nonmonotonic function of P/P_{cr} with a minimum, $a_{eq} \approx 2$, reached for $P/P_{cr} \approx 2$.

In the case of saturated ion response, there exists a particular class of steady state solutions of Eq. (3.4), called equilibrium solutions, which take the form of elongated cylindrical filaments. The equilibrium solutions can be found by solving the eigenvalue problem for the NLS equation

$$\hat{L}E_{eq} = \lambda E_{eq}, \tag{3.16}$$

where

$$\hat{L} = \nabla_\perp^2 - n_{eq}(|E_{eq}|^2).$$

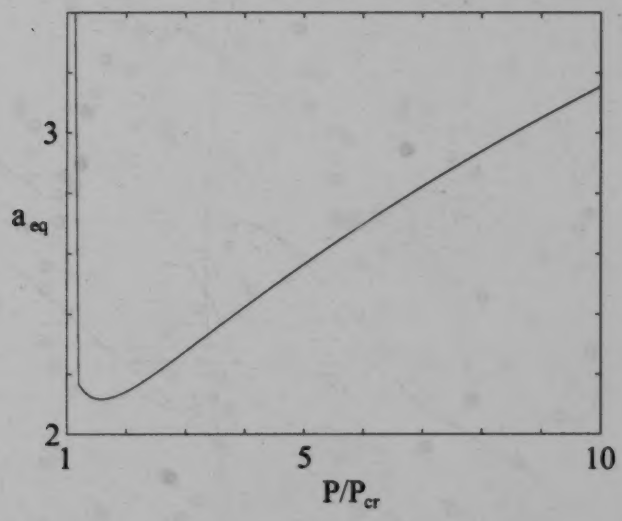

Figure 3.1: Dependence of beam waist a_{eq} from the P/P_{cr}.

Localized, axially symmetric solutions exist for $0 < \lambda < 1$. The limit $\lambda \to 0$ corresponds to the self-focusing threshold where the trapped power,

$$P = 2 \int r dr |E_{eq}|^2, \tag{3.17}$$

equals the critical power $P_c = 3.72$ [20, 7, 5, 23, 24]. The general expression for λ is given by

$$\lambda = \begin{cases} 1/a_{eq}^2, & if \quad P/P_{cr} \to 1 \\ 1, & if \quad P/P_{cr} \gg 1. \end{cases}$$

The dependence of eigenvalue λ on P/P_{cr} is presented in (3.2) and shows a monotonic variation.

3.2 Stability analysis of an equilibrium filament

The density perturbation, n_{eq}, represents a potential well for the electromagnetic wave, and $-\lambda$ defines the ground state energy level. One can also find higher excited states for a sufficiently deep potential well. These excited states, when present, lead to a fast growing instability of the ground state.

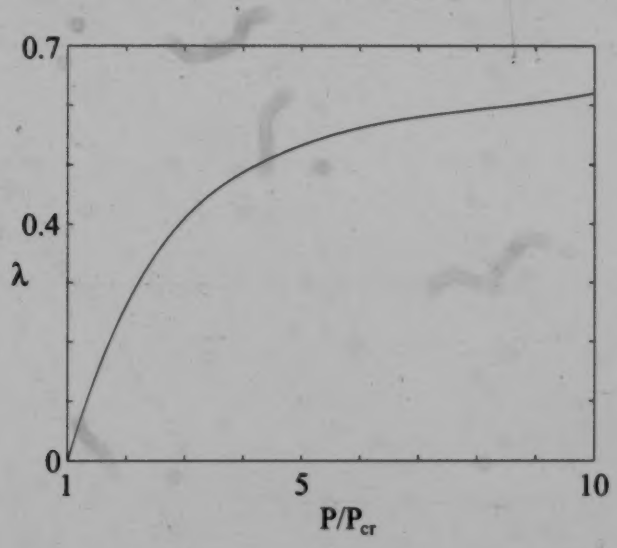

Figure 3.2: Dependence of eigenvalue λ on P/P_{cr}.

Considering solutions to Eq. (3.2), linearized with respect to the perturbations of an equilibrium state:

$$\begin{aligned} E &= (E_{eq} + \delta E)\exp(i\lambda z)\,, \\ n &= -1 + (1+\delta N)\exp(-|E_{eq}|^2), \end{aligned}$$

one obtains the following set of linear equations for three real functions: δN, $\delta E_R = \mathrm{Re}(\delta E)$ and $\delta E_I = \mathrm{Im}(\delta E)$:

$$\begin{aligned} \left(\hat{L}-\lambda\right)\delta E_R - \left(\frac{\partial}{\partial x} - \frac{1}{v_g}\frac{\partial}{\partial t}\right)\delta E_I &= (1+n_{eq})E_{eq}\delta N\,, \\ \left(\hat{L}-\lambda\right)\delta E_I + \left(\frac{\partial}{\partial x} - \frac{1}{v_g}\frac{\partial}{\partial t}\right)\delta E_R &= 0\,, \\ \left(\frac{\partial^2}{\partial t^2} - \nabla_\perp^2\right)\delta N &= 2\nabla_\perp^2 E_{eq}\delta E_R\,. \end{aligned} \tag{3.18}$$

Introducing cylindrical coordinates and an explicit dependence on the parallel coordinate, x, on the azimuthal angle ϕ, and on time,

$$\delta N = \mathrm{Re}(N)\exp(im\phi + \Gamma t - iqx)\,,$$

$$\delta E_R = \mathrm{Re}(E_R)\exp(im\phi + \Gamma t - iqx),$$
$$\delta E_I = \mathrm{Im}(E_I)\exp(im\phi + \Gamma t - iqx),$$

we find three eigenmode equations for $E_R(r)$, $E_I(r)$, and $N(r)$:

$$\begin{aligned}
(\hat{L}_m - \lambda)E_R - \left(q - i\frac{\Gamma}{v_g}\right)E_I &= (1+n_{eq})E_{eq}N, \\
(\hat{L}_m - \lambda)E_I - \left(q - i\frac{\Gamma}{v_g}\right)E_R &= 0, \\
\left(\Gamma^2 - \frac{1}{r}\frac{\partial}{\partial r}r\frac{\partial}{\partial r} + \frac{m^2}{r^2}\right)N &= \frac{2}{r}\left(\frac{\partial}{\partial r}r\frac{\partial}{\partial r} - \frac{m^2}{r}\right)E_{eq}E_R,
\end{aligned} \tag{3.19}$$

where

$$\hat{L}_m = (1/r)\frac{\partial}{\partial r}r\frac{\partial}{\partial r} - m^2/r^2 - n_{eq}.$$

It has been found before [25, 21, 11] that the system Eq. (3.19) is unstable with respect to the modulational instability in the long wavelength limit, $q \ll \lambda$. According to the analysis of Ref. [11], one obtains the following dispersion relation for the mode $m = 1$

$$\Gamma^2 = A^2q^2,$$

where

$$A^2 = \left(\int_0^\infty dr E_{eq}^2[1 - \exp(-E_{eq}^2)]\right)^{-1}\int_0^\infty rdr E_{eq}^2.$$

In the limit of a small amplitude filament, $\lambda \ll 1$, one finds, $A \approx 1/\sqrt{2\lambda}$. This leads to the estimate of a maximum growth rate $\Gamma_{max} \sim \sqrt{\lambda}$ at $q \leftarrow \lambda$. This instability develops on a relatively long time scale which gives filaments an opportunity to affect laser plasma interaction processes.

A much faster growing supersonic instability can be found in the short wavelength domain, $q \leftarrow k_{eq}$, if there is another guided electromagnetic mode in the equilibrium density channel, n_{eq}. To describe this solution analytically we have to further simplify the model equations. It follows from the third equation of Eq. (3.19) that the density perturbation is small in the limit of a large growth,

$|\Gamma| \gg 1$. Neglecting N in the first equation of Eq. (3.19), we obtain a system of two equations for the electromagnetic wave amplitudes in the first-order approximation;

$$\begin{aligned} (\hat{L}_m - \lambda)E_R^{(1)} - q_{res}E_I^{(1)} &= 0, \\ (\hat{L}_m - \lambda)E_I^{(1)} - q_{res}E_R^{(1)} &= 0. \end{aligned} \tag{3.20}$$

These are eigenvalue equations for the resonance wave number q_{res}, which corresponds to an excited level in the filament with a given density profile. Localized solutions require $0 < q_{res} < \lambda$ since λ corresponds to a ground level. The eigenvalue analysis of Eqs. Eq. (3.20) for $m = 1$ shows that there is no eigenstates other than the fundamental mode, if $\lambda < 0.41$ (i.e. $P \approx 3P_c$), and there is an eigenstate $\lambda_1 = \lambda - q_{res}$ for filaments with larger intensity. By comparison, there is no threshold value for the antisymmetric mode in two-dimensional case often considered in simulations. The dependence of an eigenvalue λ_1 on P/P_c is shown in Fig. 3.3(a).

The eigenmode $E_R^{(1)}(r)$ for $\lambda = 0.5$ ($P/P_c = 4.24$) is shown in Fig. 3.3(b). Higher excited levels appear in much more intense filaments. Levels with $m = 0$ (the mode with one node) and $m = 2$ exist for $\lambda \to 0.75$ ($P/P_c \to 18.7$), next level $m = 1$ appear for $\lambda \to 0.8$ ($P/P_c \to 30.2$) and so on. We limit the discussion here to the lowest excited level.

At the second-order approximation the density perturbation follows from the third equation of Eq. (3.19):

$$N^{(2)} = \frac{2}{r\Gamma^2}\left(\frac{\partial}{\partial r}r\frac{\partial}{\partial r} - \frac{1}{r}\right)E_{eq}E_R^{(1)},$$

and one obtains a second-order equation for the electric field assuming a small deviation $\Delta q = q - q_{res}$ from resonance:

$$\begin{aligned} &(\hat{L}_1 - \lambda + q_{res})\,(E_R^{(2)} - E_I^{(2)}) = \\ &\quad -2\left(\Delta q + i\frac{\Gamma}{v_g}\right)E_R^{(1)} + \frac{2}{r\Gamma^2}(1 + n_{eq})E_{eq}\left(\frac{\partial}{\partial r}r\frac{\partial}{\partial r} - \frac{1}{r}\right)E_{eq}E_R^{(1)}. \end{aligned}$$

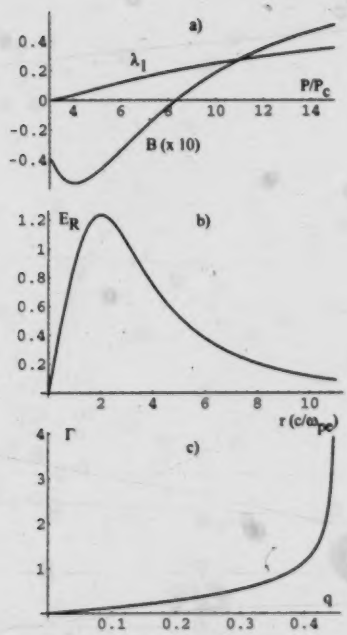

Figure 3.3: a) Dependence of the excited level λ_1 in the filament and the coupling coefficient B (magnified 10 times) for the resonance instability on the filament power, P/P_c. b) Radial profile of the eigenfunction of the excited state $m = 1$ for $P/P_c = 4.24$.

Since $\hat{L}_1$ is a self-adjoint operator, the dispersion equation can be obtained by multiplication of the above equation by the first-order eigenfunction followed by integration over the radial coordinate. It can be written as

$$\Gamma^2(\Delta q + i\Gamma/v_g) = B,$$

where

$$B = \left(\int_0^\infty r dr [E_R^{(1)}]^2\right)^{-1} \int_0^\infty r dr (1+n_{eq}) \left[\frac{1}{2}\frac{\partial}{\partial r}E_{eq}^2 \frac{\partial}{\partial r}[E_R^{(1)}]^2 + (2\lambda - q_{res} + 2n_{eq})E_{eq}^2[E_R^{(1)}]^2\right].$$

The dependence of the parameter B on P/P_c is shown in Fig. 3.3(a). It assumes relatively small values, $|B| \sim 0.1$, and it also changes sign from negative to positive for $P/P_c \approx 9$ ($\lambda \approx 0.64$).

The maximum growth rate of the resonance instability,

$$\Gamma_{max} = \frac{\sqrt{3} - iB/|B|}{2}(|B|v_g)^{1/3}, \tag{3.21}$$

corresponds to the resonant perturbation, $\Delta q = 0$. The width of the resonance, $\Delta q_{res} \sim (|B|/v_g^2)^{1/3}$, is rather narrow.

The system Eq. (3.19) can be solved numerically or by polynomial expansion [14]. The calculated growth rate is in agreement with the analysis presented above. The instability disappears after the resonance, $q > q_{res}$.

This instability is similar to the hose-modulation instability considered for short laser pulses [18, 19] where only the fast electron response has been accounted for. A more detailed analysis of short laser pulse instabilities which includes modes $m = 0, 1,$ and 2 has been done recently by Duda and Mori [10]. It is also instructive to compare the maximum growth rate of the resonance instability with the growth rate for SBS. The growth rate Eq. (3.21) can be written as

$$\Gamma \approx |B|^{1/3}\omega_0^{1/3}(\omega_{pe}c_s/c)^{2/3}.$$

It is comparable to the growth rate that one could expect for the backward SBS in the limit of strong coupling and it is much larger than the maximum forward SBS growth rate for a homogeneous pump wave. The difference is in the factor $k_\perp/k_0 < 1$ where $k_\perp$ is the wave number of ion acoustic wave which participates in the forward SBS. The explanation of such a difference is that the filaments which are subjected to the resonance instability already have a relatively small radius, $a_0 \sim 2c/\omega_{pe}$ and therefore introduce a relatively small scale density perturbation.

3.3 Numerical simulations of the filament instability

We performed numerical simulations which demonstrated the instability of laser filaments and, in addition, indicated that the instability leads to the filament disintegration. The results were confirmed with similar simulations conducted using a 3D quasi-paraxial code F3D [6] *. We only discuss the results obtained from our 2D non-paraxial code. The three-dimensional results are similar to our simulations.

The simulations start with the Gaussian laser beam being focussed in the plasma and show formation of nonlinear filaments which are very similar to the equilibrium NLS solutions described before.

Figure (3.4) demonstrates contours of light intensity in the interaction region at three different time moments illustrating filament formation, Fig. (3.4)(a) and Fig. (3.4)(b), and the subsequent destruction, Fig. (3.4)(c). To the right of the contour plots far field images are shown for the same time moments which are angular distributions of the transmitted light. During the phase of filament for-

*In both codes the backward SBS is controlled by either strongly damping an ion-acoustic wave which is responsible for the backward scattering or not solving the equation for the back-propagating wave (in the paraxial code).

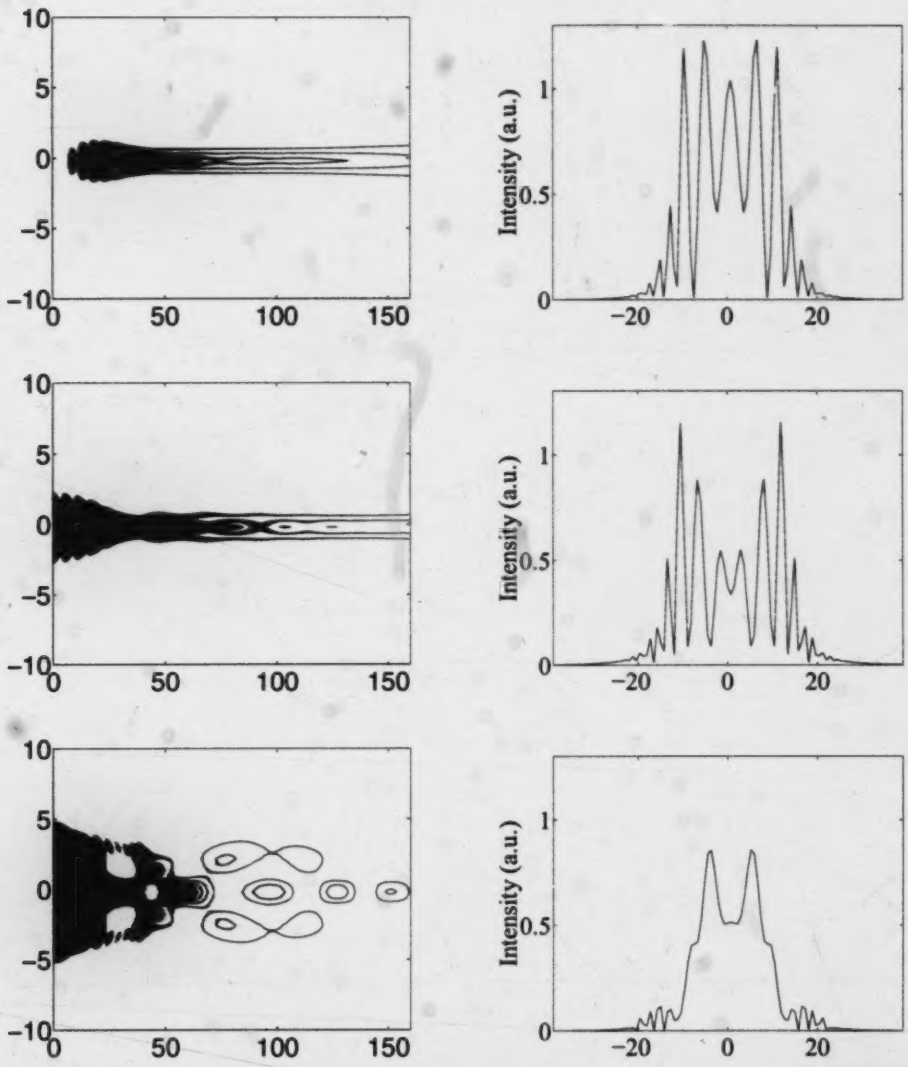

Figure 3.4: Intensity contours and angular distributions of transmitted light at different times: (a) 14.5 ps, (b) 18.2 ps, (c) 21.8 ps. At time t=0 ps the 1 μm Gaussian beam has been focussed in the center of the simulation box $100 \times 160\,\mu\text{m}^2$ with maximum intensity 1.46×10^{15} W/cm^2 and FWHM 6 μm. The background plasma parameters are: $n_0/n_c = 0.4$ and $T_e = 1$ keV.

mation they display an interference pattern of the coherent light emitted from the narrow orifice which is created by the plasma density channel. The coherent pattern disappears, Fig. (3.4)(c), after rapid growth of the instability and filament disintegration. This illustrates a plasma induced smoothing effect in the laser beam.

The instability appears at a time of $18-19$ ps and it is characterized by a fast growth rate, comparable with the theoretically found value of $\Gamma_{max} = 1.2$ ps^{-1}. A modulation period of about $20-22$ μm in Fig. (3.4)(b) and Fig. (3.4)(c) in the propagation direction is also in agreement with results of the linear theory, Eq. (3.21), giving $2\pi/q_{res} \approx 20\,\mu$m. Intensity maxima and their location ($\sim 2\,\mu$m away from the laser axis in Fig. (3.4)(c)), correspond to the resonantly excited antisymmetric mode shown in Fig. (3.3)(b).

Numerical simulations show that the instability is effectively destroying the filament. When energy is transferred from the fundamental to the excited mode, it exerts a ponderomotive pressure which does not support the original density channel due to the complicated intensity pattern that is generated, Fig. (3.4)(c). Because of this instability, the light is detrapped and propagates over a wide interaction region.

Nonlinear filaments are formed over a relatively long time period, equal to the acoustic propagation time across the initial laser beam, which corresponds to a simulation time of 18 ps. Although the resonant instability develops during much shorter time period it does not prevent filament formation. The solution of the eigenmode equation Eq. (3.19) indicates that the resonant instability is suppressed if the density channel depth is not sufficient to support the excited eigenmode. The necessary depth must be of the order of 90% of the density perturbation observed in the equilibrium filaments. This explains both the relatively long time for filament formation and its fast disruption.

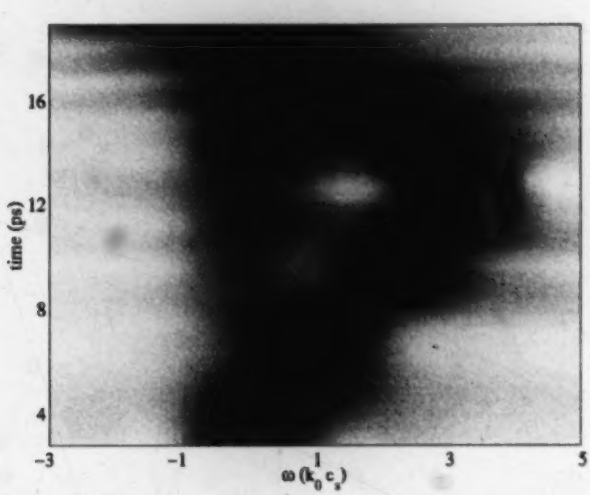

Figure 3.5: Frequency spectrum of the transmitted light, which has been calculated within the window of 6 ps at different moments of time. Frequency is given in units of $k_0 c_s = 1$ ps^{-1} which corresponds to the wavelength shift of 0.57 nm.

The dynamical evolution of a single filament results in a red shift of the transmitted light spectrum as shown in Fig. (3.5). An increasingly red shifted component corresponds to time dependent phase shift, $\Phi = \int k_z dz$, of an electromagnetic wave propagating in a deepening density channel. This frequency shift,

$$\delta\omega = -\frac{\partial \Phi}{\partial t} \approx \frac{k_0 L}{2n_c}\frac{\partial n}{\partial t}$$

characterizes the filament formation phase and continues until the time of 18 ps, when the instability takes over. The values of the red shift are large, $\sim 1.5 - 2$ nm, many times above the magnitude which forward SBS could produce within the directions of propagation shown in Fig. 3.4. The density perturbations remaining after filament destruction propagate in the plasma further enhancing angular spread of the transmitted light (Fig. 3.4c) and forward SBS (late time spectrum in Fig. (3.5)).

Bibliography

[1] D. Anderson, Phys. Rev. A **27**, 3135 (1983).

[2] D. Anderson, and M. Bonnedal, Phys. Fluids **22**, 105 (1979).

[3] D. Anderson, M. Bonnedal, and M. Lisak, Phys. Fluids **22**, 788 (1979).

[4] D. Anderson, M. Bonnedal, and M. Lisak, Phys. Fluids **22**, 1838 (1979).

[5] L. Bergé, Phys. Reports **303**, 259 (1998).

[6] R. L. Berger, B. F. Lasinski, T. B. Kaiser, E. A. Williams, A. B. Langdon, and B. I. Cohen, Phys. Fluids B **5**, 2243 (1993).

[7] R. Y. Chiao, E. Garmire, and C. H. Townes, Phys. Rev. Lett. **13**, 479 (1964).

[8] B. I. Cohen, B. F. Lasinski, A. B. Langdon, and J. C. Cummings, Phys. Fluids B **3**, 766 (1991).

[9] M. Desaix, D. Anderson, and M. Lisak, J. Opt. Sox. Am. **8**, 2082 (1991).

[10] B. J. Duda, and W. B. Mori, Phys. Rev. E **61**, 1925 (2000).

[11] V. V. Eliseev, D. Pesme, W. Rozmus, V. T. Tikhonchuk, and C. E. Capjack, Phys. Scripta **T75**, 112 (1998).

[12] P. Kaw, G. Schmidt, and T. Wilcox, Phys. Fluids **16**, 1522 (1973).

[13] C. E. Max, Phys. Fluids **19**, 74 (1976).

[14] D. Pesme, W. Rozmus, V. T. Tikhonchuk, A. Maximov, I. Ourdev, and C. H. Still, Phys. Rev. Lett. **84**, 278 (2000).

[15] J. J. Rasmussen, and K. Rypdal, Phys. Scripta **33**, 481 (1986).

[16] H. A. Rose and D. F. DuBois, Phys. Fluids B **6**, 3337 (1993).

[17] H. A. Rose and D. F. DuBois, Phys. Plasmas **2**, 2216 (1995).

[18] G. Shvets and J. S. Wurtele, Phys. Rev. Lett. **73**, 3540 (1994),

[19] Ph. Sprangle, J. Krall, and E. Esarey, Phys. Rev. Lett. **73**, 3554 (1994),

[20] V. I. Talanov, Izv. VUZov, Radiofizika **7**, 564 (1964).

[21] E. Valeo, Phys. Fluids **17**, 1391 (1974).

[22] E. Valeo, and K. G. Estabrook, Phys. Rev. Lett. **34**, 1008 (1975).

[23] F. Vidal, and T. W. Johnston, Phys. Rev. Lett. **77**, 1282 (1996).

[24] F. Vidal, and T. W. Johnston, Phys. Rev. Lett. **77**, 4852 (1996).

[25] V. E. Zakharov and A. M. Rubenchik, Sov. Phys. JETP **38**, 494 (1974).

Chapter 4

Interactions in a single hot spot

In this Chapter we discuss theoretical and numerical results related to a series of experiments [21, 20, 18] that examine different aspects of laser pulse propagation through an exploding foil plasma.

Investigations of ignition-scale ICF gas targets [12] address an integrated set of problems, related to the effects of beam smoothing on SBS and filamentation, beam pointing and deflection, effects of ion composition on SBS reflectivity, etc. Smaller scale experiments, which have investigated the ion wave response to intense laser pulses have been performed with exploding foil targets. They differ from ICF relevant measurements by a much lower temperature, a smaller plasma size and stronger inhomogeneities. However they provide a more accurate diagnostics and have been able to isolate important physical processes. Most recent examples of such experiments are observations of backward SBS induced by spatially and temporally incoherent laser light [9, 3], detailed Thomson scattering measurements of SBS produced ion waves [9, 18], and the demonstration of channel formation and physics of laser pulse propagation [19] motivated by the ICF ignitor concept [15]. A better theoretical understanding of these experiments helps in extrapolating the present results to the scales and sizes relevant to ICF reactor plasmas.

In the first interpretation of these experiments [17], spreading of a transmit-

ted laser beam has been attributed to light scattering on density fluctuations produced by filamentation. The maximum angular spread of laser light outside the focussing optics in the forward direction has been linked to the wave number of density perturbations corresponding to the maximum growth of ponderomotive filamentation. The initial theoretical interpretation presented in Refs.[19, 17] did not consider SBS in backward and forward directions in spite of the averaged 15% SBS reflectivity measured in the backward direction within the focussing optics.

It is essential that modeling of these experiments include a realistic distribution of the laser beam intensity and interaction between SBS, filamentation and self-focussing instabilities. The latter has been achieved in a non-paraxial description of electromagnetic wave propagation through the underdense plasma [1, 4, 6, 5]. By solving the full electromagnetic wave equation, we can properly describe the simultaneous SBS and FI as well as small scale hot spots approaching transverse dimensions on the order of laser wavelengths during the non-linear evolution of the FI. As we show, it is also very important not to restrict *a priori* possible directions of SBS light by identifying the dominant direction of laser light propagation.

Using the numerical model given by Eq. (2.88) and Eq. (2.91) to describe the experimental situation, we can summarize the important results obtained as follows. First of all, a weak correlation between backscattered SBS and filamentation and self-focussing instability was established. Comparison between transmitted and backscattered light, shows that filamentation and density modulations affecting transmitted light are spatially separated from the region of backward SBS growth. In effect, both instabilities develop almost independently, which contradicts the conventional point of view that filamentation significantly enhance the backward SBS. The transmitted light demonstrates angular spread-

ing and frequency shifts consistent with near-forward SBS.

In addition, we found that the self-focussing of the narrow parts of Gaussian beams seeds the transversely propagating sound waves and increases the filamentation. The filamentation instability then competes with the near-forward SBS. The results show that FI can be very effective during the initial time evolution. However on the time scale defined by an experimental pulse duration ($\sim 100ps$) near-forward SBS dominates and controls the characteristic properties of the transmitted light. These results were confirmed by analytical considerations, presented later in Section 4.8.

In the next Section 4.1 we describe our approach of achieving a realistic model of the laser pump by adding two Gaussian beams with properly chosen parameters.

Section 4.2 specifies a set of parameters used for the numerical simulations.

In Section 4.3 we describe the early time (up to $\sim 10ps$) evolution of the hot spot and quantify its formation.

Section 4.4 concentrates on the FI of a wider laser beam as reflected in the transmitted and backscattered light and demonstrates the spatial separation from the region of backward SBS growth. This separation is further investigated in the next Section 4.5 by using the frequency spectra of the transmitted light at later times ($\sim 30, 50ps$).

Section 4.6 describes the late time ($\sim 100ps$) evolution of the laser beam and the development of RPP-like small-scale hot spots.

Finally, Section 4.7 contains an explanation of the experimental observations of the reflected and transmitted energy as a function of plasma density.

4.1 Laser pump model

The main objective here was to achieve a better understanding of the physical processes involved in the experiment by Young *et al.* [19, 17]. The experimental data includes a well-characterized laser intensity distribution in the best focal position and across the interaction region. We have approximated the main characteristics of the experimental laser beam spatial profiles in our simulations. This feature plays an important role in the dynamic evolution of the interaction process. We have modeled an incident laser beam at the initial moment as a sum of two Gaussian beams with different f-number and intensities, but having the same focal positions. The field distribution in the best focus position, has the following form:

$$E(y)|_{x=x_f,t=0} = \sum_{m=1}^{2} E_{0m} \exp\left(-\frac{(y-y_f)^2}{2f_m^2\lambda_0^2}\right) \tag{4.1}$$

The maximum amplitudes of the pump electric fields are $E_{01} = 0.47E_0$ and $E_{02} = 0.53E_0$, where the amplitude E_0 defines the maximum pump intensity $I_0 = |E_0|^2$.

Experiments have been conducted for two typical cases, one where the laser beam has been focussed to a circular focus, the other a line focus [19]. Correspondingly, we have performed two sets of simulations.

Figure (4.1)(a) shows intensity cross section of the laser field in the best focus position for a circular focus, and for a line focus, Fig. (4.2)(a). The circles correspond to the experimental data, while solid lines refer to our model for $I_0 = 1.7 \times 10^{15} W/cm^2$. Although a real laser beam has a more complicated phase structure, this model, Eq. (4.1) is sufficient for the analysis of parametric instabilities because the length of the interaction region is comparable to the beam Rayleigh length

$$L_R = 2\pi f_1^2 \lambda_0 \sqrt{1 - n_e/n_c}. \tag{4.2}$$

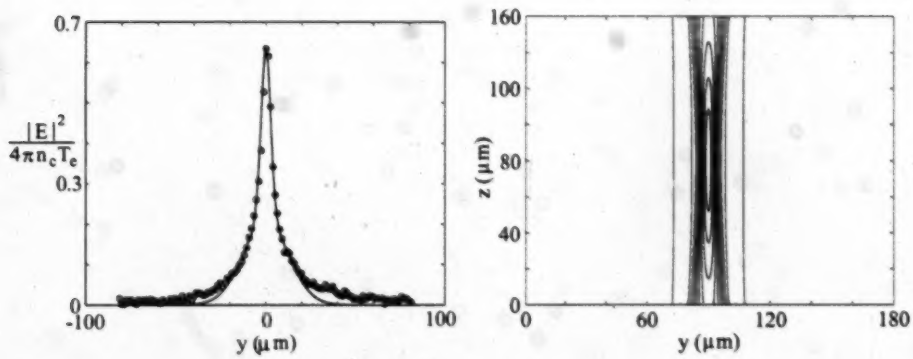

Figure 4.1: Circular focus, a) intensity cross section at best focus position at the initial moment in time and b) intensity contour plot at the initial moment in time. The figure on the left shows a comparison between the experimental measurements (small circles) and the theoretical distribution (solid line) used in simulations.

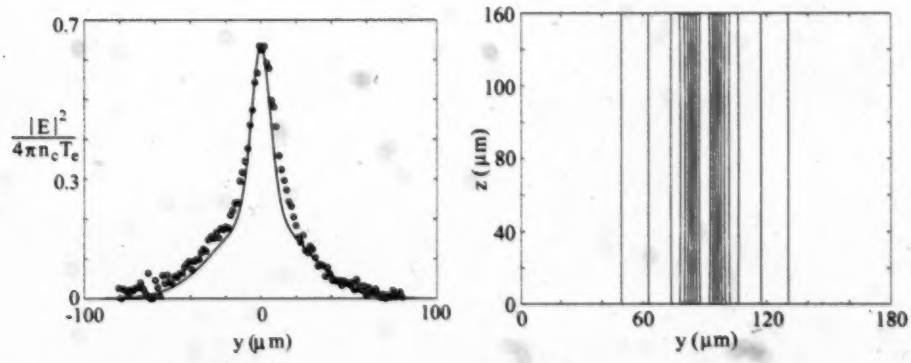

Figure 4.2: Line focus, a) intensity cross section at best focus position at the initial moment in time. Shows a comparison between the experimental measurements (small circles) and the theoretical distribution (solid line) used in simulations.

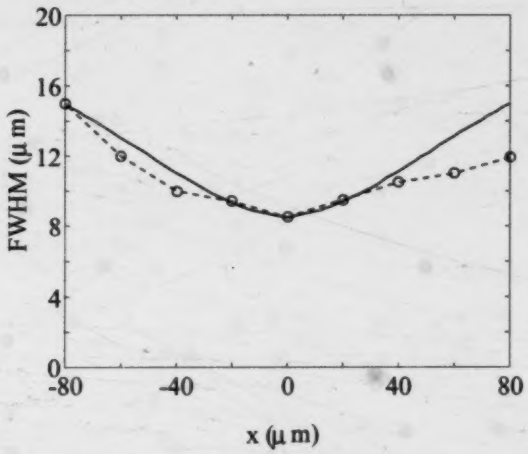

Figure 4.3: Circular focus – a comparison between the measured FWHM spot diameter as a function of the axial position (circles and dashed line) and the theoretical calculations (solid line) based on Eq. (4.1).

Figures (4.1)(b) and (4.2)(b) display the laser intensity distributions in the interaction region at the initial time for circular and line focusses, respectively. One can clearly see the small f-number beam contributing to a narrow intensity enhancement at the best focus position for the circular focus. A similar enhancement is more elongated in the propagation direction for the line focus. As we demonstrate later, this feature is important for the dynamics of self-focussing and filamentation instabilities.

To reproduce with an even better accuracy the experimental conditions we have matched the laser intensity distribution for the circular focus with the available experimental FWHM (full width half maximum) as a function of the axial distance. Figure (4.3) shows this comparison within the interaction length, where the dashed line is plotted using Eq. (4.1).

As we pointed out in Subsection 2.4.1, SBS is a convective instability and therefore should be supported at all times by a noise source and/or electromagnetic seed. The results described here are obtained with a seed provided by a

small amplitude electromagnetic wave with the frequency shifted to satisfy the backward SBS resonance condition for a wave propagating in a direction opposite to the pump beam. The intensity of the seed electromagnetic wave is a small fraction ($\epsilon \sim 10^{-6}$) of the maximum intensity of the pump beam. It is supported by density modulations produced by the ponderomotive force of an inhomogeneous incident laser beam.

4.2 Simulation plasma parameters

Guided by experimental conditions [19, 17], the following plasma parameters have been chosen for the simulations. The density gradient measured in experiments had a typical scale length of $300\mu m$. The size of the plasma in our simulations ($160\mu m \times 180\mu m$) was smaller than the characteristic inhomogeneity length in the experiment, therefore the assumption of a homogeneous plasma density (Section 2.2) is well justified. An additional approximation, of a zero initial plasma velocity, has been made in order to simplify instability modeling. It is clear, that for a complete understanding of the interaction processes, particularly backward SBS [22], the effects of inhomogeneous plasma flow have to be included, but the emphasis in this analysis is on processes which directly affect transmitted light, e.g. near-forward SBS, filamentation or self-focussing which are less sensitive to the plasma inhomogeneity.

We control the backward SBS by introducing relatively strong damping of ion acoustic wave at the wave number k_s and frequency ω_s. These are waves resonantly driven by the backward SBS and in the simulations are assumed to have a damping rate $\gamma_s/\omega_s = 0.3$. A laser beam has been focussed in the middle of the box ($x_f = 80\mu m$) and the temperature of the electrons was taken to be $T_e = 1keV$. We have varied the plasma density over the range n_e/n_c from 0.05 to 0.3 and have used different values for the pump intensity. The simulation time

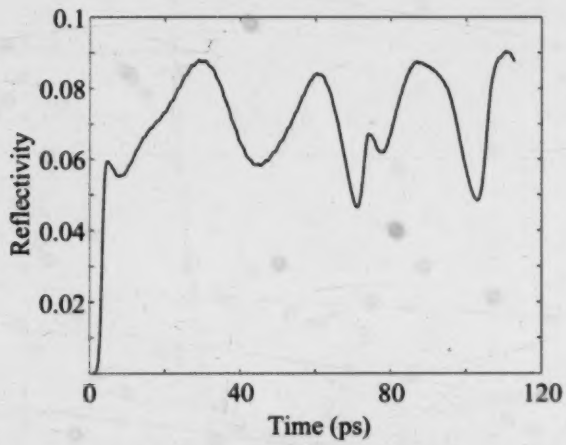

Figure 4.4: Circular focus – typical time dependence of backward SBS reflectivity. The parameters of the run are $I_0 = 1.7 \times 10^{15} W/cm^2, n_e/n_c = 0.1$.

corresponds to laser pulse duration of approximately 100 ps.

4.3 Early time behavior

During the numerical calculations we monitored the plasma density fluctuations δn_e and intensity distribution $|E|^2$ inside the plasma, which we define as *near field*. The angular distribution of the transmitted and reflected light brightness in the *far field* [1] has been calculated by taking a Fourier transform of the outgoing electric field on the boundaries of the simulation region. We have also collected data relevant to the time evolution of the angular brightness distribution as well as the integrated energy flux in the far field. A typical time dependence of backscattered SBS reflectivity is shown in Fig. (4.4) for circular focus and $n_e/n_c = 0.1$, $I_0 = 1.7 \times 10^{15} W/cm^2$. The figure displays an initial phase of rapid growth followed by a quasi-stationary behavior, including regular oscillations on the scale of $\approx 50ps$. These oscillations are a consequence of a dynamic evolution of the narrow beam ($f_1 = 3$) self-focussing.

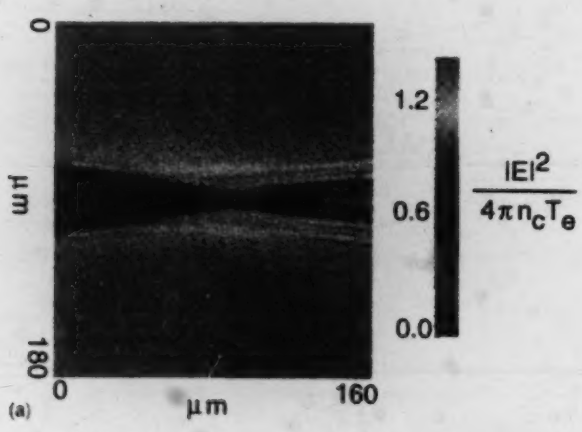

Figure 4.5: Circular focus – contour plot of the near field intensity distribution at $t = 10ps$.

The average reflectivity level is of the order of 10%. The backscattered reflectivity has been adjusted to experimental values through an appropriate choice for the ion acoustic wave damping and the magnitude of the electromagnetic seed. It is important to keep the backscattered reflectivity in simulations at moderate levels in order to prevent pump depletion from dominating the interaction [4, 7]. The angular spread of the backward SBS light in the simulations is several times larger than the focussing angle of the pump [6]. Therefore the integrated reflectivity in a near-backward direction is always higher ($\sim 40\%$) than the backward reflectivity collected by the focussing lens, as measured in experiments.

The SFI of the narrow Gaussian beam is also an important part of the early time evolution. The focussing of the narrow beam is illustrated by Figs. (4.5) and (4.6). Figure (4.5) shows a contour plot of the normalized electric field intensity distribution $|E|^2/4\pi n_c T_e$ at $t = 10ps$. The laser light propagates from the left and produces backscattered light represented here as short wavelength modulations which increase in the amplitude toward the left boundary. The SFI

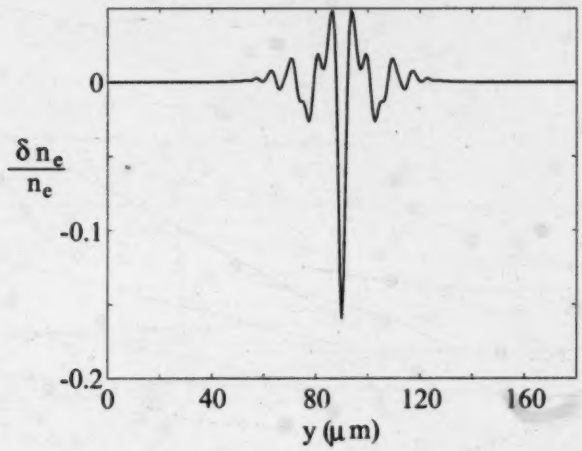

Figure 4.6: Circular focus – density cross section at best focus position at $t = 10ps$.

occurs after the SBS region, in the front part of the plasma and extends up to the right boundary. This evidence of the virtual separation of the two instabilities will be further stressed and discussed below.

Figure (4.6) shows a cross-section of the density perturbation at the current best focus position. Although these plots are for the circular focus, the line focus demonstrates similar behavior at early times. In both cases, only the narrow Gaussian portion of the laser beam undergoes an increase in intensity and shortening of transverse dimension. The characteristic self-focussing time defined by the propagation of density perturbations across the laser beam cross-section [1, 2] is given by

$$t_{sf} = f_1 \lambda_0 / c_s.$$

During this time the initial central part of the pump beam is focussed to a size of the order of one-two laser wavelengths [cf. Fig. (4.5)]. The further contraction is prevented by diffraction [4, 8]. Saturation of the SFI due to nonlinear density depletion does not play an important role at this stage in our 2D simulations,

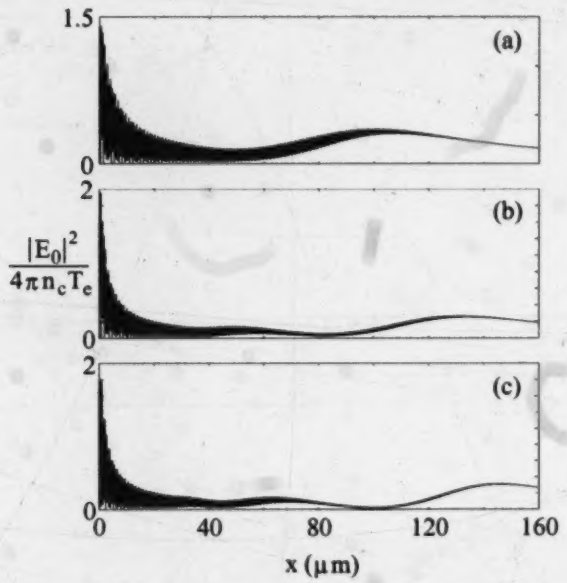

Figure 4.7: Near field intensity distribution along the axis of the laser beam propagation at different time moments: (a) 20*ps*, (b) 30*ps*, (c) 40*ps*.

because the corresponding density perturbations are at moderate levels of a few percent [cf. Fig. (4.6)].

Figure (4.7) shows a sequence of near field intensity distributions along the beam axis for different moments in time. The position of the focal spot is changing in time. It moves forward * in the direction of propagation of the laser light starting at x_f at $t = 0$. This evolution of a hot spot agrees with simulation results obtained previously in Ref. [2] the using paraxial optics approximation. This movement is a consequence of the refocussing of the laser beam by the narrow density channel, which acts as an effective plasma lens. The hot spot motion results in the oscillations of the backward SBS reflectivity displayed in Fig. (4.4).

*Hot spot dynamics have also been described in Refs.[13, 14]. In addition to motion away from the laser, which is associated with a formation of long filaments, the hot spot can move toward the laser if the focal plane is deep enough in the interaction region. However, these results did not include effects of SBS.

The speed of a hot spot can be estimated from the following considerations. In order to compensate for the divergence of a beam due to diffraction the lens formed in plasma should have a focal length equal or smaller than the Rayleigh length of the beam [4]. Assuming the lens formation time to be t_{sf} we can obtain an estimate for the speed of the local spot movement.

$$c_f = 2\pi f_1 c_s \sqrt{1 - n_e/n_c}. \tag{4.3}$$

This speed is supersonic and for parameters of Fig. (4.7), $c_f \approx 17c_s$ where we have assumed $f_1 = 3$. This predicted value for c_f is approximately two times higher than that inferred from numerical results in Fig. (4.7). The factor of two discrepancy can be accounted for by the change in the effective f-number, which decreases due to self-focussing of the narrow beam. This change of the effective f-number plays a very important role in the next two chapters where the main focus is the effect of self-smoothing.

4.4 Filamentation instability of the wide laser beam

Density fluctuations [cf.(4.6)] produced by channel formation and self-focussing of the narrow beam, provide a strong seed for the FI and near-forward SBS. These processes involve the wide Gaussian part of the beam defined by f_2 and E_{02} in Eq. (4.1). Well-developed linear filamentation can be observed at times as early as $t \sim 10ps$.

Figures (4.8)(a) and (4.8)(b) demonstrates the angular distribution of the transmitted and reflected light for this moment of time. The angular distribution of the transmitted light, Fig. (4.8)(a), shows two characteristic shoulders in the far field distribution, which extends within the angular range of about $\pm 6°$ forward direction. This is consistent with the linear spatio-temporal evolution

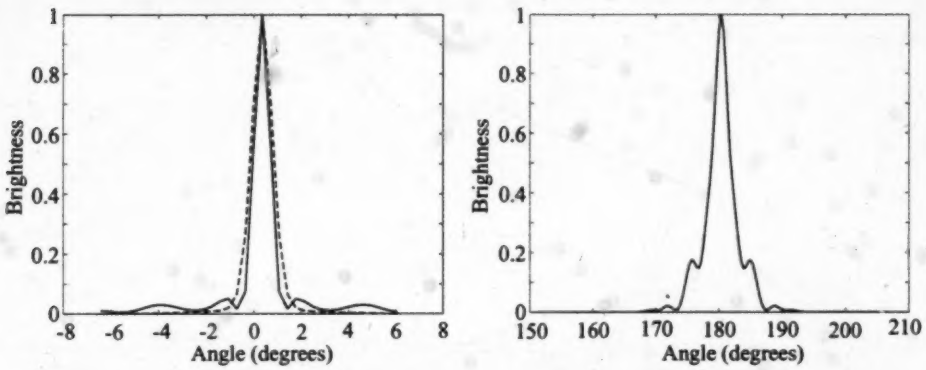

Figure 4.8: Far field angular distribution of (a) transmitted light at $t = 10ps$ (solid line) and at $t = 0ps$ (dashed line), and (b) reflected light at $t = 10ps$ for the parameters of Fig.(4.4).

of the FI as will be discussed later. Namely, the broadening of the spectrum of the transmitted light is a result of scattering of the laser pump on density modulations produced by the FI. The angular spread corresponds to the angle θ satisfying the relation

$$\sin\theta \approx k_{\perp m}/k_0, \tag{4.4}$$

where

$$\left(\frac{k_{\perp m}}{k_0}\right)^2 = \frac{n_e}{n_c}\frac{|E_0|^2}{16\pi n_c T_e} \tag{4.5}$$

is the wavenumber of the fastest growing mode in ponderomotive FI. For the parameters of Fig. (4.8)(a) this angle is approximately 7°. In addition, density perturbations resulting from the SFI of the narrow beam [cf. Fig. (4.6)] contribute to spreading of the laser beam at this early time of $\sim 10ps$.

Figure (4.8)(b) shows the far field distribution of the backscattered light at the same moment in time. Clearly the reflected light displays a much wider angular distribution as compared to the transmitted light. The broadening shown in Fig. (4.8)(b) is typical for backscattering from a small f-number hot spot [4, 6]. It is the combined effect of SBS taking place within a narrow density

channel and diffraction effects. Comparison between transmitted, Fig. (4.8)(a), and backscattered light, Fig. (4.8)(b), is additional evidence that filamentation and density modulations affecting transmitted light are spatially separated from the region of backward SBS growth. The contour density plot in Fig. (4.5) has already demonstrated this separation. This is one of the characteristic features of the interaction between backward SBS and filamentation, which persists at later times as well. In effect, both instabilities develop almost independently. This behavior is in contradiction to often-used arguments [cf., e.g. Ref. [3]] regarding filamentation significantly enhancing or affecting backward SBS. Still, only light that propagates through the region of backward SBS growth can support SFI. This in turn affects SBS and leads to reflectivity modulations in Fig. (4.4) due to moving hot spots early in time.

4.5 Near-forward SBS

With time, the angular distribution of the transmitted light changes and becomes more complicated. Figure (4.9)(a) shows transmitted light at the time $28ps$ for the circular focus. Comparison with Fig. (4.8)(a) discloses the enhanced spreading of the beam related to the FI of the broad beam and scattering by density fluctuations produced by SFI of the narrow beam.

However, Fig. (4.9) at the time $50ps$ shows very different shape for the angular distribution. Symmetric maxima in the transmitted light at approximately 15° are well outside the characteristic angle for the FI. This light is consistent with the angular dependence of a linear gain for near-forward SBS.

Similar angular distributions of the transmitted light are shown on Figs. (4.10) (a) and (b) for the line focus, for times $t = 10ps$ and $t = 28ps$ respectively.

The important information, which is needed to discriminate SBS from FI scattered signal, is the frequency spectrum of the transmitted light. Figure (4.11)

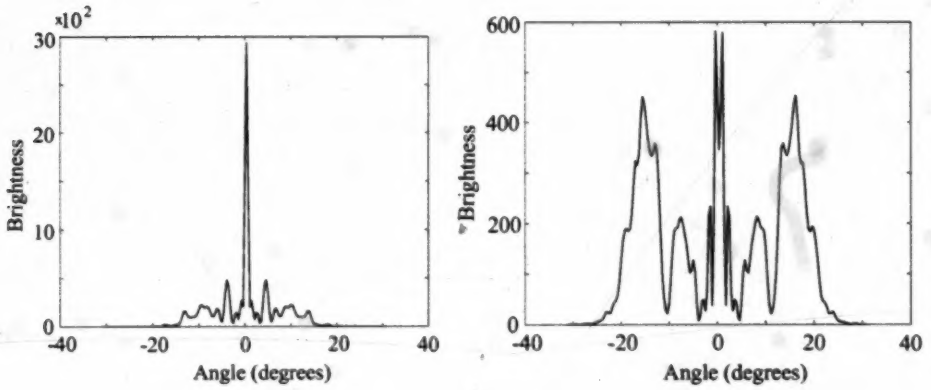

Figure 4.9: Circular focus – far field angular distribution of the transmitted light at $t = 28ps$ (a) and $t = 50ps$ (b) for the parameters of Fig. (4.4).

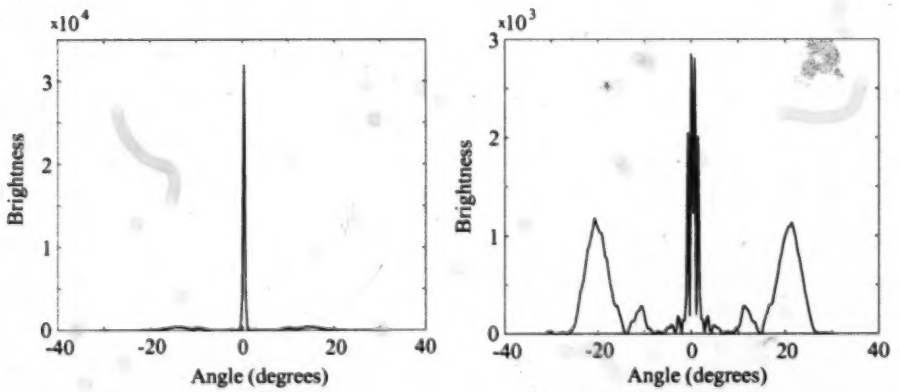

Figure 4.10: Line focus – far field angular distribution of the transmitted light at $t = 10ps$ (a) and $t = 28ps$ (b) for the parameters of Fig. (4.4).

shows the frequency spectra of the light propagating in different directions, 5°, 10° and 15° for a circular focus at $n_e/n_c = 0.1$, $I = 1.7 \times 10^{15} W/cm^2$. It is evident that the transmitted light has a red shift, which increases with the propagation angle in the forward direction. The dominant shift agrees well with the ion-acoustic wave frequency, satisfying the resonance condition for the near-forward SBS:

$$\omega_2 = k_2 c_s,$$

where

$$k_2 = 2k_0 = 2\frac{\omega_0}{c}\sqrt{1 - n_e/n_c}\sin\theta/2.$$

For small angles of propagation (at 5°, Fig. (4.11)), the spectrum also contains unshifted components as a result of a scattering on stationary density fluctuations, produced by FI and SFI. Spectra of the light scattered into negative angles with respect to 0° are very similar to Fig. (4.11). The straight light at 0^o displays small scale modulations and broadening from a complicated late time density distribution.

4.6 Late time evolution

Figure (4.12) represents the near-field laser intensity and plasma density distributions for the case of the circular focus at a later time $\sim 100ps$. The contour plot of the ponderomotive potential in Fig. (4.12)(a) clearly shows that the separation between regions of backward SBS growth (the rear part of the hot spot, on the left side of the figure) and the one, where near forward SBS, filamentation and SFI (the front part of the hot spot, on the right half of the figure) is preserved in time.

An important physical process contributing to this complicated and time changing distribution of the electric field, Fig. (4.12)(a), and plasma density, Fig. (4.12)(b), is the *nonlinear evolution* of the SFI [10]. The SFI leads to

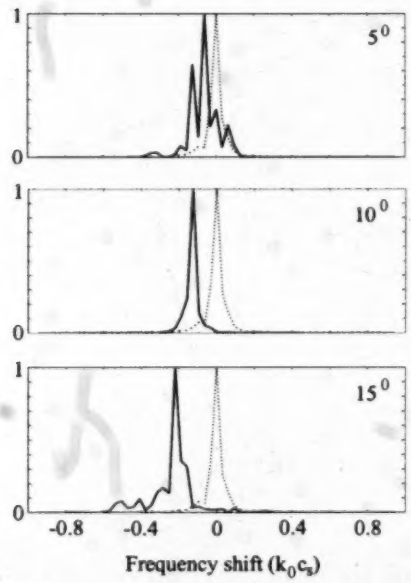

Figure 4.11: Circular focus – frequency spectra of the transmitted light propagating at different angles from the direction of the laser pump (dotted line) for the parameters of Fig. (4.4). The spectra have been calculated by taking Fourier transform of the data collected over the duration of the run, i.e. $\sim 100ps$

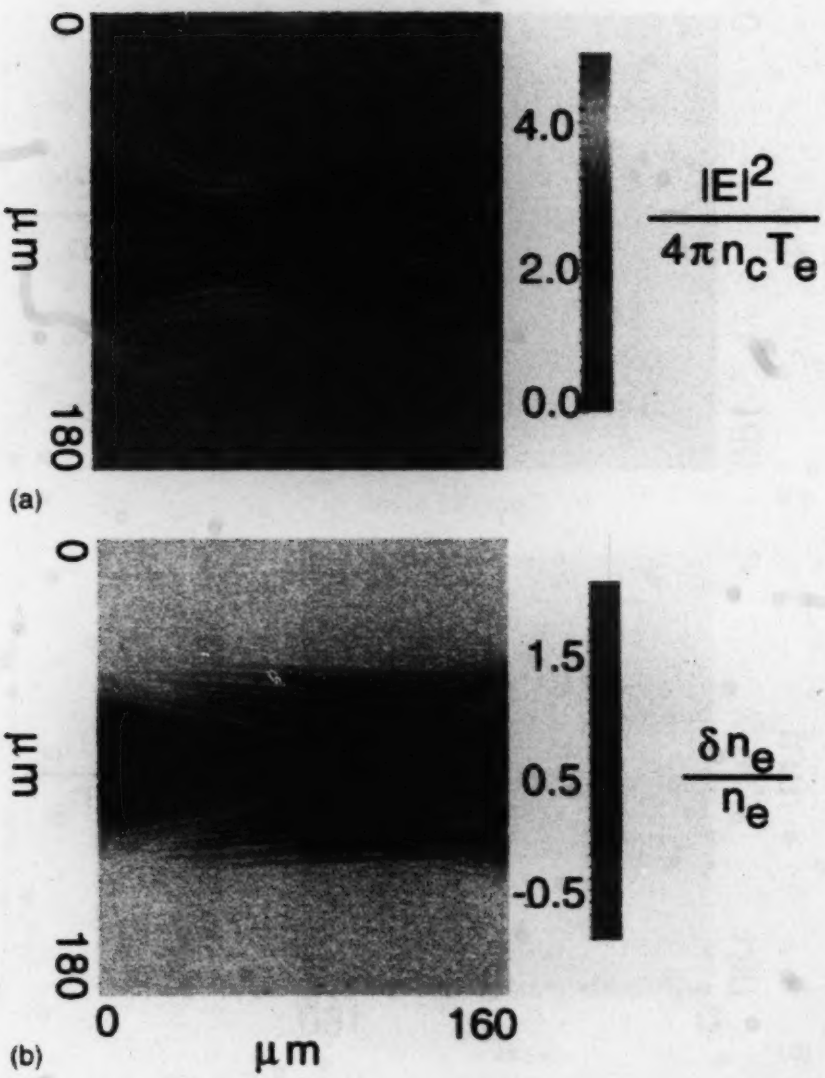

Figure 4.12: Circular focus – near field intensity(a) and density (b) distributions at $t = 100ps$ for the parameters of Fig. (4.4).

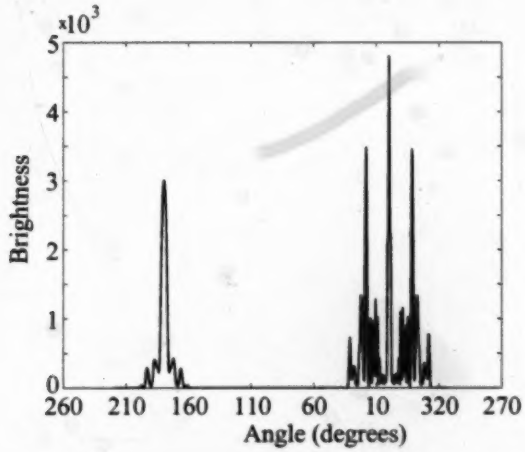

Figure 4.13: Circular focus – far field angular distribution of the transmitted and reflected light at $t = 100ps$ for the parameters of Fig. (4.4).

formation of several small scale intensity maxima during the decay of intense hot spots, which contain a power P above the critical value P_c[†], i.e.

$$P/P_c = 2.65 f^2 \frac{n}{n_c} \frac{|E_0|^2}{4\pi n_c T_e} \gg 1. \tag{4.6}$$

As the initial ratio of P/P_c for the narrow beam equals 13.4 for our parameters, we observe in the simulations a very pronounced hot spot power redistribution.

Figure (4.13) shows the far field distribution of the transmitted and reflected light at the same late time ($t = 100ps$) as the near field plots in Fig. (4.12). The multiple speckles in the plasma introduce phase perturbations in the propagating electromagnetic field, which result in small scale, high amplitude variations in the angular distribution of the transmitted light, which is reminiscent of the RPP distribution. This distribution in brightness is also changing in time due to the dynamic evolution of hot spots. None of these phase variations have been introduced into the backscattered light, once again demonstrating the spatial separation of backscattered SBS and SFI. A similar evolution of the laser beam

[†]Here the critical power, P_c, is defined for 3D geometry according to Ref. [13].

structure has been found previously in simulations with a simple Gaussian beam profile [4, 7]. However the large angle component in the transmitted light is especially enhanced in our simulations due to the presence of a small f-number Gaussian part of the laser beam.

An important characteristic of this nonlinear stage of the interaction process is the effective widening of the laser beam, which spreads outside the original width, defined by the focussing optics. This increases on average the gain length for wide-angle SBS side-scattering. The electric field, Fig. (4.14) (a), and plasma density, Fig. (4.14) (b), distributions for the line focus at the relatively late time illustrates similar physical processes as the circular focus images, Fig. (4.12), with clearly visible density fluctuations due to side scattered SBS. However both density and intensity perturbations are more regular as compared to late time circular focus images in Fig. (4.12) which are strongly affected by the short scale intense hot spots. This is also reflected in the far field angular distribution of the transmitted light, Fig. (4.15), indicating the existence of a density grating in the plasma with the dominant wave vector.

An analytical description of the late time evolution of our simulation results is a difficult problem falling between the relatively well understood theory of a single Gaussian hot spot and the complicated, broad and time dependent intensity distribution in the plasma giving rise to the angular distribution of the far field radiation, which is typical for RPP beams. This effect can be described as the self-induced plasma smoothing of the laser light, presented in greater detail in the next Chapter 5.

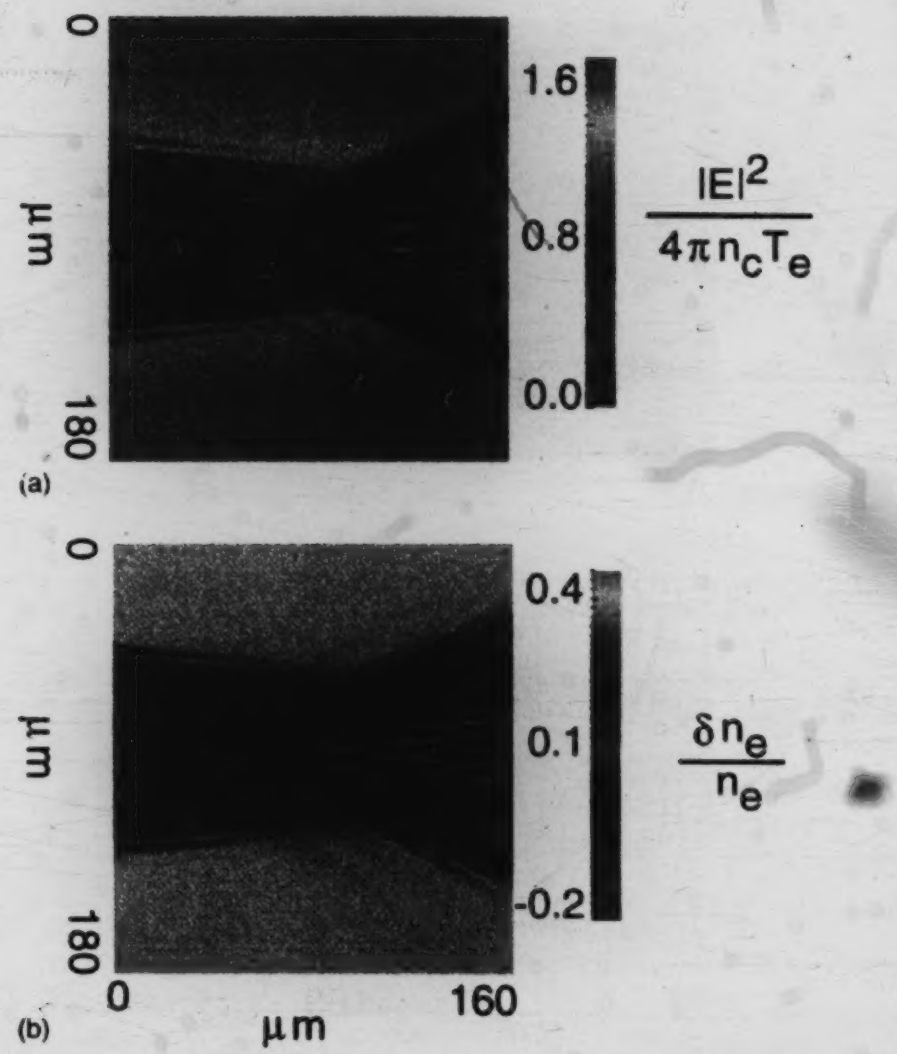

Figure 4.14: Line focus – near field intensity(a) and density (b) distributions at $t = 50ps$ for the parameters of Fig. (4.4).

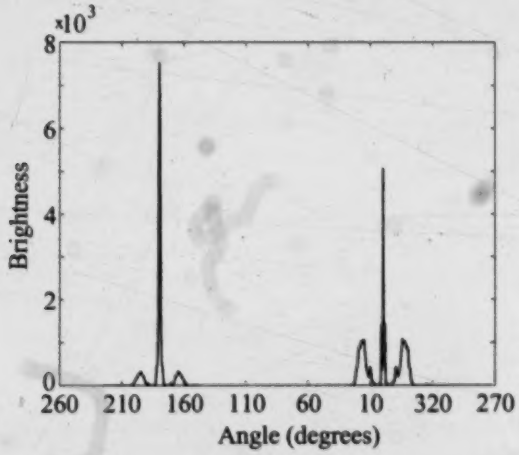

Figure 4.15: Line focus – far field angular distribution of the transmitted and reflected light at $t = 100ps$ for the parameters of Fig. (4.4).

4.7 Reflected and transmitted light as function of plasma density

We have also compared the theoretical predictions with the experimental measurements of the reflected and transmitted energy from Ref. [19]. In the experiment, all light emitted from the plasma was collected with $f/2$ optics, which corresponds to collection inside a 14° cone.

Figure (4.16) shows the dependence of the reflected (dashed line with circles) and transmitted (solid line with asterisks) light on the plasma background density. The light power has been calculated from the simulation results within the 14° cones in the forward and backward direction at laser intensity of $I = 1.7 \times 10^{15} W/cm^2$. Our results are consistent with the experimental observations shown in Ref. [19] at higher laser intensities, displaying more light propagating outside the forward cone of 14° and not being accounted for in Fig. (4.16) for higher densities. This can be explained, both in terms of scaling properties of the deflection angle due to the FI [17] and in terms of side-scattered SBS. The

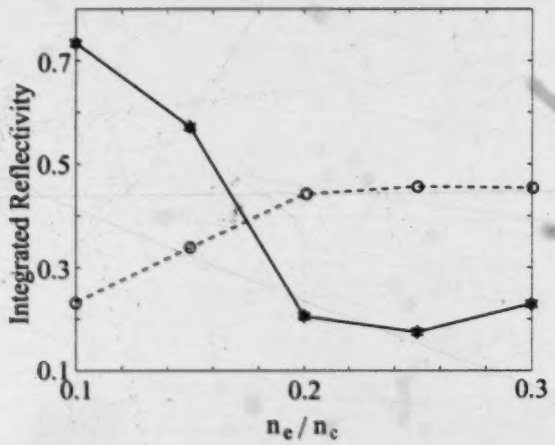

Figure 4.16: Circular focus – transmitted and reflected light integrated within the 14° cone as a function of density for intensity $I_0 = 1.7 \times 10^{15} W/cm^2$. The figure shows the dependence of the reflected (dashed line with circles) and transmitted (solid line with asterisks) light on the plasma background density.

amount of backscattered light in Fig. (4.16) within the cone of 14° saturates at higher densities and shows a small intensity increase outside the cone defined by the focussing optics.

4.8 Spatio-temporal evolution of near-forward SBS and FI

The angular spread, spectra and intensity distribution of the transmitted light in simulations as well as in experiments depend on the FI and near-forward SBS. In order to facilitate interpretation of numerical and experimental data we summarize in this section the results of the linear theory of the spatio-temporal evolution of these instabilities relevant to the conditions of our simulations. We show that within the duration time of the pulse, i.e. approximately $100ps$, linear theory gives an accurate prediction of the temporal growth of both instabilities. At first, the FI grows at a rate comparable to near-forward SBS. However, it

saturates at an earlier time and is restricted to smaller deflection angles. Forward SBS dominates interactions at later times and is primarily responsible for the observed large angle scattering. SBS produces red-shifted spectral components in the transmitted light shown in Fig.(4.11), which is also observed experimentally.

In Subsection 4.8.1 we present a model of the near-forward SBS, which appears to dominate the interactions described in our simulations. The discussion of the effect of the finite transverse size of the laser pump on the SBS is given in Subsection 4.8.2. Filamentation is addressed in Subsection 4.8.3.

4.8.1 Near-forward stimulated Brillouin scattering

The linear evolution of near-forward SBS has been obtained from a simple model that describes the resonant interaction between an electromagnetic wave of amplitude E_1 propagating at an angle θ from the forward direction, and an ion-acoustic wave with wavenumber k_s coupled to an electromagnetic pump plane wave propagating along the X-axis. Consider an approximation in which the electric field is decomposed into a pump, E_0, and scattered wave, E_1, components

$$E(\mathbf{r},t) = E_0(\mathbf{r})e^{ik_0 z} + E_1(\mathbf{r},t)e^{i\mathbf{k}_1\cdot\mathbf{r}}. \tag{4.7}$$

To determine the decomposition of the density perturbation we take into account that the source term in Eq. (2.91) is proportional to

$$|E|^2 = |E_0|^2 + |E_1|^2 + E_0E_1^*e^{i(k_0z-\mathbf{k}_1\cdot\mathbf{r})} + E_0^*E_1e^{-i(k_0z-\mathbf{k}_1\cdot\mathbf{r})}, \tag{4.8}$$

and we span the density perturbation onto the same basis of exponential functions:

$$\delta n_e(\mathbf{r},t) = \delta n_1(\mathbf{r},t)e^{i(\mathbf{k}_0\cdot\mathbf{r}-\mathbf{k}_1\cdot\mathbf{r})} + c.c.. \tag{4.9}$$

Here we used that the density perturbation is a real quantity $\delta n_e = \delta n_e^*$ and that $k_0 z = \mathbf{k}_0 \cdot \mathbf{r}$. If in addition we use the matching condition Eq. (2.50) to obtain

$$\delta n_e(\mathbf{r}, t) = \delta n_1(\mathbf{r}, t) e^{i(\mathbf{k}_s \cdot \mathbf{r})} + c.c. \tag{4.10}$$

The vector configuration for the forward SBS is shown in Fig. (2.4).

Substitution of Eq. (4.7) and Eq. (4.10) into Eq. (2.91) and Eq. (2.88) yields

$$2i\frac{\omega_0}{c^2}\frac{\partial E_1}{\partial l} + 2i\mathbf{k}_1 \cdot \nabla E_1 = \frac{\omega_0^2}{c^2 n_c}\delta n_1^* E_0, \tag{4.11}$$

$$\left(\frac{\partial^2}{\partial t^2} + 2\gamma_s\frac{\partial}{\partial t} + c_s^2 k_2^2\right)\delta n_1 = -\frac{c_s^2 k_2^2 n_e}{16\pi n_c T_e} E_0 E_1^*, \tag{4.12}$$

where we have neglected all the non-resonant terms and the Laplacians of the slowly varying amplitudes of the electric field. A simple estimate shows that the first term in Eq. (4.11)

$$\frac{\omega_0}{c^2}\frac{\partial E_1}{\partial l} \ll \mathbf{k}_1 \cdot \nabla E_1,$$

so it can be neglected too. Finally we rotate the coordinate system so that one of the axis is parallel to the vector $\mathbf{k}_1$ and constitutes an angle θ to the $x - axis$ and obtain

$$2v_g\frac{\partial E_1}{\partial l} = -i\omega_0\frac{\delta n_1^*}{n_c}E_0, \tag{4.13}$$

$$\left(\frac{\partial^2}{\partial t^2} + 2\gamma_s\frac{\partial}{\partial t} + c_s^2 k_2^2\right)\delta n_1 = -\frac{c_s^2 k_2^2 n_e}{16\pi n_c T_e} E_0 E_1^*, \tag{4.14}$$

where $v_g = k^2 c^2/\omega_0$ is the group velocity of the scattered wave and l is the distance measured along the direction of propagation (parallel to $\mathbf{k}_1$).

This approximation is also valid in the regime of strongly driven SBS, where the growth rate is comparable to or larger than the ion-acoustic perturbation frequency. The spatio-temporal evolution is calculated from the inverse Laplace transform integral

$$E_1(\theta, t) = E_{seed}\int \frac{ds}{2\pi\omega_s} e^{ist + i\lambda_1(s)l} \tag{4.15}$$

where E_{seed} represents the amplitude of the electromagnetic seed, $l = L/cos(\theta)$ is the amplification length calculated along the direction of the propagation of the scattered light. The function λ_1 in the absence of ion-wave damping has the following form

$$\lambda_1(s) = -2\frac{\omega_2}{v_g}\frac{\gamma_0^2}{s^2 - k_2^2 c_s^2}, \tag{4.16}$$

where the homogeneous SBS growth rate

$$\gamma_0^2 = w_0 k_2 c_s \frac{n_e}{n_c}\frac{|E_0|^2}{64\pi n_c T_e}, \tag{4.17}$$

and the group velocity of the light is given by

$$v_g = c\sqrt{1 - n_e/n_c}. \tag{4.18}$$

Using a saddle point analysis of the integral in Eq. (4.15) we find two characteristic solutions for SBS growth. In the strongly driven regime $|s| \gg \omega_2$, SBS varies as $\exp(i\delta_1 t)$, where

$$\delta_1 = \frac{3}{2}\left(1 - i\sqrt{3}\right)\left(\frac{\omega_2\gamma_0^2 l}{2v_g t}\right)^{1/3}. \tag{4.19}$$

With time, the SBS growth $Im(\delta_1)$, decreases and the instability reaches a weakly driven regime where the time variation of E_1 is given by $\exp(i\omega_2 t + \delta_2 t)$ with $\delta_2 \ll \omega_2$,

$$\delta_2 = 2\gamma_0\sqrt{l/v_g t}. \tag{4.20}$$

Figures (4.17)(a) and (4.17)(b) illustrate the different regimes of the linear evolution of near-forward SBS by displaying the time of strongly-driven SBS threshold (dotted lines defined by $Im(\delta_1)t = 1$) and the time for transition between weakly and strongly driven SBS (lines 2 defined $Im(\delta_1) = \delta_2$). These two figures have been drawn for two sets of parameters: $I = 1.7 \times 10^{15} W/cm^2, n_e/n_c = 0.2$ [Figure (4.17)(a)], which has been used in most of our simulations as well as in several moderate-density experiments and $I = 5 \times 10^{16} W/cm^2, n_e/n_c = 0.05$

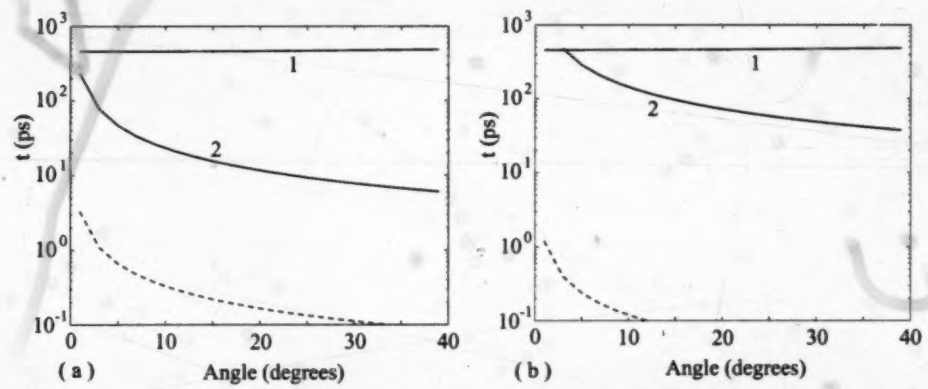

Figure 4.17: Characteristic regimes of the linear evolution of the near-forward SBS, based on Eq. (4.19) and Eq. (4.20), shown for two sets of parameters: (a) $I = 1.7 \times 10^{15} W/cm^2, n_e/n_c = 0.2$, $l = 100\mu m$, (b) $I = 5 \times 10^{16} W/cm^2, n_e/n_c = 0.05$, $l = 100\mu m$. Dashed lines show the time when the instability reaches the strongly driven SBS threshold, lines 2 show the transition time between the weakly and strongly driven SBS, and lines 1 display possible saturation time, due to the convection of sound waves in transverse direction.

[Figure (4.17)(b)], which characterizes high-intensity experiments. In each case $T_e = 1keV$ and $\lambda = 1\mu m$. The characteristic length was set to $l = 100\mu m$.

We have also displayed the time (lines 1) of possible saturation due to the convection of sound waves in the transverse direction. In the absence of strong damping this is the only mechanism which can lead to a stationary near-forward SBS. However for our parameters the transverse interaction length is $\delta y \sim 100\mu m$ so that this time $\sim \delta y/c_s$ is very long and has no significance on the $100ps$ scale of the experimental laser pulse.

Figure (4.17)(a) shows that during most of this time and for relatively large angles, SBS is weakly driven. At higher intensities the strongly driven SBS dominates during the pulse [cf. Fig.(4.17)(b)].

The characteristic time evolution of SBS as given by Eq. (4.19) or Eq. (4.20) also defines the magnitude of the red shift of the deflected electromagnetic radiation. Our numerical results are consistent with the parameter set correspond-

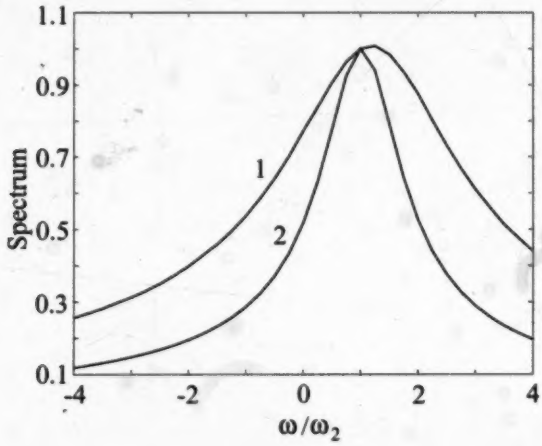

Figure 4.18: Comparison between the normalized spectra, calculated fromEq. (4.15) for strongly driven SBS (line 1) for $I = 1 \times 10^{16} W/cm^2$, $n_e/n_c = 0.2$, and for weakly driven SBS (line 2) for $I = 2 \times 10^{15} W/cm^2$, $n_e/n_c = 0.2$. The frequency is normalize to $\omega_2 = 2k_0 c_s \sin\theta/2$.

ing to Fig. (4.17)(a) and accordingly they show a red shift defined by ω_2 [cf. Fig.(4.11)].

The experimental data also includes results of high-intensity interactions [cf. Fig. (4.17)(b)] and therefore display larger spectral shifts of the transmitted light, which could be consistent with strongly driven SBS.

We calculated numerically the Fourier spectra of the scattered light obtained from linear theory, Eq. (4.15), and analyzed the results for a wide range of parameters, often for pump intensities, which are inaccessible in the numerical simulations because of steep spatial gradients generated during the non-linear stage of temporal evolution. Figure (4.18) shows an example of a comparison between the normalized spectra produced by a strongly driven SBS (line 1) for $I = 1 \times 10^{16} W/cm^2, n_e/n_c = 0.2$ and by weakly driven SBS (line 2) for $I = 2 \times 10^{15} W/cm^2, n_e/n_c = 0.2$. The frequency is normalized to ω_2 which depends on the scattering angle, i.e. Fig. (4.18) is valid for all deflection angles θ. The Fourier

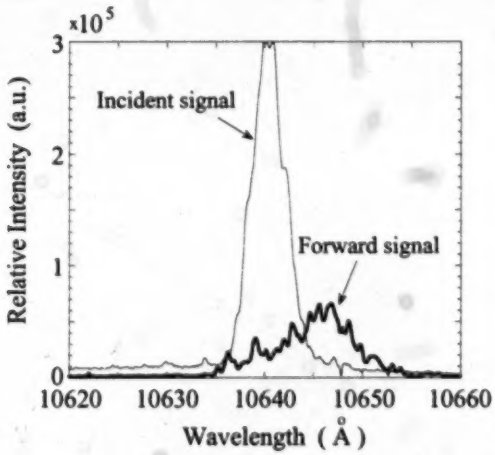

Figure 4.19: Experimental frequency spectrum at $\theta = 23°$ for the laser peak intensity $I = 5 \times 10^{16} W/cm^2$,$n_e/n_c = 0.2$ and peak plasma density is $0.28 n_c$.

transform has been taken over the time-window $0 < t < 20/\omega_2$. As expected, the spectrum for the weakly coupled SBS peaks at $\omega = \omega_2$ and it is much narrower as compared to the spectrum of the strongly driven SBS (line 1) which is shifted further towards higher frequencies. Experimental data [19, 17, 22], exhibit the qualitative features shown by line 1 in Fig. 4.18.

Figure 4.17 does not show any restriction on the angle of deflection θ. This is a consequence of assuming a plane wave pump with no limitation on the interaction length in different directions. To improve the predictions of the linear theory we introduce in the next subsection a more realistic model of the laser pump with finite transverse dimensions for the case of weak SBS coupling.

The broader component in Fig. (4.18) resembles the spectra observed in the experiment, Fig. (4.19), in which the signal was collected at a forward angle of 23°. The signal was collected by a lens (collection solid angle of $2 \times 10^{-3} sr$), which coupled the light through an optical fiber to $1.2m$ spectrometer which dispersed the light. The signal was time resolved with an optical spectrometer ($\sim 50ps$

time resolution). Forward-scattered signals could be observed only for incident intensities greater than $5 \times 10^{15} W/cm^2$; over this intensity range the wavelength shift was approximately constant. For the signal shown in Fig (4.19) the laser intensity is $5 \times 10^{15} W/cm^2$ and the peak density is $0.28 n_c$. The experimental spectrum is shifted further to the red than the results for the strongly-driven near-forward SBS would indicate. Several additional processes, including hydrodynamic evolution or localized heating of the plasma could account for this additional effect.

4.8.2 Effect of the finite transverse size laser pump

The results discussed below are derived from an analytical solution of the SBS model, which in addition to the weakly driven approximation and no pump depletion, includes a laser pump intensity variation along the direction of propagation of the scattered light. This limits the SBS gain length, particularly at large angles in forward direction. The FI is less affected as it develops within a smaller angular spread.

The analysis following Eq. (4.15) leads to different regimes of SBS growth shown in Fig.(4.17). Clearly the inhomogeneity in the transverse dimension of the laser pump will limit SBS amplification for larger angles of propagation, θ, of the scattered light. In order to obtain an approximate expression for the scattered light amplitude we further simplify Eq. (4.13) and Eq. (4.14) limiting our description to the weakly coupled SBS. This is the dominant regime of SBS evolution observed in simulations [cf. Fig.(4.11). Enveloping in time the amplitude

$$E_1 = E_s \exp(i\omega_2 t), \tag{4.21}$$

$$\delta n_1 = \delta n_s \exp(-i\omega_2 t), \tag{4.22}$$

about the frequency $\omega_2 = k_2 c_s$ we obtain from Eq. (4.13) and Eq. (4.14) that

$$2v_g \frac{\partial E_s}{\partial l} = -i\omega_0 \frac{\delta n_s^*}{n_c} E_0, \tag{4.23}$$

$$\left(\frac{\partial}{\partial t} + \gamma_s\right) \delta n_s = -i \frac{c_s k_2 n_e}{32\pi n_c T_e} E_0 E_s^*, \tag{4.24}$$

The boundary conditions, $E_s(l = 0, t) = E_{seed}$ and $\delta n_s(l, t = 0) = 0$ include an electromagnetic seed wave for side-scattered SBS and no initial density perturbations.

Combining Eq. (4.24) and Eq. (4.13) and defining a new function [16]

$$a(l, t) = \delta n_s^* \exp(-\gamma_s t) \tag{4.25}$$

we obtain a second order PDE for the function a [cf. Ref.[11]]

$$\frac{\partial^2 a}{\partial t \partial l} - \frac{\gamma_0(l)^2}{v_g} a = 0, \tag{4.26}$$

where γ_0 depends on l due to the intensity of the pump, which is inhomogeneous in y-direction. Solving Eq. (4.26) using the method of Riemann functions [16, 11] and introducing the SBS amplification due to the inhomogeneous laser pump intensity as a new variable

$$\xi(\theta) = \frac{1}{v_g} \int_0^l \gamma_0^2(l') dl', \tag{4.27}$$

we obtain

$$a(\xi, t) = \int_0^t dt' I_0(2\sqrt{\xi(t - t')} \frac{\partial}{\partial t'} a(0, t'). \tag{4.28}$$

Here I_0 is the modified Bessel function of zeroth order. From the last equation by using Eq. (4.24) to express the time derivative of a at $\xi = 0$ via the electromagnetic seed, we obtain the following expression for the the temporal dependence of the scattered wave amplitude

$$\frac{E_s(\theta, t)}{E_{seed}} = 1 + \int_0^t dt' \sqrt{\xi/t'} I_1\left(2\sqrt{\xi t'}\right) e^{-\gamma_s t'}. \tag{4.29}$$

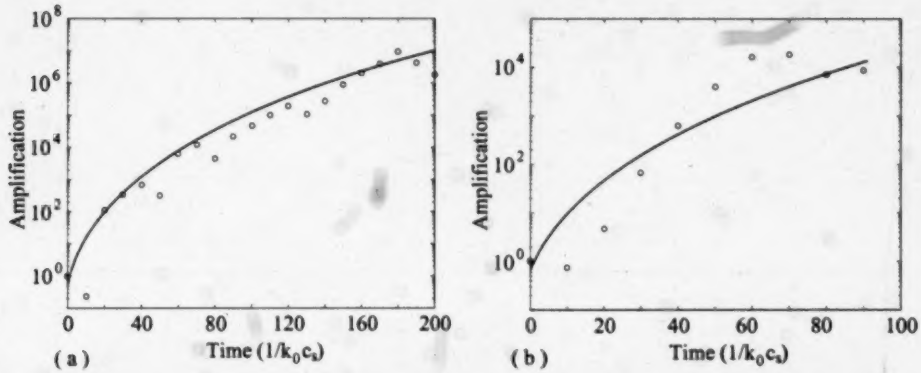

Figure 4.20: Comparison between the simulations results (small circles) and analytical results (solid line), based on Eq. (4.29) for circular focus (a) and line focus (b). The transmitted light propagates at 20^0 off the forward direction. Parameters are $I = 1.7 \times 10^{15} W/cm^2$, $n_e/n_c = 0.2$.

One can see from Figs. 4.13 and 4.14 that the width of the laser beam has increased up to three times over its initial width. In addition, the speckle structure of the electromagnetic field is not stationary. The characteristic time for changes in the beam structure is shorter than the growth time of forward SBS, so when comparing the analytical result from Eq. (4.29) with the numerical simulations one can time average the intensity distribution.

In order to account for widening and splitting of the pump, for both circular and line focusses, we have used the intensity distribution constructed from two Gaussian beams with corresponding initial f-number for the wider beam [cf. Eq. (4.1)], namely $f = 18$ for circular focus, and $f = 36$ for line focus. The two beams were shifted across from the laser axis by a distance $1.6f\lambda_0$ for circular focus, and $f\lambda_0$ for line focus. These two parameters were adjusted to obtain the best agreement with the numerical simulation results. Such an agreement is illustrated in Figs. 4.20, which shows the time evolution of the transmitted light for a direction 20^0 off the forward direction. The small circles correspond to results from simulations and the solid lines to predictions of the linear theory based on

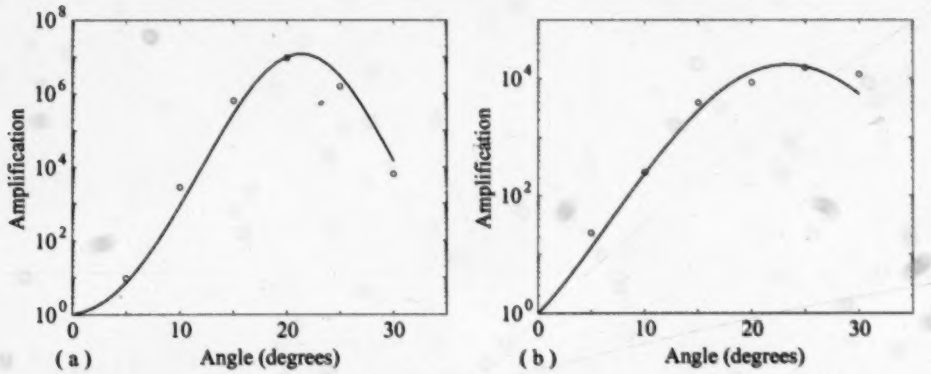

Figure 4.21: Results of the SBS gain calculations from Fig. (4.20) for different angles, shown for circular focus (a) and line focus (b). The parameters are as in Fig.(4.20).

Eq. (4.29). All parameters are from typical runs for $I = 1.7 \times 10^{15} W/cm^2$ and $n_e/n_c = 0.2$. The data from the simulations is normalized to the corresponding initial level of the transmitted light. Simulation results for the circular focus, Fig. 4.20(a), demonstrate a very good agreement with the linear model. Line focus data, Fig. 4.20(b), shows an oscillatory behavior around the average values of the simplified analytical model. The reason for these oscillations may be the late onset time of the forward SBS, because of the slower development of self-focussing and filamentation in comparison with the circular focus case.

The angular distribution of the forward scattered light at $t = 100ps$ for circular focus is shown on Fig. (4.21)(a) and the one at $t = 50ps$ for line focus is shown on Fig. (4.21)(b). The small circles correspond to results from our two-dimensional simulations while the solid line depicts $|E_1(\theta, t)|^2$, obtained from Eq. (4.29), where the interaction length $l = 160\mu m$ was the same as in simulations. In perpendicular direction the intensity distribution was approximated by a Gaussian profile. The simulation points have been obtained from the far field values [Figs.(4.13),(4.15)]. The analytical results have been obtained with

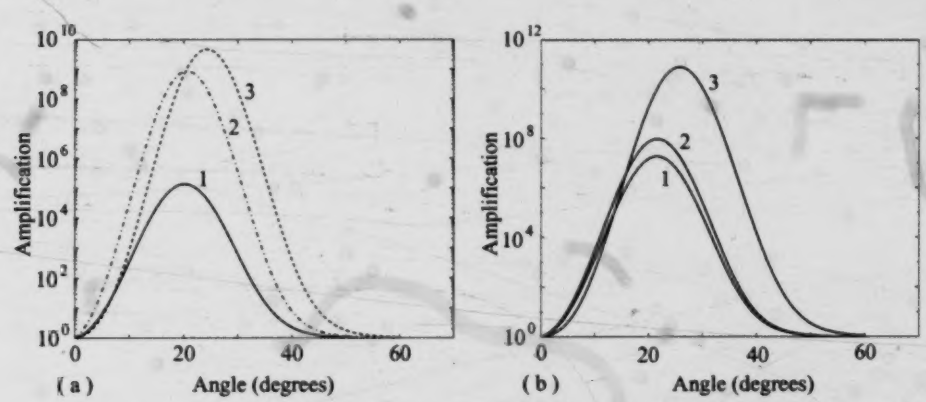

Figure 4.22: Circular focus. Results of the linear theory calculations of the near-forward SBS gain Eq. (4.29)) as a function of deflection angle for different densities (a): n_e/n_c : (1)0.1, (2)0.2, (3)0.3, for intensity $I = 1.7 \times 10^{15} W/cm^2$ at time $t = 50ps$ Similar gain calculations for different laser intensities (b): I : (1)$1.7 \times 10^{15} W/cm^2$, (2)$5 \times 10^{15} W/cm^2$, (3)$10 \times 10^{15} W/cm^2$. for density $n_e/n_c = 0.05$.

the pump model described above and adjusted to achieve a better comparison of the time evolution shown in Fig. (4.21). The good agreement between SBS analytical theory and full simulation results gives an additional indication that forward SBS dominates the interaction process at late times.

Finally, the results of the linear theory Eq. (4.29) with a finite cross-section pump, adjusted to fit the transmitted light are given on Fig. (4.22). Figure (4.22)(a) shows the amplification of the small signal go forward SBS for the circular focus, $I = 1.7 \times 10^{15} W/cm^2$, at time $t = 50ps$ for different plasma densities as a function of deflection angle. Clearly, the increase of plasma density leads to an increased broadening of the transmitted light due to near-forward SBS, an effect observed also experimentally. A similar dependence is observed with the increase of pump strength as shown on Fig. 4.22(b).

4.8.3 Filamentation instability

The role of the FI in the spreading of the transmitted light has been discussed before [19, 17]. Here we review the main features of spatio-temporal evolution of FI in order to compare it with SBS.

The linear evolution of the electric field perturbation, E_f, of electromagnetic waves participating in ponderomotive filamentation can be obtained from integral similar to Eq. 4.29

$$E_f(\theta,t) = E_{seed}\int \frac{ds}{2\pi k_0 c_s} e^{ist+i\lambda_f(s,q)L}, \tag{4.30}$$

where the wave vector q defines the direction of propagation of unstable electromagnetic waves ($\tan\theta = q/k_0$). For negligible ion-acoustic damping, λ_f, has the following form:

$$\lambda_f(s,q) = \frac{q^2}{2k_0}\left(\frac{1+q_c^2c_s^2}{s^2-q^2c_s^2}\right)^{1/2}. \tag{4.31}$$

Here we introduced the maximum wavenumber

$$q_c^2 = k_0^2\frac{n_e}{n_c}\frac{|E_0|^2}{8\pi n_c T_e} \tag{4.32}$$

which defines region $q \le q_c$ of unstable transverse perturbations.

In the long time limit with $s \to 0$, the instability reaches a stationary state with spatial growth $\exp(k_s L)$ where

$$k_s = \frac{qq_c}{2k_0}\sqrt{1-(q/q_c)^2} \tag{4.33}$$

In order to find intermediate asymptotic solutions, we have approximated the integral in Eq.(4.30) by the value of the integrand at $s = \sigma_i$ with solutions σ_i found from the constant phase condition. During the initial fast evolution of the instability, i.e. for $q \ll q_c \ll s/c_s$, the condition for the stationary phase has a solution corresponding to the exponential growth of the FI, $\exp(\sigma_1 t)$, where

$$\sigma_1(t) = \left(\frac{q_c^2c_s^2q^2L}{2k_0t}\right)^{1/3} \tag{4.34}$$

The solution is similar to the regime of strongly coupled SBS, Eq. (4.19). With time, σ_1 decreases and the growth of the FI is defined by $s = \sigma_2$, which satisfies the condition $q \ll \sigma_2/c_s \ll q_c$, (the regime of weak coupling) where

$$\sigma_2(t) = \left(\frac{q_c c_s q^2 L}{2k_0 t}\right)^{1/2}. \tag{4.35}$$

Figure (4.23) illustrates the results of the linear analysis of the ponderomotive filamentation for two characteristic parameter sets; $I = 1.7 \times 10^{15} W/cm^2$, $n_e/n_c = 0.2$ [Fig. 4.23(a)], which were used in most of our simulations as well as in several moderate intensity experiments; $I = 5 \times 10^{16} W/cm^2$, $n_e/n_c = 0.05$ [Fig. 4.23(b)], which characterize high intensity experiments. In addition, the interaction length in Eq. (4.34) and Eq. (4.35) was assumed to be $L = 100\mu m$. The other parameters were $T_e = 1keV$, $\lambda = 1\mu m$. Both figures show different regimes of FI growth as a function of the angle θ and the interaction time, t. Line 1 shows the time, defined by the relation $\sigma_2(t)t = k_s L$, when the FI growth reaches maximum defined by a stationary gain. Line 2 is defined by $\sigma_1(t) = \sigma_2(t)$ and indicates the time of transition between the strong coupling growth rate, Eq. (4.34), and weak coupling, Eq. (4.35). The dashed lines define the thresholds, $\sigma_i t = 1, (i = 1, 2)$. Line 1 limits the region of non-stationary growth where $\sigma_i t < k_s L$.

For the characteristic parameters used in Figs. (4.23)(a) and (4.23)(b), the time dependent growth dominates the development of the FI during the first $100ps$, which corresponds to the pulse duration in the experiments [19]. At smaller angles the growth is described mainly by $\exp(\sigma_2 t)$, while at larger θ values the instability becomes stationary before it can reach that regime. This higher intensity of Fig. (4.23)(b) is responsible for almost doubling the deflection angles of the transmitted light.

Comparison between the temporal growth of the FI, Eq. (4.34), and SBS, Eq. (4.19), reveals another interesting feature of the linear theory, namely that

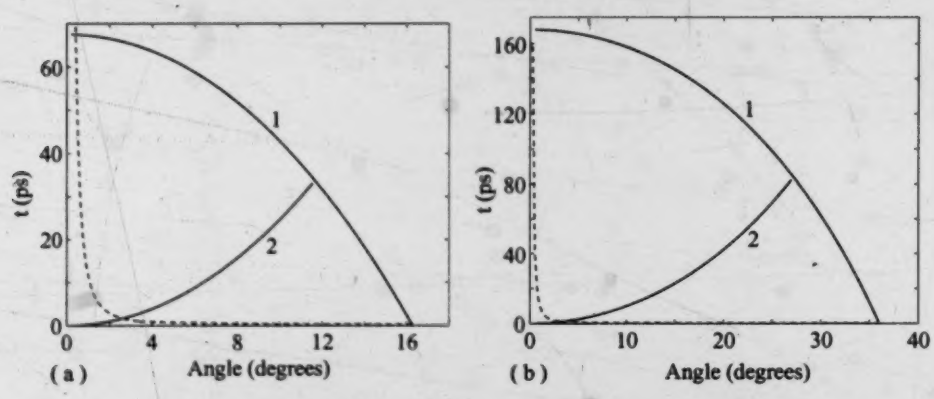

Figure 4.23: Characteristic regimes of the linear evolution of FI based on Eq. (4.34) and Eq. (4.35), shown for two sets of parameters: (a) $I = 1.7 \times 10^{15} W/cm^2$, $n_e/n_c = 0.2$, $L = 100\mu m$, (b) $I = 5 \times 10^{16} W/cm^2$, $n_e/n_c = 0.05$, $L = 100\mu m$. The dashed line define thresholds, $\sigma_i t = 1, (i = 1, 2)$. Line 1 shows the time, defined by the relation $\sigma_2(t)t = k_s L$, when the FI growth reaches maximum defined by a stationary gain. Line 2 indicates the transition time between the regimes of strong and weak coupling.

the FI grows at a rate comparable to the SBS growth rate. However it reaches the stationary regime much sooner and leads to smaller deflection angles. Also, the FI does not produce a spectral shift in the electromagnetic radiation, which has been observed in both the simulations and the experiments.

Bibliography

[1] M. R. Amin, D. E. Capjack, P. Frycz, W. Rozmus, and V. T. Tikhonchuk, Phys. Fluids B, **5** 3748 (1993).

[2] N. E. Andreev, L. M. Gorbunov, S. V. Tarakanov, and A. I. Zykov, Phys. Fluids B, **5** 1986 (1993).

[3] T. Afshar-rad, L. A. Gizzi, M. Desselberger, and O. Willi, Phys. Rev. Lett. **75**, 4413 (1995).

[4] V. V. Elisseev, W. Rozmus, V. T. Tikhonchuk, and C. E. Capjack, Phys. Plasmas **2**, 1712 (1995).

[5] V. V. Elisseev, W. Rozmus, V. T. Tikhonchuk, and C. E. Capjack, Phys. Plasmas **3**, 2215 (1996).

[6] V. V. Elisseev, W. Rozmus, V. T. Tikhonchuk, and C. E. Capjack, Phys. Plasmas **3**, 3754 (1996).

[7] S. Hüller, Ph. Mounaix, and D. Pesme, Phys. Scr. **T63**, 151 (1996).

[8] M. D. Feit, and J. A. Fleck, Jr., J. Opt. Soc. Am. A **5**, 633 (1988).

[9] C. Labaune, H. A. Baldis, E. Schifano, B. S. Bauer, A. Michard, N. Renard, W. Seka, J. D. Moody, and K. G. Estabrook, Phys. Rev. Lett. **76**, 3727 (1996).

[10] C. E. Max, Phys. Fluids **19**, 74 (1976).

[11] C. J. McKinstrie, R. Betti, R. E. Giacone, T. Kolber, and J. S. Li, Phys. Rev. E **50**, 2182 (1994).

[12] B. J. MacGowan, B. B. Afeyan, C. A. Back, R. L. Berger, G. Bonnaud, M. Casanova, B. I. Cohen, D. E. Desenne, D. F. DuBois, A. G. Dulieu, K. G. Estabrook, J. C. Fernandez, S. H. Glenzer, D. E. Hinkel, T. B. Kaiser, D. H. Kalantar, R. L. Kauffman, R. K. Kirkwood, W. L. Kruer, A. B. Langdon, B. F. Lasinski, D. S. Montgomery, B. H. Wilde, S. C. Wilks, and E. A. Williams, Phys. Plasmas **3**, 2029 (1996).

[13] H. A. Rose and D. F. DuBois, Phys. Fluids B **6**, 3337 (1993).

[14] H. A. Rose and D. F. DuBois, Phys. Plasmas **2**, 2216 (1995).

[15] M. Tabak, G. Hammer, M. Glinsky, W. L. Kruer, S. C. Wilks, J. Woodworth, E. M. Campbell, and M. D. Perry, Phys. Plasmas **1**, 1626 (1994).

[16] V. T. Tikhonchuk, and A. A. Zozulya, Phys. Fluids B, **5** 3748 (1993).

[17] S. C. Wilks, P. E. Young, G. H. Hammer, M. Tabak, and W. L. Kruer, Phys. Rev. Lett. **73**, 2994 (1994).

[18] P. E. Young, Phys. Rev. Lett. **73**, 1939 (1994).

[19] P. E. Young, J. H. Hammer, S. C. Wilks, and W. L. Kruer, Phys. Plasmas **2**, 2825 (1995).

[20] P. E. Young, M. E. Foord, J. H. Hammer, W. L. Kruer, M. Tabak, and S. C. Wilks, Phys. Rev. Lett. **75**, 1082 (1995).

[21] P. E. Young, G. Guethlein, S. C. Wilks, J. H. Hammer, W. L. Kruer, and K. G. Estabrook, Phys. Rev. Lett. **76**, 3128 (1996).

[22] P. E. Young, M. E. Foord, A. V. Maximov, and W. Rozmus, Phys. Rev. Lett. **77**, 1278 (1996).

Chapter 5

RPP beam interactions

Spatially incoherent laser beams are widely used in laser-plasma experiments because of their capability to control the light intensity distribution and to potentially suppress parametric instabilities [32, 28, 13, 1, 19, 20, 25] such as backward SBS. A technique to generate spatially incoherent laser beams is the random phase plate (RPP) [10] that breaks the incident laser light into many beamlets with random phase shifts. A RPP laser beam has large intensity fluctuations in the focal spot. The peak intensity in a laser speckle can be larger than the average beam intensity by an order of magnitude. These large intensity hot spots may have dramatic consequences for SBS, FI and their mutual interplay.

New statistical models [22, 23, 24, 18, 29, 30] have been developed to describe scattering instabilities driven by RPP pumps. These theories calculate reflectivity by averaging the independent hot spot contributions with respect to the intensity distribution function. It appears now that SBS is particularly sensitive to plasma induced changes in the hot spot distribution [30].

Several experiments have shown that a laser beam propagating in an underdense plasma develops angular spreading and spectral broadening with a shift toward longer wavelengths [17, 12, 36]. Similar plasma induced angular spreading and red shift have been observed in simulations [5, 35] describing the interaction of a coherent beam with a plasma. These results were explained in terms

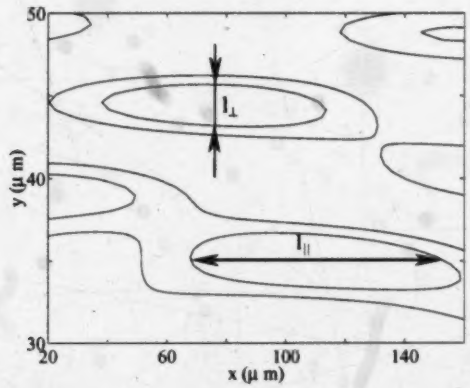

Figure 5.1: Typical contour plot of the intensity of the laser beam. Definition of the hot spot sizes.

of forward SBS and filamentation instabilities. On the other hand, numerical studies [26] with RPP laser beams have shown that both angular divergence and temporal bandwidth of the transmitted light are larger that those of the incident light in the regimes where filamentation does not reach a steady state. In this Chapter we characterize quantitatively this ability of an underdense plasma to induce a temporal incoherence together with an additional spatial incoherence to a propagating laser beam. This effect is called *plasma induced smoothing.*

The angular and spectral broadening of the laser beam can be related to spatial and temporal statistical characteristics of the laser field. In order to characterize the *spatial incoherence* of the propagating beam, we demonstrate that both the longitudinal, $l_\parallel$, and transverse, $l_\perp$, [see Fig.(5.1)] speckle sizes decrease as the beam propagates through the plasma, while the ratio $l_\parallel/l_\perp^2$ does not change significantly in space and in time. In addition, the angular width $\langle\theta\rangle$ of the transmitted light is found to satisfy the standard relation of diffraction optics, $\langle\theta\rangle \sim 1/l_\perp$. These results make it possible to define a local (in space and time) f-number of the laser beam. We also analyze the angle correlation function of the transmitted light. The plasma induced spatial incoherence is found to

result in an angle correlation function similar to the correlation function of a RPP beam characterized by the effective f-number.

The plasma induced *temporal incoherence* can be characterized by the temporal correlation function. For a random laser beam the correlation function quickly decays with the time difference of its arguments.

In addition to a quantitative characterization of the plasma induced smoothing, we also give an interpretation of its origin. Our overall picture is the following: in the regime where the average power in a speckle approaches the self-focussing threshold, nonlinear laser filaments form in the front part of the plasma. The high-intensity filaments are unstable [34, 33, 6, 21]. The instability corresponds to forward SBS growing inside the cavity formed by the density depletion associated with the filament. The temporal growth rate is characteristic of the so-called strong coupling regime [6, 21]. This instability gives rise, in the front part of the plasma, to scattered waves, temporally incoherent and characterized by a large spectral red shift and a broad angular distribution. They can then be spatially amplified during their propagation through the plasma by the forward SBS instability, in the so-called *incoherent* regime of three-wave coupling. This incoherent spatial amplification corresponds to a collective process, in the sense that it involves a spatial domain larger than the size of a single hot spot. In Fourier space, it gives rise to an increase of the angular width and of the spectral broadening while propagating further inside the plasma. In real space, it results in speckle size and correlation time both decreasing with the longitudinal coordinate. In the low intensity regime these effects result from a single scattering process only. In the case of higher laser beam intensity, the scattered waves can themselves be unstable with regard to forward SBS, leading to a multiple forward SBS process. This leads to further angular and spectral broadening of the transmitted light.

The ability of the plasma to introduce additional incoherence to a propagating laser beam has important implications concerning the growth of backscattering instabilities. We will show in Section 5.10 that additional spatial incoherence is able by itself to reduce backward instabilities, because the gain factor is smaller in the shorter speckles. In addition, it has been shown recently [3] that even a small level of temporal incoherence is able to dramatically reduce the backscatter instabilities. Namely, in contradiction with usual estimates [19, 20], it is found that a correlation time as long as a few growth times can reduce the reflectivity by several orders of magnitude.

This Chapter is organized in the following way. The importance of the optical smoothing techniques is discussed in Section 5.1. The RPP laser pump model is derived in Section 5.2. The parameters of the model used in the simulations are described in Section 5.3. In Section 5.4 the beam incoherence is quantified with spatial and temporal correlation functions. The predictions from the model are compared with the numerical results presented in Section 5.5 with a justification for the introduction of a effective beam f-number. The beam angular spreading is illustrated in Section 5.6. The statistical properties of the propagating beam are discussed in Section 5.7. A theoretical model for single forward Brillouin scattering from a spatially incoherent beam is developed in Section 5.8. In Section 5.9 the simulation results for the spectral shift of the transmitted light are presented. The reduction of backward SBS is explained by the decrease of the effective speckle length in Section 5.10.

5.1 Optical smoothing techniques

Direct target irradiation with short-wavelength lasers leads to good energy coupling and high-ablation pressure with small hot-electron preheat. However, the major potential problem in this approach is the irradiation nonuniformity which

leads to implosion nonuniformity, because of the small lateral-smoothing effects. Efforts to achieve uniform illumination have been frustrated by imperfections in the laser systems. The cumulative effect of small phase abberations introduced by each optical element of a multistage laser produces large random intensity non-uniformities. These illumination non-uniformities can be divided into two categories:

- large scale non-uniformities – encompass the entire intensity profile of the incident laser beam;
- small scale non-uniformities – involves the detailed structure of the beam [cf.Fig.(2.7)].

While the large scale nonuniformity can probably be controlled to within tolerable limits, the non-uniformities from the second group seed the filamentation instability. Intensity hot spots caused by filamentation can seriously degrade laser-plasma coupling and can produce conditions favorable for other instabilities.

To avoid seeding instabilities by the small scale non-uniformities of the laser beams, as well as to get some control over the overall laser beam profile, different optical smoothing techniques have been developed. One of the most popular is the *random phase plate* technique *. RPP breaks up the incident laser light into many small beamlets by means of transmitting areas each one applying a phase shift randomly chosen between 0 and π. The beamlets are then focussed onto the target and the intensity distribution comprises a very large number of closely spaced spikes, arising from the interference between the different beamlets.

*The other two techniques, induced spatial incoherence (ISI) and smoothing by spatial diffraction (SSD) require the use of finite bandwidth laser light. The ISI method [14, 15, 2, 8] uses a transparent echelon that introduces a different time delay into the produced beamlets and renders them mutually incoherent. The SSD method [27] spatially disperses broadband light onto a phase plate so that each element of the RPP is irradiated by a different frequency.

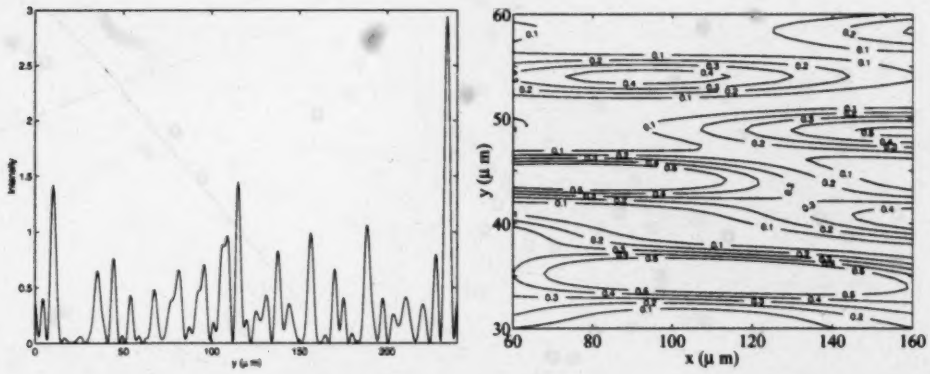

Figure 5.2: Typical intensity cross section at best focus position,(a), and intensity contour plot of part of the computational box,(b), at $T = 0ps$. Parameters of the run are $f_{\#} = 4$, $I_0 = 0.85 \times 10^{15} W/cm^2$, $n_e/n_c = 0.1$.

Figure (5.2)(a) shows the cross section of the beam intensity at the best focus position and Fig.(5.2)(b) – the corresponding contour plot at time $T = 0$. The RPP intensity pattern in the focal plane consists of a diffraction-limited envelope of a rapidly varying structure caused by the interference between rays from different phase-plate elements. As an example, consider the interference between two rays with lengths L_1 and L_2, respectively, from a RPP in the focal plane. In the target plane their combined electric fields are

$$E = E_1 e^{i(kL_1+\phi_1-\omega t)} + E_2 e^{i(kL_2+\phi_2-\omega t)}$$

where the amplitudes are diffraction limited, i.e. $E_1 \sim E_2 \sim \sin y/y$ and the phases ϕ_1 and ϕ_2 include those imposed by the RPP. Then the intensity profile at the focal plane

$$I = |E|^2 = 2E_1^2 \left(1 + \cos\left[k(L_1 - L_2) + (\phi_1 - \phi_2)\right]\right)$$

consists of high-intensity fluctuations in the transverse direction as the path length $(L_1 - L_2)$ changes.

5.2 RPP pump model

A model for the electric field of a RPP beam is an important part of the numerical simulation. For this purpose we solve the Maxwell's equations for the free light propagation in homogeneous plasma, neglecting at this step the plasma response to the field. The derivation of the model for the incoherent pump which we have adopted is based on the paraxial optic wave equation that is obtained from Eq. (2.88) by using the dispersion relation for the light propagation:

$$\left(\partial_z - \frac{i}{2k_0}\nabla_\perp^2\right) E = 0.$$

In order to describe the free light propagation, we derive the near field pattern for a RPP beam by using it's far field profile. Denoting the size of RPP plate by D, one introduces N random elements of size $d = D/N$ located at

$$y_j = \alpha_j D/2,$$

where

$$\alpha_j = -1 + \frac{1}{N} + \frac{2(j-1)}{N}, \qquad j = 1, \cdots, N$$

varies in the range of

$$\alpha_j \in [-1 + 1/N, 1 - 1/N].$$

We use the dimensionless units

$$x = \hat{x} l_R, \tag{5.1}$$

$$y = \hat{y} a_0, \tag{5.2}$$

where $a_0 = f\alpha_0$, $l_R = k_0\alpha_0^2$, and $f = F/D$. In these units the lens is located at $x_0 = -F/l_R \equiv -\hat{F}$ [see Fig.(5.3)] and the position of a j-th RPP element is expressed as $\hat{y}_j = \alpha_j \hat{D}/2 \equiv \alpha_j (D/a_0)/2$. Both $\hat{F}$ and $\hat{D}$ are large numbers $\gg 1$ and one has $\hat{D}/\hat{F} = 2\pi$.

The starting point is the desired shape of the far field at the lens:

$$E_0(y) \equiv E(y, x = x_0 = -F) = E_0 \exp i\phi_{x_0}(y) \sum_{j=1}^{N} e^{i\varphi_j} S\left(\frac{y - y_j}{d}\right), \qquad (5.3)$$

where φ_j is the phase for the j-th element randomly chosen between 0 and π; S is the echelon function

$$S(y) = \begin{cases} 0, & for \quad y/d < -1/2, \\ 1, & for \quad -1/2 < y/d < 1/2, \\ 0, & for \quad y/d > 1/2. \end{cases}$$

The phase $\phi_{x_0}(y)$ is such that

$$k_\perp(y) = \frac{\partial \phi_{x_0}}{\partial y}.$$

and corresponds to a ray converging at the focal point $x = 0$. From the geometrical relations $k_\perp/k_0 = -y/F = y/x_0$, we can obtain an expression for the phase as follows

$$\phi_{x_0}(y) = \int_0^y k_\perp(y)dy = \frac{y^2}{2x_0}.$$

By defining the electric field, E_0 via the incident power $P_{inc} = E_0^2 D$, the expression for the far field, Eq. (5.3), reads

$$E(\hat{y}, \hat{x} = \hat{x}_0 = -\hat{F}) = \sqrt{\frac{-P_{inc}}{D}} \exp i\frac{\hat{y}^2}{2\hat{x}_0} \sum_{j=1}^{N} e^{i\varphi_j} S\left(\frac{y - y_j}{d}\right). \qquad (5.4)$$

The solution for the near field close to the focal plane is given by

$$\hat{E}(\hat{y}, \hat{x}) = \int d\hat{y}_0 G(\hat{y} - \hat{y}_0, \hat{x} - \hat{x}_0) E(\hat{y}_0, \hat{x}_0 = -\hat{F}), \qquad (5.5)$$

where the Green function is given by

$$G(\hat{y} - \hat{y}_0, \hat{x} - \hat{x}_0) = \frac{1}{\sqrt{2i\pi(\hat{x} - \hat{x}_0)}} \exp i\frac{(\hat{y} - \hat{y}_0)^2}{2(\hat{x} - \hat{x}_0)}. \qquad (5.6)$$

So the general expression for the near field is given by

$$E(\hat{y}, \hat{x}) = \sqrt{\frac{-P_{inc}}{D}} \frac{\hat{D}/2\pi}{\sqrt{2i\pi\hat{F}}} \sum_{j=1}^{N} e^{i\varphi_j} \exp\left\{-i\theta_j\left(\hat{y} + \frac{\theta_j \hat{x}}{2}\right)\right\} F_N(\hat{y} + \hat{\theta}_j \hat{x}, \hat{x}), \quad (5.7)$$

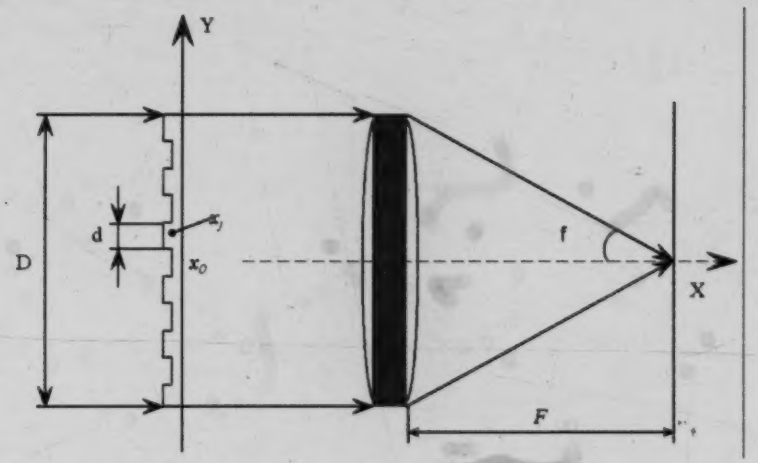

Figure 5.3: Random phase plate configuration.

where

$$F_N(\hat{\xi},\hat{x}) = \int_{-\pi/N}^{\pi/N} d\theta \exp(i\theta\hat{\xi}) \exp -i\frac{\theta^2\hat{x}}{2}. \tag{5.8}$$

Here we defined θ as the ratio

$$\theta_j = -\hat{y}/\hat{x}_0. \tag{5.9}$$

Note that $\theta_j = \alpha_j\pi = \tan\varphi$ has a meaning of a perpendicular k-vector and varies from $-\pi$ to π. In the focal plane, i.e. when $\hat{x} \to 0$ the function $F_N(\hat{\xi},\hat{x})$ reduces to

$$F_N(\hat{\xi},\hat{x}) = \frac{1}{\xi}\sin\frac{\pi\hat{\xi}}{N} \tag{5.10}$$

and the final expression for the field near the focal plane is:

$$E(\hat{y},\hat{x}) = \sqrt{\frac{P_{inc}}{ia_0}}\frac{1}{2\pi}\sum_{j=1}^{N} e^{i\varphi_j} \exp\left\{-i\theta_j\left(y + \frac{\theta_j}{2}x\right)\right\}\frac{2}{\xi_j}\sin\left(\frac{\pi\xi_j}{N}\right), \tag{5.11}$$

with

$$\xi_j = \hat{y} + \theta_j\hat{x}.$$

5.3 Parameters of the model

The system of Eq. (2.88) and Eq. (2.91) was solved numerically for plasma parameters close to experimental conditions. The assumed size of the plasma is 160 laser vacuum wavelengths ($\lambda_0 = 1\,\mu$m) in the longitudinal (x) direction, and 240 λ_0 in the transverse (y) direction. The electron temperature is $T_e = 1$ keV and density $n_e = 0.1 n_c$. The ratio $\Gamma_s = \gamma_s/\omega_s$ of the damping rate γ_s to the angular frequency ω_s for the ion acoustic waves generated by the backward SBS is set to 0.55 in order to maintain the backward SBS reflectivity at experimentally observed levels. The standard *top-hat* model [25] is used for the angular spectrum of the incident RPP beam:

$$|E(k_y)|^2 = \begin{cases} const, & if \quad |k_y| \le k_m \\ 0, & if \quad |k_y| > k_m. \end{cases}$$

The f-number of an incident beam is defined as

$$f_0 = \frac{1}{2}\sqrt{k_0^2/k_m^2 - 1},$$

where $k_0 = 2\pi/\lambda_0$ (in the simulations $f_0 = 4$).

Numerical simulations have shown a non-stationary behavior of the electric field intensity distribution and of the plasma density perturbations at simulation times up to 150 ps. Density channels created by unsteady filaments are found to coexist with the ion acoustic waves generated by broad-angle forward and backward SBS.

The onset of ponderomotive self-focussing in a three-dimensional (3D) laser speckle is controlled by the *self-focussing parameter* p_{3D} which is equal to the ratio of the beam power contained in a speckle to the critical power for self-focussing [22, 16]:

$$p_{3D} = \frac{\pi}{2N_c}\frac{n_e}{n_c\lambda_0^2}\int dS_\perp I,$$

where $N_c = 1.86$, $I = |E|^2/4\pi n_c T_e$, and the integration is performed over the speckle transverse profile. A waist a_{3D} of a 3D speckle can be defined by the

formula:

$$a_{3D}^2 = \frac{1}{\pi I_m} \int dS_\perp I,$$

where I_m is the peak speckle intensity. The choice of the constant in the definition of a_{3D} leads to $a_{3D} = a_G$ for a Gaussian speckle, where a_G is a characteristic width of the transverse intensity distribution, $I = I_m \exp(-r_\perp^2/a_G^2)$. By using the speckle waist definition, one can rewrite the self-focussing parameter p_{3D} in the form:

$$p_{3D} = \frac{1}{2N_c} a_{3D}^2 k_{opt}^2, \tag{5.12}$$

where

$$k_{opt} = \frac{\pi}{\lambda_0} \sqrt{I_m n_e/n_c},$$

is the transverse wavenumber, which maximizes the growth rate of filamentation instability [cf. e.g. [11]]. Therefore, the self-focussing parameter p_{3D} is determined by the ratio of the speckle waist to the wavelength optimal for the growth of linear filamentation instability. In the case of a 3D cylindrical speckle produced by a top-hat RPP beam one obtains

$$a_{3D}^2 = \frac{4}{\pi^2} f^2 \lambda_0^2,$$

and consequently the self-focussing parameter p_{3D} is given by

$$p_{3D} = 1.07 I_m f^2 n_e/n_c.$$

In a two dimensional geometry there is no threshold power for the existence of a stationary localized solution for a laser filament [31]. Such a solution takes the form

$$I_{2D} = I_m/\cosh(y/a_T),$$

and is localized on a characteristic scale $a_T = \sqrt{2}/k_{opt}$. Similarly to the case of a 3D speckle, one can define the waist of a 2D speckle (with 1D transverse

direction) as

$$a_{2D} = \frac{1}{2I_m} \int dy I.$$

In the case of the nonlinear stationary solution I_{2D} this definition of the speckle waist leads to $a_{2D} = a_T$. We have found that the following parameter, p_{2D}, which is defined in a way similar to p_{3D} in Eq. (5.12), characterizes the onset of self-focussing instability in a 2D RPP beam,

$$p_{2D} = \frac{1}{2} a_{2D}^2 k_{opt}^2. \tag{5.13}$$

For the case of the stationary nonlinear localized solution I_{2D} this parameter p_{2D} is equal to 1. In the case of a speckle produced by a top-hat RPP corresponding to our 2D simulations, one has

$$a_{2D} = f\lambda_0/2,$$

and consequently the self-focussing parameter is given by

$$p_{2D} = 1.23 I_m f^2 \frac{n_e}{n_c}.$$

The average intensity of the incident beam q has been varied in our simulations in the range of $(0.2 - 1) \times 10^{15}$ W/cm^2. Thus, the self-focussing parameter $\langle p_{2D} \rangle$ corresponding to an *average speckle* was varied in the range $(0.16 - 0.8)$. Here "average speckle" means a speckle characterized by a peak intensity I_m equal to the average beam intensity $\langle I \rangle$. Naturally in the RPP beam there are a large number of hot spots with peak intensities larger than $\langle I \rangle$ [cf. Fig.(5.2)], so that the self-focussing parameter p_{2D} for these hot spots could be larger than one.

5.4 Spatial and temporal incoherence

To clarify the concept of temporal coherence consider electric field with a finite bandwidth $\Delta\nu$. For a finite time interval τ we expect the complex envelope

$\mathbf{E}(\mathbf{x},t)$ to remain relatively constant provided $\tau \ll 1/\Delta\nu$. In other words the function $\mathbf{E}(\mathbf{x},t)$ and $\mathbf{E}(\mathbf{x},t+\tau)$ are highly correlated, i.e. *coherent* if τ is much less that the *coherence time* $\tau_c = 1/\Delta\nu$. But because every real light source has a finite bandwidth, for sufficiently large time delay τ the functions $\mathbf{E}(\mathbf{x},t)$ and $\mathbf{E}(\mathbf{x},t+\tau)$ become decorrelated. Similarly considering the spatial coherence, we can start with two electric fields $\mathbf{E}(\mathbf{x}_1,t)$ and $\mathbf{E}(\mathbf{x}_2,t)$ without time delays. When the two points coincide, $\mathbf{x}_1 = \mathbf{x}_2$), the two wavefronts are perfectly correlated, but moving the points $\mathbf{x}_1$ and $\mathbf{x}_2$) apart, some loss of correlation can be expected.

In spectral representation, two fields exhibit temporal incoherence if their wave vectors have the same direction but different length. The fields are spatially incoherent if the length of their wave vectors is the same, but the direction is different.

In order to characterize the *spatial incoherence* of a propagating beam, we have calculated the angle correlation function:

$$C_T(\theta,\Delta\theta) = 1 - \frac{\overline{|E_\theta E^*_{\theta-\Delta\theta}|}}{[\overline{|E_\theta|^2}]^{1/2}\,[\overline{|E_{\theta-\Delta\theta}|^2}]^{1/2}}, \tag{5.14}$$

where E_θ is the amplitude of transmitted light electric field propagating at an angle θ with regard to the incident beam direction. The angle correlation function (5.14) plotted in Fig. 5.4 shows that the transmitted light has a correlation angle θ_c of a few degrees. Thus, plasma induced smoothing results in a weak correlation of the light propagating in different directions, both inside and outside the incident beam convergence angle. In particular, the light scattered outside the focussing cone is weakly correlated in angle with the incident light. This weak correlation between the Fourier components corresponding to different propagation directions, together with the Gaussian nature of its statistics, confirm that the transmitted beam behaves as a generic RPP beam with an effective f-number.

In order to characterize the *temporal incoherence* of the propagating beam,

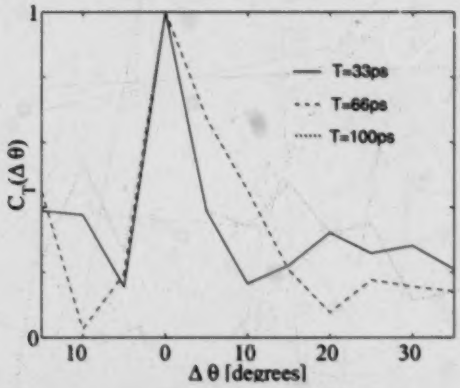

Figure 5.4: Angle correlation function of the transmitted light propagating at angle $\theta = 10°$ for three time intervals with the interval center at $T = 33$ ps (solid line), 66 ps (dashed line), 100 ps (dotted line); the averaging time interval $\Delta t = 27$ ps, the average beam intensity 0.7×10^{15} W/cm^2.

we have calculated the time correlation function of the electric field amplitude at the rear boundary of the plasma:

$$C_{T,\theta}(\tau) = \frac{\int dt E_\theta(t-\tau/2)E_\theta^*(t+\tau/2)}{\int dt E_\theta(t)E_\theta^*(t)}, \tag{5.15}$$

where the integrals are taken over the time interval $[T - \Delta t/2, T + \Delta t/2]$. Time correlation functions (5.15) are shown in Fig. 5.5 for three different time periods. They decay with time τ, indicating that $E(t)$ is an incoherent process. The correlation time, τ_c, defined as half width half maximum of the correlation function absolute value, decreases with T, and is comparable to the inverse of the transmitted light temporal bandwidth, $\tau_c \sim \Delta\omega^{-1}$. It is found that the correlation time depends on the propagation angle. It is much smaller for large angles, outside the incident beam convergence angle, than within it [cf. Figs. 5.5(a),(b)]. We attribute this result to multiple stimulated forward Brillouin scattering. In particular, at late time ~ 100 ps the temporal bandwidth of the light transmitted outside the incident beam cone reaches values on the order of $k_0 c_s$, which is consistent with the correlation time $\tau_c \sim 1/(k_0 c_s) \approx 0.6ps$ [cf. Fig. 5.5(a)]. The

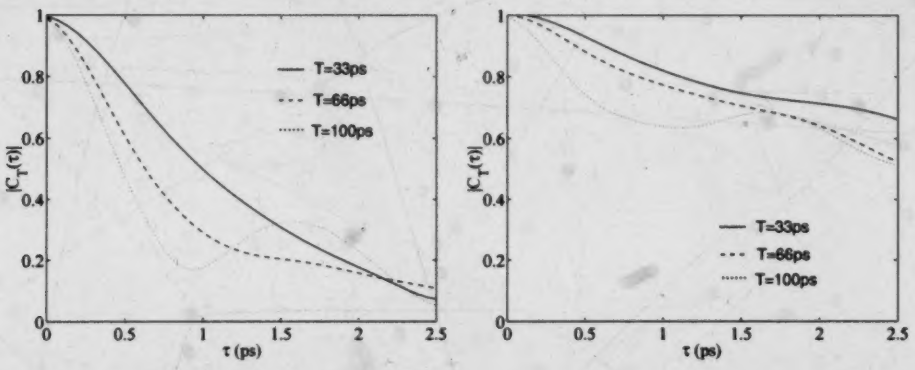

Figure 5.5: Time correlation function of the transmitted light propagating at angle $\theta = 10°$ (a) and angle $\theta = 0°$ (b) for three time intervals with the interval center at $T = 33$ ps (solid line), 66 ps (dashed line), and 100 ps (dotted line); the averaging time interval $\Delta t = 27$ ps, the average beam intensity 0.7×10^{15} W/cm^2.

correlation time is in good agreement with the theoretical predictions derived in the next section, namely $\tau_c \sim f_L/k_0 c_s$, where f_L is the effective f-number for the transmitted light.

5.5 Laser beam effective f-number

To explain the changes of the beam structure as reflected in the evolution of its parameters we introduce the following definition of an effective laser beam f-number assuming that corrections $\sim 1/4f^2 \ll 1$ can be neglected. According to [22], the hot spot longitudinal size, $l_\parallel \sim f^2$, and the transverse size, $l_\perp \sim f$. The proportionality factors depend on the transverse profile of the speckle and on the spatial dimensionality of the model. We have calculated the average transverse, $\langle l_\perp \rangle$, and longitudinal, $\langle l_\parallel \rangle$, hot spot size as functions of time and introduced two time-dependent effective f-number, namely,

$$f_\parallel(t) = f_0 \sqrt{\langle l_\parallel \rangle(t)/\langle l_\parallel \rangle(0)}, \tag{5.16}$$

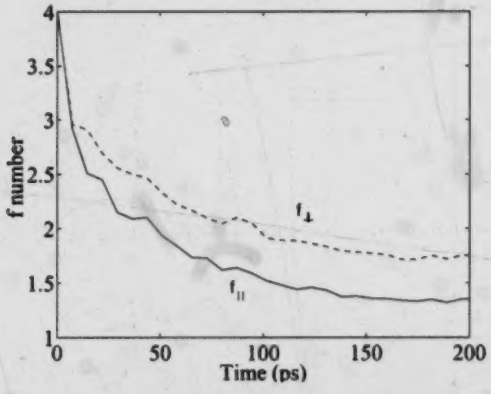

Figure 5.6: Variation of the laser RPP beam effective beam f-numbers $f_\perp$ (dashed line) and $f_\parallel$(solid line) in time for the average beam intensity 0.7×10^{15} W/cm^2.

and

$$f_\perp(t) = f_0\langle l_\perp\rangle(t)/\langle l_\perp\rangle(0). \tag{5.17}$$

The averaging has been performed over the hot spot ensemble obtained in the numerical simulations. A contour plot of the field intensity in a part of the simulation region is shown in Fig. (5.2)(a). The hot spots have been identified as well-separated local maxima of the field intensity in a plasma volume.

The temporal dependence of the effective f-number (calculated for the rear half part of the simulation region) is presented in Fig. (5.6). The two effective f-number have similar values and both decrease in time. The effective f-number calculated from the average longitudinal hot spot size, $f_\parallel$, is up to 30% smaller than the f-number calculated from the average transverse hot spot size, $f_\perp$. This difference is due to the change of hot spot orientation in space caused by plasma smoothing. It can indeed be seen on Fig. (5.7) that many hot spots are oriented not exactly along the direction of beam propagation (the x-direction), but at an angle up to 15° that is consistent with the beam angular spreading. For such a hot spot ensemble, the average hot spot size in the x-direction is smaller than

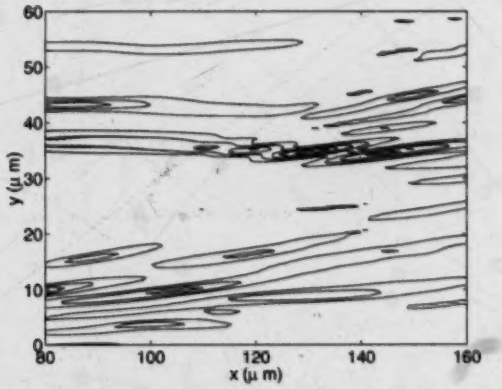

Figure 5.7: The distribution of laser field intensity at time 50 ps for the average beam intensity 0.6×10^{15} W/cm^2.

the average hot spot size in the direction of its orientation. After accounting for the change in hot spot orientation one can conclude from Fig. (5.6) that the hot spots preserve their shape while their size decreases. Therefore, it is possible to characterize the light beam structure in the plasma by one parameter only, that we choose to be $f = f_\perp$, because it is less affected than $f_\parallel$ by the hot spot orientation. Inside the plasma the effective f-number changes gradually from $f = f_0$ at the entrance boundary to $f = f_L$ at the rear boundary.

Together with the effective f-number, the hot spot volume, $\sim f^{D+1}$, decreases with time, so that the number of hot spots per unit volume, $\sim 1/f^{D+1}$, is expected to increase with time (here d denotes the spatial dimensionality). We have checked this result numerically.

5.6 Beam angular spreading

In the case of a linear propagation of a RPP beam, the angular width of the transmitted light is inversely proportional to the f-number of the beam $\langle\theta\rangle \sim 1/f_L$. We have checked numerically that this property still holds when the transmitted

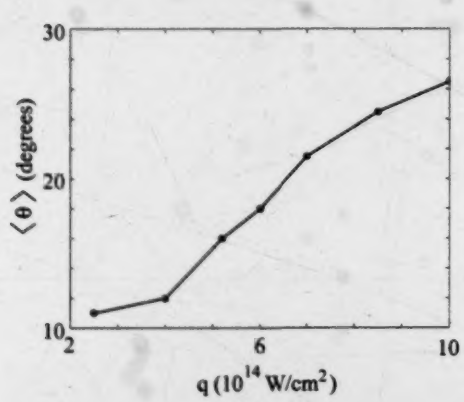

Figure 5.8: Dependence of the angular width of the transmitted light $< \theta >$ at time $T = 70ps$ on the average intensity of the incident beam.

beam is smoothed due to its nonlinear propagation in the plasma. The angular spreading has been negligible for intensities smaller than 0.4×10^{15} W/cm^2 (corresponding to an average self-focussing parameter $\langle p_{2D} \rangle < 0.32$), and, accordingly, the f-number has not changed in time. For larger beam intensities, the angular beam spreading increases with intensity [cf. Fig. (5.8)], the length of the plasma, and time. At our maximum intensity, which corresponds to $\langle p_{2D} \rangle = 0.8$, the angular width of the transmitted light increased by a factor of 2.5 at time $\sim$ 70 ps and continued to increase during the entire simulation time [†].

A typical temporal evolution of the intensity of transmitted and reflected light is shown in Fig.(5.9). The series of time snapshots shows a large angular spreading of the transmitted light and a virtual dissapearance of the reflected part. Fig. (5.10) summarizes these results for the duration of the simulation. Fig. (5.10) (a) shows an almost linear increase of the angular width, $\langle \theta \rangle$, of

[†]The angular spreading and the frequency shift of a RPP beam in 2D numerical simulations has been reported in Ref. [26] within a paraxial model of light propagation. The explored range of the self-focussing parameter there was close to ours, but the angular width of the incident beam was much smaller. Different from the paraxial simulations of Ref. [26], we have modeled the large angular spreading of a RPP beam up to angles of 30 – 40 degrees off the incident beam direction, where the validity of paraxial approximation becomes questionable.

the transmitted light. The angular width $\langle\theta\rangle$ is defined as the full width of the central part of the spectrum that contains 76% of the electromagnetic energy. It is equal to the full width half maximum for a Gaussian distribution. The power reflected by the plasma due to backward SBS (solid line in Fig. (5.10)(b)) at first increases with time, reaches its maximum at time $\sim 10 - 20$ ps, and then gradually decreases. One additional parameter is extracted from the data and is shown in (Fig. (5.10)(b)), namely the intensity of the transmitted light within the initial beam cone (dotted line in Fig. (5.10)(b)). As we see, it decreases with time.

5.7 Hot spot statistics

Another important characteristic of a spatially incoherent laser beam is the distribution function of the peak intensities in hot spots. This function plays a fundamental role in theoretical predictions concerning self-focussing and SBS [22, 23, 24]. The number of hot spots with peak intensities above a given intensity I per unit volume is described by the *abundance function*, $M(I)$. For Gaussian statistics of hot spots, the abundance function has the form [7]:

$$M_G = N\lambda_0^{-D} f^{-D-1} u^{D/2} \exp(-u), \tag{5.18}$$

where

$$u = I/\langle I\rangle \gg 1, \tag{5.19}$$

and N is a numerical factor. In Fig. (5.11) we plot the abundance function $M(I)$ normalized to $M(2\langle I\rangle)$. Fig. (5.11) shows that the abundance function from numerical simulations, $M(I)/M(2\langle I\rangle)$ (solid line), which can be well fitted by the corresponding Gaussian prediction $M_G(I)/M_G(2\langle I\rangle)$ (dotted line). Thus, the transmitted light, smoothed during its nonlinear propagation through the plasma, can be characterized by the same Gaussian statistics as a generic RPP

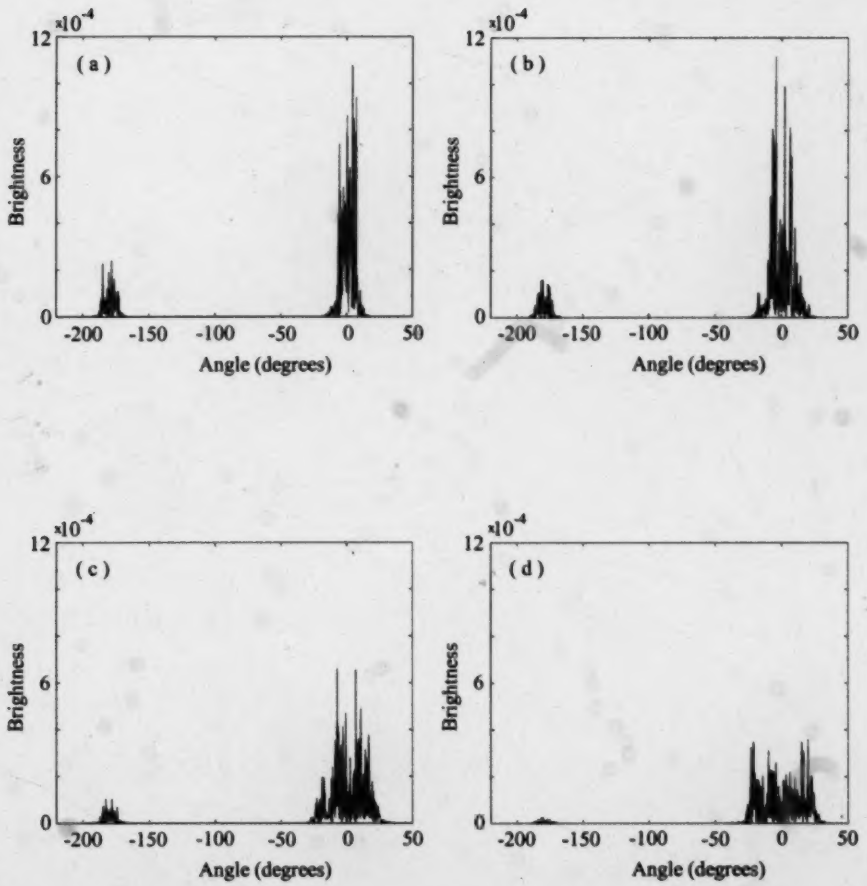

Figure 5.9: Typical evolution of beam spreading in different moments of time: (a) 14ps, (b) 58ps, (c)116, (c) 211ps. The average beam intensity is 0.7×10^{15} W/cm^2.

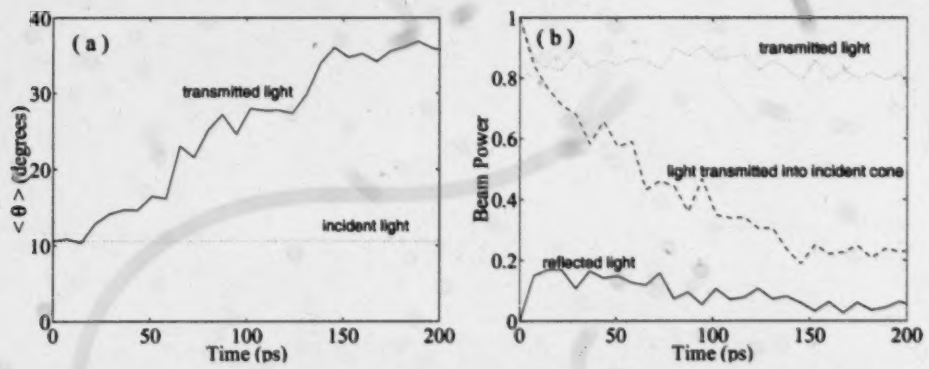

Figure 5.10: Variation of the laser RPP beam parameters in time for the average beam intensity 0.7×10^{15} W/cm^2: (a) angular width of the transmitted light; (b) fraction of the incident beam power: transmitted (dashed line), transmitted into incident beam convergence angle (dotted line), and reflected (solid line);

beam with the effective f-number. Our interpretation of this result is the following. At the initial stage (taking about $20-30$ ps) filaments form in the front part of the plasma, due to trapping of high intensity laser light in density channels. Filaments become unstable and evolve into non-stationary, smaller size filamentary structures, which are the result of coupling between self-focussing and forward SBS instabilities [21, 6]. These non-stationary structures consequently emit scattered waves in a temporally incoherent way. The plasma induced laser beam incoherence results in the random distribution of hot spots obeying Gaussian statistics with reduced f-number and additional temporal incoherence.

5.8 Random Phase Approximation

In order to compute the forward SBS gain corresponding to a collective process, we use the standard Random Phase Approximation (RPA) technique [19, 20], because the Fourier components of the electric field in the propagating beam are weakly correlated, i.e. the correlation angle θ_c is much smaller than the incident beam convergence angle $2\theta_{inc}$ as seen in our simulations in Fig. 5.4. Contrary

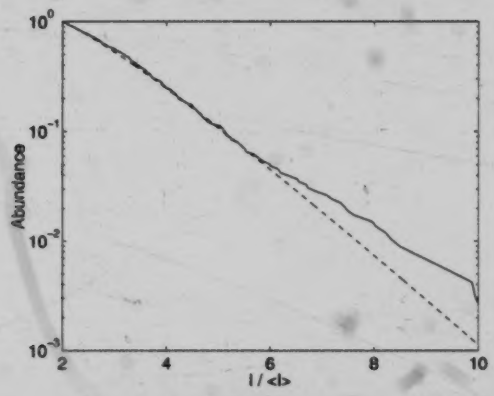

Figure 5.11: Normalized abundance of hot spots $M(I)/M(2\langle I\rangle)$ versus hot spot maximum intensity for the average beam intensity 0.7×10^{15} W/cm^2 at time 70 ps in the simulations (solid line) compared to the theoretical formula for the Gaussian speckle statistics $M_G(I)$ (dashed line).

to backward SBS, the forward SBS involves growth in several independent hot spots.

For our parameters $2\theta_{inc} \approx 15°$ while $\theta_c \approx 5°$. The correlation time of the light propagating within the incident beam cone is much larger than for scattered light [cf. Figs. 5.5(a),(b)]. Therefore the incident field amplitude can be considered as stationary.

We derive the RPA formula for the forward SBS growth rate in the limit of a *single* scattering process. In the linear regime of forward SBS, the field amplitude E can be represented as a sum of an incident field amplitude, E_0, and of a small perturbation, E_1. Linearizing Eqs. (2.88), (2.91) and Fourier transforming in the transverse (y) direction, one obtains the following equations for the Fourier components of the scattered wave $E_1(\omega, k_y)$ and the ion acoustic wave $N(\omega, k_y)$:

$$\left(2ik_0\sqrt{1-n_e/n_c}\frac{\partial}{\partial x} - k_y^2\right) E_1(\omega, k_y) = \frac{\omega_0^2}{c^2}\frac{n_e}{n_c}\int dk_y' \, N(\omega, k_y')E_0(k_y - k_y'), \quad (5.20)$$

$$\left(\omega^2 - 2i\omega\gamma_s - c_s^2k_y^2\right) N(\omega, k_y) = \frac{c_s^2k_y^2}{16\pi n_c T_e}\int dk_y' \, E_1(\omega, k_y')E_0^*(k_y' - k_y) \quad (5.21)$$

Equation (5.20) is written within the paraxial approximation, and the term with a small longitudinal component of the ion acoustic wave vector ($\sim k_x^2$) is neglected in Eq. (5.21). Following the RPA technique, the ensemble average of the pump field amplitude product $E_0(k_1)E_0^*(k_2)$ is approximated by a δ-function :

$$\langle E_0(k_1)E_0^*(k_2)\rangle = |E_0(k_1)|^2 k_0\theta_c\delta(k_1 - k_2).$$

By proceeding this way, one obtains the following equation for the intensity of the scattered wave Fourier component $|E_1(\omega, k_y)|^2$:

$$\frac{\partial|E_1(\omega,k_y)|^2}{\partial x} = |E_1(\omega,k_y)|^2\frac{\omega_0^2}{c^2}\frac{n_e}{n_c\sqrt{1-n_e/n_c}}\theta_c J(\omega,k_y)\,, \qquad (5.22)$$

where

$$J(\omega,k_y) = \int dk'\frac{|E_0(k')|^2}{16\pi n_c T_e}\mathrm{Im}\frac{(k_y-k')^2c_s^2}{(k_y-k')^2c_s^2-\omega^2-2i\gamma_s(k_y-k')\omega}\,, \qquad (5.23)$$

and $\gamma_s(k)$ is the ion acoustic damping rate for the forward SBS ($\gamma_s(k) = 0.08|k|c_s$ in our simulations). The integration in Eq. (5.22) has to be performed with respect to the transverse components of the wave vectors. The pump beam intensity spectrum can be approximated by the usual "top-hat" form:

$$|E_0(k)|^2 = \begin{cases} \langle|E_0|^2\rangle/2k_0^2\theta_c\theta_{inc}\,, & if \quad |k| \le k_0\theta_{inc}, \\ 0\,, & if \quad |k| > k_0\theta_{inc}. \end{cases}$$

Equation (5.22) describes the convective amplification of the scattered wave along the direction of the incident beam propagation: $|E_1(\omega,k_y)|^2 \sim \exp(G_f)$. The forward SBS gain factor G_f corresponding to amplification over the length L reads:

$$G_f = L\frac{\omega_0^2}{c^2}\frac{n_e}{n_c\sqrt{1-n_e/n_c}}\theta_c\, J(\omega,k_y). \qquad (5.24)$$

There are two reasons for the angular spread of the scattered light: the natural width of the ion acoustic resonance and the angular spread of the pump field.

The latter dominates, if $2k_0\theta_{inc} \gg \gamma_s(k)/c_s$. In this limit, the forward SBS gain factor in Eq. (5.24) can be estimated as follows

$$G_f = \frac{\pi}{2} L \frac{n_e}{n_c\sqrt{1-n_e/n_c}} \frac{\omega}{2\theta_{inc}c_s} \frac{\langle |E_0|^2 \rangle}{16\pi n_c T_e}, \tag{5.25}$$

where the frequency shift, ω, belongs to the interval

$$\omega \in [k_y c_s - k_0\theta_{inc}c_s, k_y c_s + k_0\theta_{inc}c_s].$$

The maximum of the gain corresponds to the maximum of the frequency shift, hence the angular spreading increases the red shift of the transmitted light. Result (5.25) corresponds exactly to the well-known RPA result, namely

$$G_f = 2\pi\gamma_0{}^2\tau_c L/v_c,$$

in which

$$v_c = c\sqrt{1-n_e/n_c},$$

and the correlation time τ_c is given in terms of the sound wave temporal bandwidth $\Delta\omega_s$ by $\tau_c = 1/\Delta\omega_s$, with $\Delta\omega_s = k_0 c_s/f_0$.

In order to check the validity of this single forward SBS description, we have computed the average frequency shift

$$\langle\omega\rangle(\theta) = \frac{\int d\omega\, \omega\, |E_1(\omega, k_y)|^2}{\int d\omega\, |E_1(\omega, k_y)|^2},$$

of the transmitted light with $k_y = k_0 \sin\theta$, in which the intensity of the scattered light $|E_1(\omega, k_y)|^2$ was obtained numerically using Eq. (5.24). The results are compared with the frequency shift from the simulations at time up to 70 ps [see Fig. 5.14]. For scattering angles smaller than 10°, the linear ion acoustic frequency $\omega_l(\theta)$ is small compared to the red shift $\Delta\omega_s$, so that the average frequency $\langle\omega\rangle$ does not depend much on the angle θ. On the other hand, for scattering angles smaller than 10°, the transmitted light involves contributions

from both the incident pump intensity and the scattered radiation, so that the comparison with the analytical result (5.24) involving only the scattered light should not be made in this range of angles. We shall therefore consider only angles larger than 10° in the discussion that follows.

5.9 Spectral shift of the transmitted light

The transmitted light frequency spectra in our simulations are broadened and red shifted, as observed in the experiments [17, 12, 36] and previous numerical results [5, 26]. Figures (5.12),(5.13) shows an example of frequency spectrum of the transmitted light for the average laser intensity 0.7×10^{15} W/cm^2, and $f_0 = 4$ RPP beam, corresponding to $\langle p_{2D} \rangle = 0.56$. All light propagating in the forward direction has been collected and contributes to Fig. (5.12)(a). The increasing width and red shift of the spectrum are consistent with the angular broadening of the transmitted light described before [cf. Fig. (5.10)(b)]. At early times, up to $20 - 30$ ps, the unshifted component in the frequency spectrum [cf. Figs. (5.12)(a),(b)] is dominant. During this time, the spectral width is about $0.25 k_0 c_s$. It corresponds to the transient plasma response to the initial RPP beam, when the plasma density fluctuations build up due to the ponderomotive force. After this initial period of time, the high intensity hot spots form nonlinear filaments which subsequently undergo the filament instability. It results in the formation of dynamical filamentary structures accompanied by the generation of a broad spectrum of ion acoustic and scattered electromagnetic waves.

From the frequency spectra of transmitted light we have obtained the dependence of the frequency red shift on the propagation angle, $\omega(\theta)$. For an average beam intensity below 0.6×10^{15} W/cm^2, the frequency shift is in good agreement with the forward SBS in the weak coupling regime. In this regime the frequency

shift $\omega(\theta)$ is given by the three-wave resonance condition,

$$\omega_l(\theta) = 2k_0 c_s \sin(|\theta|/2)\sqrt{1 - n_e/n_c}.$$

For larger incident beam intensity, the frequency shift of the light scattered outside the focussing cone is up to 1.5 times larger than the weak coupling prediction $\omega_l(\theta)$ (see Fig. (5.14)). This feature of the frequency spectra is also experimentally observed [17].

The forward SBS from a single hot spot cannot explain these results. Indeed, in the transient regime of SBS growth, $t \leq \lambda_0 f/c_s$, the gain in a hot spot is given by the formula [5] :

$$G_{hs} = 2\gamma_0\sqrt{l_{hs}t/c},$$

where

$$\gamma_0 = (1/4)\sqrt{\omega_0\omega_l I n_e/n_c},$$

is the homogeneous SBS growth rate and l_{hs} is the hot spot length in the direction of the scattered wave propagation,

$$l_{hs} = \min\{l_{\|}, \lambda_0 f/\sin|\theta|\}.$$

Hence the maximum gain in a single hot spot is proportional to the f-number, and for the parameters of our simulations it cannot be much larger than 1. Therefore, one has to consider a collective process of forward SBS, in which the light amplification takes place in a domain larger than a single hot spot.

For a moderate pump intensity of 0.7×10^{15} W/cm^2 (corresponding to an average self-focussing parameter $\langle p_{2D}\rangle = 0.56$), the frequency shift $\langle\omega\rangle$ deviates by up to 30% from the three wave resonance condition result ω_l. The agreement is reasonable between the single scattering analytical predictions and the simulations at early time (until approximately 70 ps), and for scattering angles outside the original divergence of the beam.

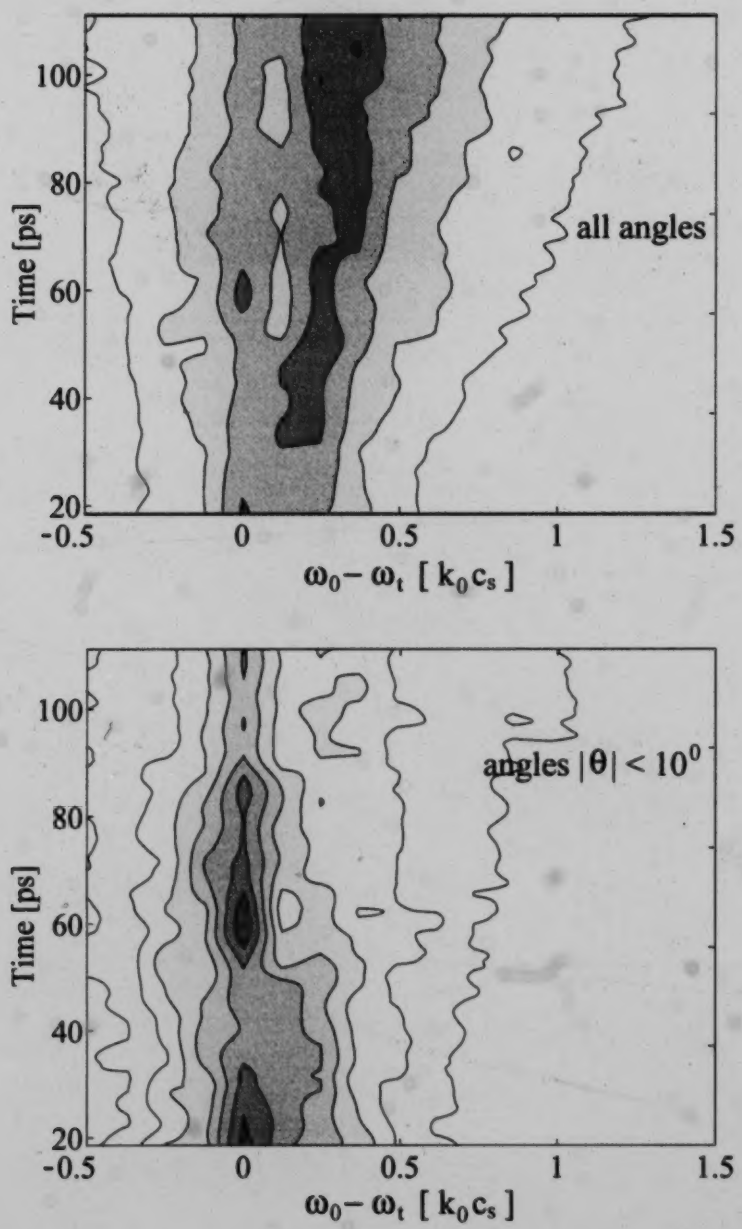

Figure 5.12: The frequency spectrum of transmitted light as a function of time and frequency ω_t for: (a) all scattering angles θ, (b), $|\theta| \leq 10°$. The averaging time interval is 35 ps. The average beam intensity is 0.7×10^{15} W/cm^2.

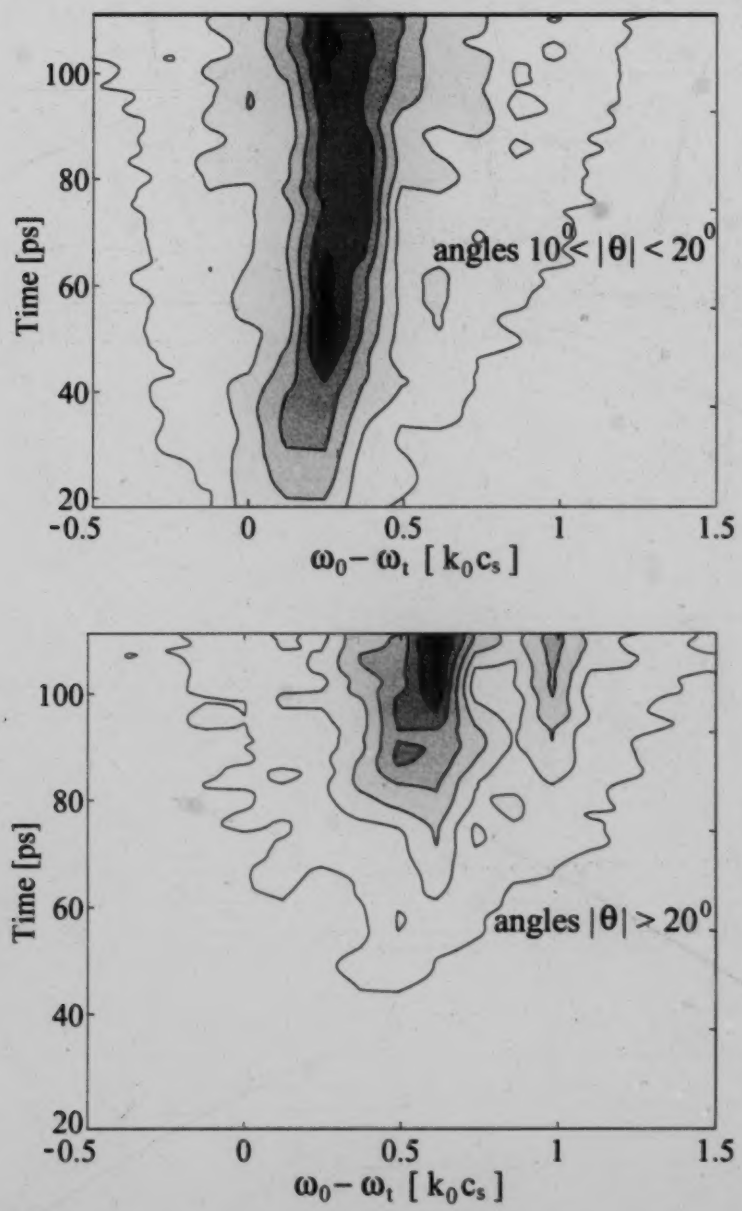

Figure 5.13: The frequency spectrum of transmitted light as a function of time and frequency ω_t for: (c) $10° < |\theta| < 20°$, (d), $|\theta| \geq 20°$. The averaging time interval is 35 ps. The average beam intensity is 0.7×10^{15} W/cm^2.

The frequency shift [cf. Fig. (5.12), (5.13)] becomes noticeably larger at later times (larger than 70 ps), especially for large angles $20° - 25°$. We attribute this result to *multiple* forward SBS. At the time $t > 70$ ps, the light scattered by the primary forward SBS can itself drive a secondary forward SBS wave, as can be seen from Figs. (5.13)(c),(d). In Fig. (5.13)(d) the first maximum (the least red shifted) corresponds to the primary forward SBS with frequency $\omega_l(\theta_1)$, where $\theta_1 \approx (20 - 30°)$. The primary scattered wave has frequency $\approx 0.3k_0c_s$ [cf. Fig.(5.13)(c)]. The secondary ion acoustic wave involved from scattering from the primary scattered wave to secondary scattered wave may have a wave vector $k = (0.6 - 0.7)k_0$ and frequency shift $\omega_l = (0.6 - 0.7)k_0c_s$. Adding up the frequency shift for the primary and the frequency for the secondary ion acoustic waves, gives a frequency shift of about $(0.9 - 1.0)k_0c_s$, consistent with the second maximum in the spectrum of the simulations [cf. Fig.(5.13)(d)]. The second maximum (the most red shifted) results from the secondary forward SBS of the waves primarily scattered in the angular domain $\theta \approx (10° - 20°)$, which is the preferential angular domain where the primary scattered waves are emitted [see Fig. (5.13)(c)].

It is also found that for a beam intensity of 10^{15} W/cm^2, corresponding to a self-focussing parameter $\langle p_{2D} \rangle = 0.8$, the frequency shift of the transmitted light is larger than for the intensity 0.7×10^{15} W/cm^2 [cf. Fig. (5.14)]. This result can also be interpreted in terms of multiple scattering: the forward SBS gain is larger for higher beam intensity, so that the regime of secondary scattering can be reached faster in space (as a function of the longitudinal coordinate x) and in time.

Consequently, based on numerical simulations, we come up to the following scenario: (i) at a time of about $20 - 30$ ps, the instability of filaments give rise, in the front part of the plasma, to non-stationary filamentary structures, which

generate incoherently forward SBS in a broad domain of propagation angles; (ii) these waves, emitted in the front part of the plasma, serve as a seed for an incoherent spatial amplification of forward SBS, which gives rise to an angular and spectral broadening of light during its propagation through the plasma. In particular, it produces red-shifted light, corresponding to propagation angles outside the incident beam cone (in the range $10° - 20°$, see Fig. (5.13)(c)), to the transmitted light. This process depends on time and space the angular and spectral width are increasing functions of time and of the longitudinal coordinate x. In real space, this incoherent spatial amplification changes the speckle size and the correlation time that both decrease with time and with x. This process explains why the effective f-number keeps decreasing with time and x, even in spatial domains where the speckle size is too small for self-focussing to take place. Indeed, the reduction of the hot spot size along the direction of beam propagation implies that the hot spots can self-focus only in the front part of a plasma, where the self-focussing parameter $p_{2D} \sim f^2$ has not decreased significantly. The observation in our simulations that beam spreading continues in the rear part of the plasma, when the self-focussing parameter p_{2D} is smaller than the filament instability threshold, is therefore another indication that it is the collective forward SBS process which is responsible for angular and spectral broadening. In the case of high laser intensities, the scattered waves become unstable with regard to secondary forward SBS.

The frequency spectra of the transmitted light has been studied for various scattering angles in order to distinguish between different processes that can take place in the plasma. At early times, $\sim 20 - 30$ ps, the unshifted component in the frequency spectrum is dominant. This is the time period when the speckle self-focussing takes place. After about 30 ps, the red-shifted component of the frequency spectrum increases rapidly due to forward SBS.

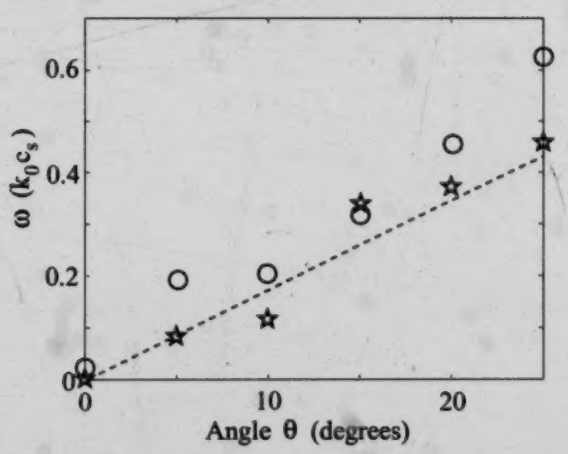

Figure 5.14: Angular dependence of the frequency shift of transmitted light for $P/P_{cr} = 1.2$ and 1.7 compared with the linear theory result $\omega_l(\theta)$ (dashed line).

The frequency spectra integrated over the whole simulation time were used to obtain the dependence of the frequency shift on the propagation angle, $\omega(\theta)$, that is shown in Fig. (5.14). For small incident beam intensities, $P/P_{cr} < 1$, the frequency shift $\omega(\theta)$ is in good agreement with the forward SBS in the regime of weak coupling, $\omega_l(\theta) = 2k_0c_s\sin(\theta/2)$. For larger incident beam intensities, $P/P_{cr} > 1$, the frequency shift of a light scattered outside the focussing cone is up to 1.5 times larger than the forward SBS frequency shift $\omega_l(\theta)$. This feature of the frequency spectra is similar to what is observed in experiment [17].

We interpret the frequency spectra as a signature that RPP beam experiences the instability of high intensity hot spots coupled to the supersonic ion density perturbations [34, 33, 6, 21]. A new fast growing resonant instability of an elementary filament with $P/P_{cr} \gg 1$ has been found recently [21]. This instability is due to the excitation of higher order filament eigenmodes. In our simulations the average power of RPP beam is about critical, but there are some intense hot spots where conditions for the resonant filament instability are sat-

isfied. The instability of high intensity hot spots can generate a broad spectrum of non-stationary density perturbations, that interact with moderate intensity hot spots, thus changing the statistical properties of the whole laser field distribution in the plasma. The growth rate of the resonant filament instability [21] is of the order of $k_0 c_s$, and is larger than the SBS growth rate in the strongly coupled regime. This estimate is consistent with the numerical results for the width $\Delta\omega$ of the frequency spectrum of the transmitted light for different propagation angles θ. The corresponding correlation time $\tau_c = 1/\Delta\omega \sim 0.6$ ps for our parameters.

5.10 Reduction of backward SBS

Plasma induced smoothing results in modification of backward SBS, which gradually decreases in time [cf. solid line in Fig. (5.10)(a) and Figures (5.9)]. This reduction of backward SBS reflectivity is partly due to the speckle size shortening, and partly due to the temporal incoherence. In order to understand the effect of the speckle size, it is sufficient to notice that the backward SBS gain in a single hot spot is proportional to the product of the maximum intensity and the speckle length[23]: $G_b \sim I l_\parallel$. Thus, to maintain a given SBS reflectivity, the laser intensity has to be increased if the speckle length decreases. As the number of speckles having a given intensity I is a decreasing function of I, the total reflectivity is also a decreasing function of the speckle length.

To estimate more precisely the effect of speckle size reduction on the average SBS reflectivity, we follow the arguments developed in Refs. [23, 29] for a RPP beam, and assume that the speckle statistics is approximately Gaussian. In this limit the average reflectivity per unit of length in the direction of beam propagation is given by:

$$\frac{d\langle R\rangle}{dx} = \frac{1}{l_\parallel}\int du\, u\, p(u) R_b(\langle I\rangle u)\,. \tag{5.26}$$

Here $R_b(I)$ is the reflectivity from a single speckle, and $p(u) \sim -dM/dI$ is the intensity probability distribution function. For hot spot statistics close to Gaussian and $u \gg 1$,

$$p(u) = \alpha u^{D/2} \exp(-u),$$

where α is a numerical factor. Following [23], we assume that R_b is an exponential function of the gain, $\epsilon \cdot \exp(G_b)$, for $R < R_{sat}$, and that it saturates at the level $R_{sat} \sim 1$. Since G_b is a linear function of the intensity and of the speckle length, $G_b = u l_{\|}/l_{crit}$, one readily sees from Eq. (5.26) that above the SBS threshold, $l_{\|} > l_{crit}$, the dominant contribution to the average reflectivity comes from the speckles with saturated backward SBS

$$u_m \approx \frac{l_{crit}}{l_{\|}} \ln(R_{sat}/\epsilon).$$

Evaluating the integral in Eq. (5.26) one finds the following formula for the reflectivity per unit length:

$$\frac{d\langle R\rangle}{dx} = \frac{\alpha}{l_{crit} \ln(R_{sat}/\epsilon)} u_m^{D/2+2} \exp(-u_m). \tag{5.27}$$

As the parameter u_m is inversely proportional to the speckle length, the reflectivity per unit length decreases with the decrease of $l_{\|}$ if the inequality $u_m > 2 + d/2$ is satisfied.

For the plasma parameters relevant to our simulations shown in Fig. (5.10), $\epsilon = 10^{-6}$, $R_{sat} \sim 1$, $l_{\|} = 64\lambda_0$, and

$$l_{crit} = 0.8\Gamma_s \sqrt{1 - n_e/n_c}\, \lambda_0 (n_c/n_e\langle I\rangle) \approx 15\lambda_0,$$

and the value of u_m in the front part of plasma $u_m^{front} \approx 3$. The value of u_m in the rear part of plasma increases with time because $u_m \sim 1/f^2$, and at time $\sim 100-130$ ps it reaches $u_m^{rear} \approx 12$. Correspondingly, the effective length for the backward SBS decreases, so that at late time only the front part of the plasma,

within a domain of the order of one Rayleigh length, contributes to backward SBS. For example, in the simulation results shown in Fig. (5.10), the reflectivity at the late time $\sim 100 - 130$ ps is about 2 times smaller than its peak value at the early time (~ 20 ps). The decrease of reflectivity in simulations is consistent with the following formula obtained from Eq. (5.27):

$$\langle R \rangle = \frac{\alpha}{l_{crit} \ln(R_{sat}/\epsilon)} \int_{u_m^{front}}^{u_m^{rear}} du_m \frac{1}{du_m/dx} u_m^{D/2+2} \exp(-u_m) \sim 1/(du_m/dx)|_{u_m = u_m^{front}}, \tag{5.28}$$

where $(du_m/dx)|_{u_m = u_m^{front}}$ increases in time due to the decrease of the speckle length $l_{\parallel}$.

Temporal incoherence is also an efficient mechanism to reduce backward SBS. According to Ref. [3], a correlation time as short as 1 ps is able to reduce the SBS reflectivity by several orders of magnitude. As the plasma induced temporal incoherence takes place in the same spatial domain as the speckle size reduction, we may conclude that after some transient time, backward SBS could develop in the front part of plasma only, due to onset of plasma induced incoherence in the remaining part of the plasma.

Bibliography

[1] R. L. Berger, Phys. Rev. Lett. **65**, 1207 (1990).

[2] S. E. Coe, T. Afsar-rad, M. Desselberger, F. Khattack, O. Willi, A. Giulietti, Z. Q. Lin, W. Yu, and C. Danson, Europhys. Lett. **10**, 31 (1989).

[3] L. Divol and Ph. Mounaix, Phys. Plasmas **6**, 4037 (1999).

[4] V. V. Eliseev, W. Rozmus, V. T. Tikhonchuk, and C. E. Capjack, Phys. Plasmas **3**, 3754 (1996).

[5] V. V. Eliseev, I. Ourdev, W. Rozmus, V. T. Tikhonchuk, C. E. Capjack, and P. E. Young, Phys. Plasmas **4**, 4333 (1997).

[6] V. Eliseev, D. Pesme, W. Rozmus, V. T. Tikhonchuk, and C. E. Capjack, Phys. Scripta **T75**, 112 (1998).

[7] J. Garnier, Phys. Plasmas **6**, 1601 (1999).

[8] P. N. Guzdar, C. S. Liu, and R. H. Lehmberg, Phys.Fluids **B3**, 910 (1993).

[9] S. Hüller, Ph. Mounaix, and V. T. Tikhonchuk, Phys.Plasmas **5**, 2706, 3794 (1998).

[10] Y. Kato and K. Mima, Appl. Phys. B **29**, 186 (1982).

[11] W. L. Kruer, *The Physics of Laser Plasma Interactions*, (Addison-Wesley, New York, 1988).

[12] C. Labaune, H. A. Baldis, B. Cohen, W. Rozmus, S. Depierreux, E. Schifano, B. S. Bauer, and A. Michard, Phys. Plasmas **5**, 2048 (1999).

[13] G. Laval, R. Pellat, D. Pesme, A. Ramani, M. N. Rosenbluth, and E. A. Williams, Phys. Fluids **20**, 2049 (1977).

[14] R. H. Lehmberg, and S. Obenschain, Opt. Commun. **46**, 27 (1983).

[15] R. H. Lehmberg, A. J. Schmitt, and S. E. Bodner, J.Appl.Phys. **62**, 2680 (1987).

[16] C. E. Max, Phys. Fluids **19**, 74 (1976).

[17] J. D. Moody, B. J. MacGowan, S. H. Glenzer, R. K. Kirkwood, W. L. Kruer, A. J. Schmitt, E. A. Williams, and G. F. Stone, Phys. Rev. Lett. **83**, 1783 (1999).

[18] Ph. Mounaix, Phys. Rev. E **52**, R1306 (1995).

[19] D. Pesme, Annual Report CNRS: Interaction Laser Matiere – LULI **29**, 1 (1987), National Technical Information Document No PB92-100312.

[20] D. Pesme, in *La Fusion Thermonucleaire Inertielle par Laser*, edited by R. Dautray and J.-P. Watteau (Eyrolles, Paris, 1993), Vol. 1.

[21] D. Pesme, W. Rozmus, V. T. Tikhonchuk, A. V. Maximov, I. Ourdev, and C. H. Still, Phys. Rev. Lett. **84**, 278 (2000).

[22] H. A. Rose and D. F. DuBois, Phys. Fluids B **5**, 590 (1993).

[23] H. A. Rose and D. F. DuBois, Phys. Rev. Lett. **72**, 2883 (1994).

[24] H. A. Rose, Phys. Plasmas **2**, 2216 (1995).

[25] A. J. Schmitt, Phys. Fluids **31**, 3079 (1988).

[26] A. J. Schmitt and B. B. Afeyan, Phys. Plasmas **5**, 503 (1998).

[27] S. Skupsky, R. W. Short, T. Kessler, R. S. Craxton, S. Letzring, and J. M. Soures, J. Appl. Phys. **66**, 3456 (1989).

[28] J. J. Thomson and J. I. Karush, Phys. Fluids **17**, 1608 (1974).

[29] V. T. Tikhonchuk, Ph. Mounaix, and D. Pesme, Phys. Plasmas **4**, 2658 (1997).

[30] V. T. Tikhonchuk, S. Hüller, and Ph. Mounaix, Phys. Plasmas **4**, 4369 (1997);

[31] R. Y. Chiao, E. Garmire, and C. H. Townes, Phys. Rev. Lett. **13**, 479 (1964).

[32] E. Valeo and C. Oberman, Phys. Rev. Lett. **30**, 1035 (1973).

[33] E. Valeo, Phys. Fluids **17**, 1391 (1974).

[34] V. E. Zakharov and A. M. Rubenchik, Sov. Phys. JETP **38**, 494 (1974).

[35] S. C. Wilks, P. E. Young, J. Hammer, M. Tabak, and W. L. Kruer, Phys. Rev. Lett. **73**, 2994 (1994).

[36] P. E. Young, J. H. Hammer, S. C. Wilks, and W. L. Kruer, Phys. Plasmas **2**, 2825 (1995).

Chapter 6

Two crossed RPP beams

The studies of laser plasma interaction physics in preformed plasmas with crossed beam illumination have two important applications: understanding the potential energy exchange mechanisms between the crossed beams, and providing new insight into the evolution of parametric instabilities under well controlled experimental conditions [2, 15, 12].

Particularly the energy transfer between crossed-beams has received a close attention because it can destroy the carefully designed energy balance between the multiple laser beams in the ICF experiments, thus affecting the symmetry of a pellet illumination [16]. So far, experiments [10, 24] have shown modest energy transfers, in apparent agreement with stationary theory predictions [11]. Kirkwood et al. [10] observed a small energy exchange between two crossed laser beams with different frequencies. The energy transfer was mediated by the resonant ion acoustic wave generated by the optical mixing of the two beams. Wharton et al. [24] obtained similar results to [10] with two equal frequency crossed beams interacting in a flowing plasma. Due to the Doppler shift, the frequency of the ion acoustic wave generated by the beating of the two beams was zero in the laboratory frame, thus allowing for an energy transfer between the beams via the resonant scattering on this ion sound wave.

In this Chapter, we describe numerical simulations motivated by the experi-

mental observations showing a large angular beam spreading, spectral broadening and red shift of the transmitted light for two equal frequency crossed beams interacting at 22.5°. A broad frequency spectrum and large angular spread of the transmitted light have already been observed in single beam interaction experiments [25, 23, 19] and these effects were related to the plasma-induced laser beam smoothing. As we discussed in Chapter 5 the latter involves the self-focusing instability of speckles containing more power than the critical power for self-focusing, and the subsequent dynamical evolution of laser filaments, coupled to forward SBS [20]. In the case of single beam experiments, plasma self-induced smoothing gives rise to angular broadening, spectral broadening and red shift of the transmitted light [22, 17], which have been clearly observed in experiments [13, 25, 23, 19] and described in numerical simulations [7, 22]. In the case of the crossed beam illumination considered here, plasma self-induced smoothing is found, in addition to these single beam effects, to dramatically enhance the large angle forward SBS by which the energy of one beam can be transferred to the other.

The content of this Chapter is organized as follows. In Section 6.1 we describe the set of experiments that formed the basis for our numerical simulations. In section 6.2 we present the model for the crossed laser beams and the typical parameter sets of the simulations. Next, in Section 6.3 we show the time evolution of the system characteristics like beam power and angle between beams for crossed beam with equal intensities. The frequency spectra of the transmitted light is discussed in greater details in Section 6.4 and a close comparison between experiment and simulation is performed. Density fluctuation spectra for the same case are presented in Section 6.5. Section 6.6 contains results for crossed beams with colors in the case of beams with equal intensities and beams with different intensities.

6.1 Crossed beams in experiments

The experiments [13] that were used as a basis for our numerical simulations were carried out on the 6-beam LULI facility at Ecole Polytechnique. Three 0.53 μm beams were used to preform and heat the plasma from a thin exploded plastic foil, two 1.053 μm beams as interaction beams, and one 0.35 μm beam as a probe beam for Thomson scattering diagnostics. The interaction beams (labeled 1 and 2, respectively, in the present text) had identical characteristics. They were focused with $f/6$ lenses through random phase plates, producing a focal spot diameter of 320 μm (containing 62% of the total energy), and maximum average intensity of $8\times10^{13}\mathrm{W/cm^2}$. The angle between the two beams was 22.5°. The main diagnostic of these experiments was a spectrometer coupled with a streak camera providing time-resolved spectra of the light collected along the forward direction of beam 1. The light was collected with an $f/4$ lens, off-axis from beam 1 by 3°. The collected signal included the transmitted light contained within the focusing cone of beam 1, and the forward scattering light with scattering angles extending up to 11° from the beam 1 axis. The spectral and temporal resolutions were $0.5\times10^{-8}cm$ and 20 ps, respectively. Fast photodiodes were used to measure the absolute forward energy.

The plasma was preformed by irradiating a thin micro-disk of plastic with two 0.53 μm beams from each side, 2 ns before the interaction beam arrival. A third 0.53 μm beam was used to heat the plasma before the interaction. The initial foil thickness and laser energies were chosen in such a way that the foil had exploded a short time before the arrival of the interaction beams. The plasma was characterized by monitoring the spatial and temporal evolution of the $5/2\omega$ emission, generated by the 3ω probe beam scattering off the $\omega/2$ plasmon produced by the two plasmon decay of the interaction beam. This harmonic emission provides information on the position of the quarter-critical layer as

a function of time. The electron temperature was measured using Thomson scattering from ion acoustic wave fluctuations without any interaction beams, and was found to be 0.5 keV.

The main diagnostic of these experiments was a spectrometer coupled with a streak camera providing time-resolved spectra of the light collected along the forward direction of beam 1. The light was collected with an $f/4$ lens, off-axis from beam 1 by 3°. The collected signal included the transmitted light contained within the focusing cone of beam 1, and the forward scattering light with scattering angles extending up to 11° from the beam 1 axis. It was checked by using masks that most of the light transmitted in the forward direction of beam 1 was collected this way. The spectral and temporal resolutions were $0.5 \times 10^{-8} cm$ and 20 ps, respectively. Fast photodiodes were used to measure the absolute forward energy.

Figure 6.1 shows time-resolved spectra of the transmitted light collected by the optics located along the direction of beam 1 as described above when both beams, 1 and 2, have equal average intensities. The spectrum is illustrated in more detail by three cross-sections at different times. The first cross-section shows a spectrum containing essentially an unshifted component of the transmitted light. After a transient period there is a sudden onset of a broad red shifted component as shown in cut 2. Cut 3 illustrates an equally broad spectrum at a later time. In both the cases 2 and 3 corresponding to times past the initial transient, the main part of the transmitted signal lies in the red shifted components.

6.2 Pump model

Our simulations are based on the results obtained in Chapter 5 and extend previous crossed Gaussian beam studies [6] to the case of two RPP beams. The

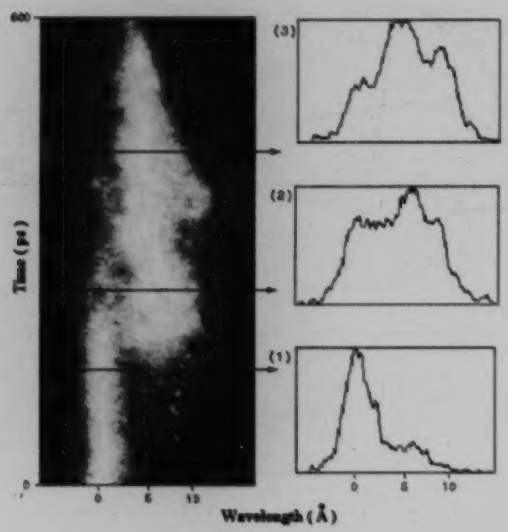

Figure 6.1: Time-resolved spectra of the transmitted light collected in the experiment by the optics located along the direction of beam 1, when both beams, 1 and 2, have equal average intensities.

two incident laser beams are initialized in the plasma at time $T = 0$. Following the experimental setup described in the previous Section, both beams have the same structure of the electric field, [cf.Eq. (6.2)], but different random phase realizations $\phi^{(1,2)}$ [see Fig (6.3)(a) and (b)]. The beams are symmetric with regard to the x-axis and the angle between the axes of the beams was chosen to be $2\alpha = 24^0$. To obtain the structure of the summary field we extend the model developed in Section 5.2 by adding a rotation factor $e^{\pm i\alpha y}$ to the solution to account for the different directions of the crossing beams. The summary field in the focal plane has the form [cf. Eq. (5.11)]:

$$E(y,x) = \sum_{j=1}^{N} A_j(y,x) \left[E_1 e^{i\varphi_j^{(1)}} e^{-i\alpha y} + E_2 e^{i\varphi_j^{(2)}} e^{i\alpha y} \right],$$

where

$$A_j(y,x) = \sqrt{\frac{P_{inc}}{ia_0}} \frac{1}{2\pi} \exp\left\{ -i\theta_j \left(y + \frac{\theta_j}{2} x \right) \right\} \frac{2}{\xi_j} \sin\left(\frac{\pi \xi_j}{N} \right),$$

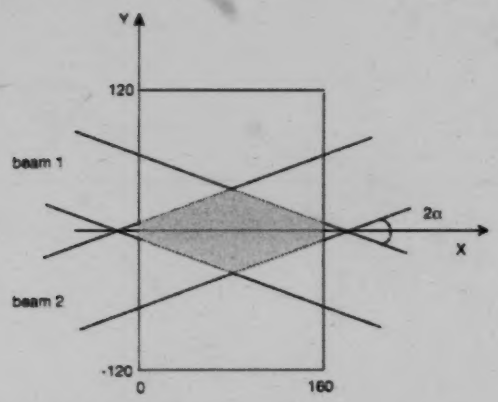

Figure 6.2: Layout of the interaction region between beam 1 and beam 2.

and

$$\xi_j = y + \theta_j x.$$

In the first series of simulations the amplitude coefficient of the primary beam was kept constant $E_1 = 1$, and the relative intensity of the secondary beam varied $E_2 = 0.2, 0.6, 1$.

The boundary conditions are imposed at the left boundary, $x = 0$, and correspond to a sum of two RPP beams focused in the middle of the computational box. The size of the box is 240 × 160 laser wavelengths [cf. Fig.(6.2)]. Figure (6.3) (c, left) shows the intensity cross section at best focus position for the summary beam for the case where each of the constituting beams had $f = 8$. It is clearly seen the effect of the interference leads to a much smaller scale of the perpendicular size of the hot spots. The same holds for their longitudinal size as illustrated by the intensity contour plot on Fig.(6.3) (c, right). The electron temperature, T_e, and electron density, n_e, used in our numerical simulations were: T_e =0.5 keV, n_e =0.3n_c.

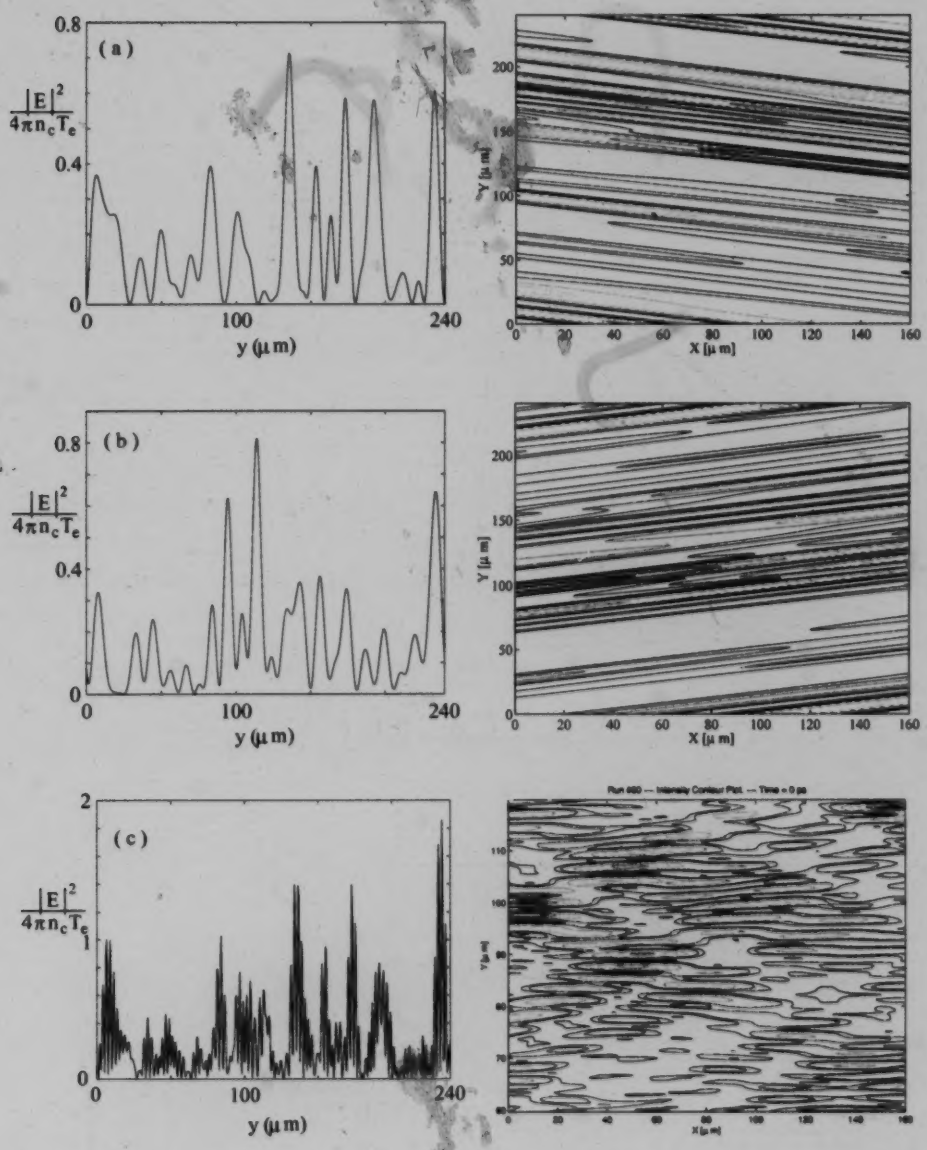

Figure 6.3: Intensity cross sections and the corresponding intensity contour plots of the crossed RPP beams at time $T = 0$ for (a) beam 1, (b) beam 2 and (c) sum of beam 1 plus beam 2.

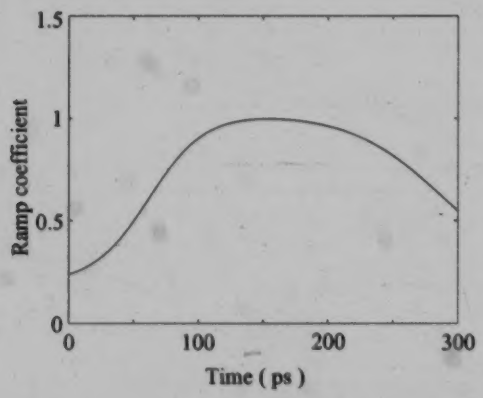

Figure 6.4: Time profile of the laser beam intensity imposed on the left boundary of the computational box, $x = 0$.

6.3 Evolution in time

The simulations were carried out over 300 ps, and they model the central part of the laser pulse duration in the experiments. The laser beam intensities were ramped in time, in order to account for the laser time history. The time profile of the laser pulse was built on the basis of the profiles used in the experiment and is given on Fig.(6.4). The maximum average intensity of each RPP beam was I =5.4 $\times 10^{13}$ W/cm^2 and was reached at time $\sim 170ps$. The very beginning and the very end of the pulse duration was neglected, because the intensity was not high enough ($< 2.6 \times 10^{13} W/cm^2$) to significantly perturb plasma.

Following the diagnostics, developed in the previous Chapters, we calculated the far field brightness distributions in time in forward and backward directions. A typical temporal evolution of the intensity of transmitted and reflected light is shown in Fig.(6.5). The series of time snapshots shows a large angular spreading of the transmitted light for each beam and a virtual disappearance of the reflected part [cf. Fig.(5.9)].

We follow the dynamics of the process by summarizing the snapshots in time

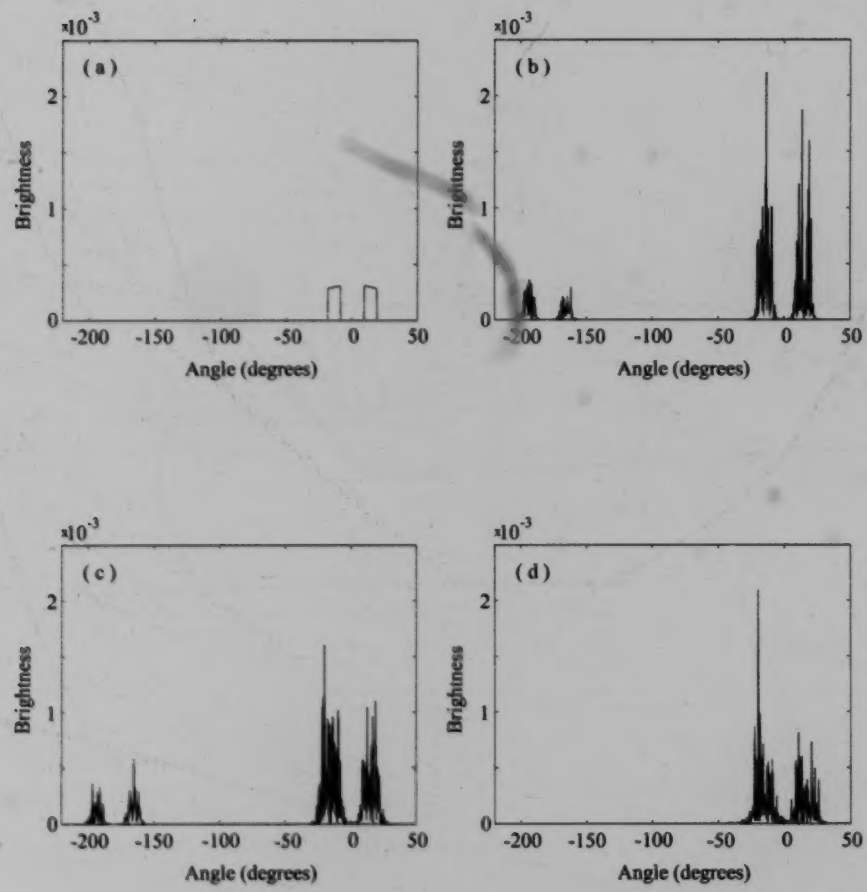

Figure 6.5: Typical evolution of beams spreading in different moments of time: (a) 0ps, (b) 102ps, (c)205ps, (d) 300ps. The two laser beams have equal average beam intensity of $I = 5.4 \times 10^{13} W/cm^2$ and $f = 6$; $n/n_c = 0.3$.

in Fig. (6.6)(a) shows the balance of power between the two crossing beams of the same intensity. One can see that the amount of reflected light decreases after time $\sim 150ps$.

As for the transmitted light, Fig.(6.5) shows the spreading of each of the crossed beams. Fig. (6.6)(c) shows an almost linear increase of the angular width, $\langle\theta\rangle$, of the transmitted light from 7° to 14° (by 7°) that is consistent with the increase of the angle between the beams, if angular spreading of the beams occurs in the outward direction. As before, [cf. Chapter 5] the angular width $\langle\theta\rangle$ is defined as the full width of the central part of the spectrum that contains 76% of the electromagnetic energy. It is equal to the full width half maximum for the equivalent Gaussian distribution. The angular spreading of the crossed beams is a very important feature and it will be discussed to a larger extent in the next Section.

Figure (6.6)(b) shows the angle between the crossing beams as a function of time. The angle between the incident beams is about 25° and the angle between transmitted beams at late time $\sim 300ps$ is about 32°. Comparing angular spreading, Fig.(6.6)(c), and the increase of the angle between beams, Fig.(6.6)(b), one can conclude that beam spreading occurs mainly in outward direction. This corresponds to the results of Chapter 5 that the gain of the forward SBS, Eq. (5.25), is higher for larger wave vectors of ion acoustic waves excited by the RPP beams. In the geometry of two crossed beams, the largest wave vector of ion acoustic waves corresponds to scattering between outward regions of the incident beams.

The next section will show that the red-shifted component in the frequency spectra is mainly due to the light coming from outside the initial beam cone.

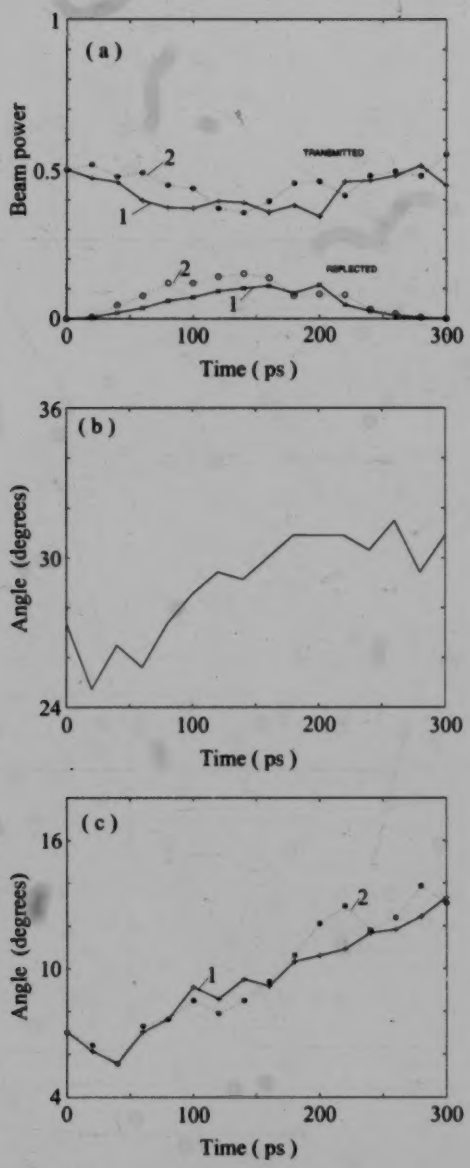

Figure 6.6: Time evolution of crossed beams with equal intensities, (a) transmitted and reflected light for beam 1 (solid line) and beam 2 (dotted line), (b) change of the angle between the beams, (c) beams angular width. The parameters of the run are the same as in Fig. (6.5).

6.4 Frequency spectra of transmitted light

For comparison with the experimental data, we display in Figure 6.8 the overall transmitted light spectra obtained by summing up all the near field spectra corresponding to different directions of propagation within an angle of 180°. The transmitted light is collected along different angles θ in the near-field domain and analyzed spectrally.

The maximum laser intensity is reached in Figs. 6.1 and 6.7 at the moment corresponding approximately to cuts 2. Initially, the main part of the spectrum lies in the unshifted component, as shown in the first cut. The cuts 2 in Figs. 6.1 and 6.7 illustrate the regime taking place just after the sudden onset of the red shifted component. In the simulations the onset of this red shifted component can be clearly identified as occurring at the moment when the average intensity of the beam speckles reaches the critical value for self-focusing. Thus, at this moment of time there is a large number of speckles which are unstable with respect to self-focusing and the subsequent instabilities of light trapped in filaments [20]. The third cut in Fig. 6.7 corresponds to a broad spectrum, in which three distinct peaks can be seen, the total width extending up to $10 \times 10^{-8} cm$ towards the red part of the spectrum.

To achieve a better understanding of the processes involved in crossed beam interactions we compare the transmitted light spectra produced in the crossed beam case with that of a single beam interaction. Frequency spectra of the transmitted light obtained from the simulations for a single beam interaction and the same parameters as in Fig.(6.7) is shown in Fig.(6.8) *.

*Concerning the single beam spectra, some differences can be seen between the simulations [Fig. 6.8] and the experiments [14] results, the latter exhibiting a much broader red shift. Our numerical modeling of the IAW nonlinearity (a simple logarithmic saturation of the density response) cannot properly account for the laser induced flow velocity contributing to the Doppler broadening of the ion waves which scatter the transmitted light. Moreover, we are modeling relatively small plasma ($160 \times 240 \lambda_0$) with constant background conditions. Thus, our hot spot statistics of the interaction region is limited and may exclude significant nonlinear effects [20]

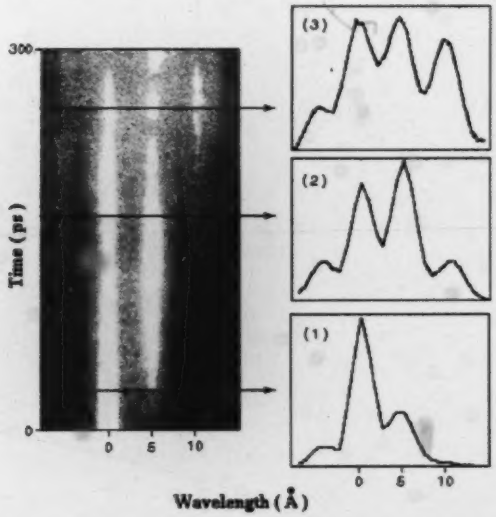

Figure 6.7: Frequency spectra of the transmitted light obtained from the simulations for two equal intensity crossed beams. The parameters of the run are T_e =0.5 keV and n_e =0.3n_c.

We have found in simulations that whenever at least one of the interacting beams has a large red shifted component, it can act as a resonant seed for the large angle forward SBS of the unshifted part of the second beam. Such forward SBS produces intense and broad red-shifted components of the first beam as seen in cuts 2 and 3 of Figs. 6.1 and 6.7.

In the experiments, an increase by a factor 2.3 in the energy of the transmitted light collected by the optics located along the direction of beam 1 has been measured when beam 2 was present. The analysis of the single beam spectrum,Fig. 6.8, shows that this increase is mainly due to the amplification of the red-shifted component of beam 1. As said before, this red shifted component is related to plasma induced beam smoothing. For two incident beams of equal intensity this implies an increase of the overall transmission. Such an increase is

due to very intense hot spots. leading to a less efficient temporal plasma induced smoothing of a single beam in the simulations as compared to the one in the experiments.

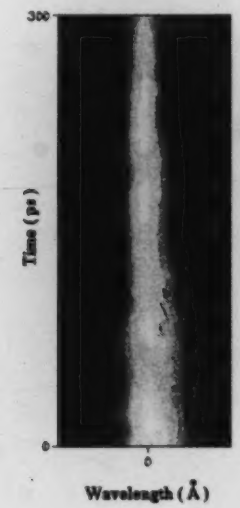

Figure 6.8: Frequency spectra of the transmitted light obtained from the simulations for a single beam interaction and the same parameters as in Fig.(6.7).

partly due to reduced collisional absorption because of the higher temperatures obtained with crossed beam irradiation, and partly due to smaller backward SBS during the late stages of the interaction, as discussed further on. The enhancement of the red-shifted component as a function of the two beam characteristics is further discussed for crossed beams with different wavelengths in Section 6.6 .

The simulations show very clearly that the presence of the second beam increases the energy which is scattered outside the solid angle of beam 1, supporting the interpretation that the red-shifted component is mainly due to the light coming outside this beam cone. This result was confirmed in the experiment [14], using complementary masks on the transmitted light diagnostic. The near field spectra in the case of a single beam interaction indeed shows that spectral broadening associated with a plasma induced smoothing is important for directions corresponding to transmission outside the incident cone only. Thus the forward SBS of the unshifted part of beam 2 can be seeded only by these red

shifted components of beam 1 which propagate outside the incident cone of beam 1. For this reason, the near field diagnostics in the case of two beam illumination shows that the transfer of energy between the beams involves forward SBS at approximately 30°, which would lead to a frequency shift of $\approx 3 \times 10^{-8} cm$ according to the linear matching conditions for forward SBS. This linear estimate is of the same order in magnitude as the observed red shifts. The difference can be attributed to the intricate interplay between the plasma induced smoothing effects on each of the interaction beams and the large angle forward SBS taking place between them. The excellent agreement between the simulations and the experiments represents an additional argument in favor of our interpretation, i.e. the red shifted component of a single beam spectrum appears indeed to be sufficiently broad to act as an efficient seed for large angle SBS, in spite of weaker plasma induced smoothing effects in the one beam simulations than in the experiments.

6.5 Density fluctuation spectra

The result of plasma induced smoothing effects can be further investigated on the imprint they leave in plasma density fluctuations. Figure (6.9) shows the Fourier spectra of density fluctuations corresponding to two different times.

The Fourier spectra of density fluctuations shown in Fig. (6.9)(a) correspond to the earlier time associated with cuts 1 of Figs.(6.1) and (6.7). For small values of k_x, they display the three distinct components corresponding to the stationary density perturbations produced by the optical mixing of two top hat RPP beams [21]. The temporal ramping of the laser intensity has eliminated the initial transient effects [18, 9] of the IAW excitation which would be generated by an instantaneous turn on of the laser ponderomotive force in simulations. The transmitted light has already been broadened in angle but no additional

frequency components are observed at that time in the frequency spectrum [cf. Figs. (6.1) and (6.7)]. The components of the ion wave spectrum in Fig. (6.9)(a) at $k_x \approx 2k_0$ are associated to backward SBS along the directions of each beam, and to the stimulated scattering of one beam into the backward direction of the other - the so called symmetric mode ($k_y = 0$) [5] which has been identified before by Thomson scattering in Ref. [2].

At the later time corresponding to the cuts 3 in Figs. (6.1) and (6.7), Fig. (6.9)(b) shows that the three small k_x-components are now significantly broadened in comparison with that of Fig. (6.9)(a). This broadening is the result of plasma self-induced smoothing effects for the two spectral components corresponding to the optical mixing of the interacting RPP beams, and of large angle forward SBS for the central part of the small k_x-spectrum. At the same time the backward SBS driven fluctuations are dramatically reduced. Such an effect has been observed experimentally before [2]. We interpret it as resulting from the enhancement of the bandwidth and angular spread of the forward propagating light, leading to a reduction of the backward SBS gain coefficient [17]. Suppression of backward SBS was explained in Refs. [3, 4] as due to the IAW nonlinearity. The latter mechanism is likely to be more important for plasma densities lower than the one considered here, as plasma induced beam smoothing is less effective for low plasma density.

6.6 Crossed beams with different wavelengths

Studying crossed beams with different wavelengths was motivated by the fact that the interaction between the two beams via ion acoustic waves should be enhanced if the frequency mismatch between the beams is in the range of the frequency of the IAW involved in this interaction. Before going into a discussion of the interactions of beams with different frequencies let's give a brief account of

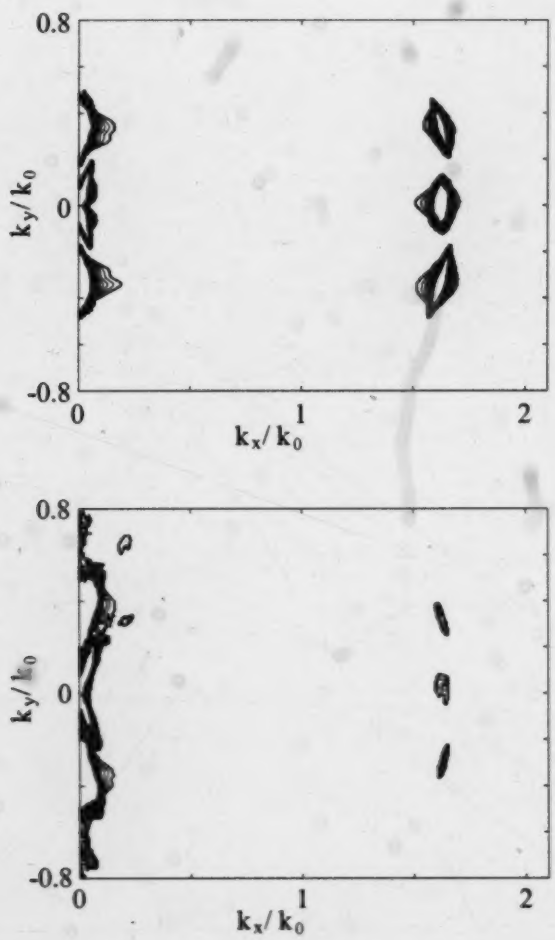

Figure 6.9: Density fluctuation spectra at early time (a) corresponding to the moment of time of cuts 1 in Figs. (6.1) and (6.7). (b) corresponds to the late time moment of cuts 3 in the same figures.

a set of simulations, where we varied the relative intensities between the beams. First, we have observed that the enhancement factor depends on the intensity of beam 2 : with beam 1 at its maximum intensity 8×10^{13} W/cm^2, this factor was 2.1 and 3.5 for beam 2 at 2.4×10^{13} W/cm^2 and 8×10^{13} W/cm^2, respectively. This increase was found to be associated with an increase of the overall intensity of the red-shifted component. The enhancement factor depends also on the intensity of beam 1. At low intensity of beam 1, the enhancement factor was larger than at high intensity: for beam 2 at its maximum intensity 8×10^{13} W/cm^2, this factor was 8 for beam 1 at 2×10^{13} W/cm^2 and 3.5 for beam 1 at 8×10^{13} W/cm^2, showing the saturation of the mechanism. These features were also confirmed experimentally. The transfer of energy can be identified as taking place between the spectrally unshifted component of one beam and the red shifted part of the other. We observed also that the transfer of energy between the beams mediated by the mechanism described above results in the equilibration of their energy fluxes.

6.6.1 Beams with equal intensities

Fig.(6.10) shows the time evolution of crossed beams in the case when both beams have the same intensities but the frequency of beam 1 is $0.6k_0c_s$ smaller than the frequency of beam 2. Such a frequency mismatch is consistent with the frequency of the ion acoustic waves excited by the interaction of two beams with an angle of $25 - 35°$ between them [cf. Fig.(6.10)(b)]. The incident beam $f_\#$ =6, ratio of $P/P_{cr} = 1.2$ From Fig. (6.10)(a), which illustrates the balance of power between the two crossed beams, one can see that at early time (up to 70ps) the beam with lower frequency is increasing in intensity whereas the beam with larger frequency is decreasing in intensity. After time about 150ps, the intensities of both transmitted beams are close to the same value.

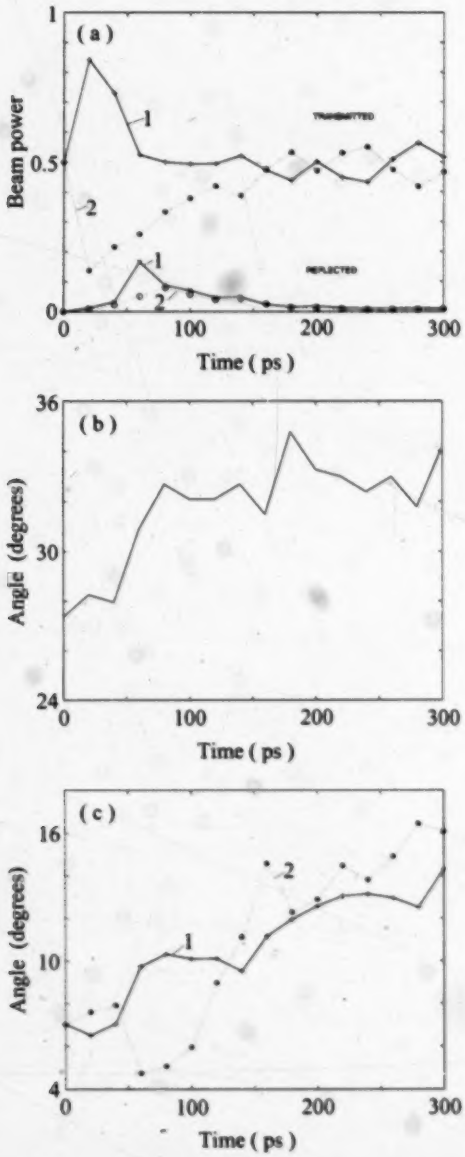

Figure 6.10: Time evolution of crossed beams with equal intensities and different frequencies, (a) transmitted and reflected light for beam 1 (solid line and beam 2 (dotted line), (b) change of the angle between the beams, (c) beams angular width. The parameters of the run are the same as in Fig. (6.5) the frequency of beam 1 is 0.6 of the frequency of beam 2.

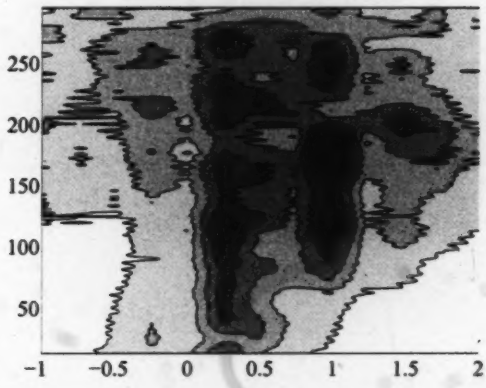

Figure 6.11: Frequency spectrum of the transmitted light in the case of crossed beams with equal intensities and $\omega_1 = 0.6\omega_2$.

The dependence of the angle between the beams with color as a function of time is given in Fig. (6.10)(b) and is similar to the case of beams with equal frequencies Fig.(6.6)(b). Namely the angle between the beams increases by about 7° during the simulation time. We define the center of the angular spectrum of a beam as an angular position for which half of the beam energy is to the left and the other half is to the right.

The angular width of the beam with colors is shown in Fig.(6.10)(c). One can see than at time interval between 50ps and 100ps, the angular width of the beam with lower frequency is larger than the width of the beam with higher frequency. At the same time the intensity of the beam with lower frequency is much larger that the intensity of the beam with higher frequency [see Fig.(6.6)].

Figure (6.11) shows the frequency spectra of the transmitted light from the two crossed beams with colors. The zero frequency in the spectrum corresponds to the average between the frequencies of the beam. Therefore the beam with lower frequency corresponds to $\omega = 0.3$ and the beam with higher frequency corresponds to frequency $\omega = -0.3$. The asymmetry toward the positive ω of the frequency spectra, illustrates the energy transfer from the beam with higher

frequency to the one with lower frequency. The frequency spectrum in the case of crossed beams with colors, Fig. (6.11), is more red-shifted and broader than the frequency spectrum from the crossed beams with the equal frequencies [cf. Fig. (6.7)].

6.6.2 Beams with different intensities

Let us now consider the case when the intensity of beam 1 (the one with lower frequency) is 10 times smaller than the intensity of beam 2 (the one with higher frequency). The f-number of the incident beam is 4, and the ratio of $P/P_{cr} = 0.8$ for the beam with higher intensity.

Fig.(6.12)(a) shows that energy is transferred from the beam with higher frequency (dotted line in Fig. (6.12)) to the beam with lower frequency (solid line in Fig. (6.12)). Only at late times ($\sim 250ps$) are the intensities of the transmitted beams are similar.

The angle between the two beams is shown in Fig.(6.12)(b) and its increase with time is much slower than the angle between the beam with equal intensities [see Fig. (6.10)(b)].

The width of both beams Fig. (6.12)(c) does not change as much as in the case when beams have the same intensity [see Fig. (6.10)(c)].

The frequency spectrum in the case of beams with colors, having different intensities, Fig. (6.13), is not as broad as the frequency spectrum in Fig. (6.11) since P/P_{cr} for Fig. (6.13) is smaller than that one for Fig. (6.11). Therefore the plasma smoothing effects are less pronounced.

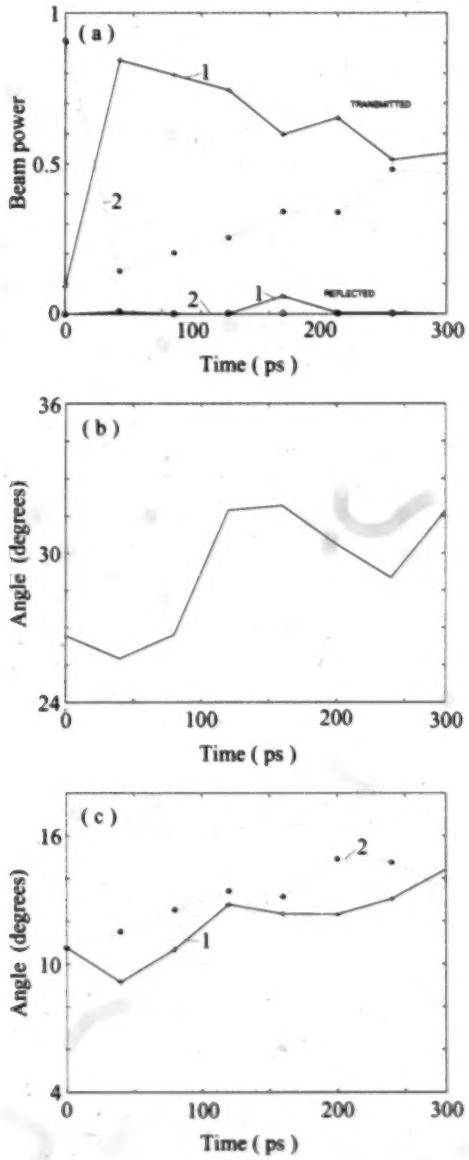

Figure 6.12: Time evolution of crossed beams with different frequencies. (a) transmitted and reflected light for beam 1 (solid line and beam 2 (dotted line), (b) change of the angle between the beams, (c) beams angular width. The parameters of the run are $I_1 = 2 \times 10^{14} W/cm^2$, $I_2 = 0.1 I_1$, $f = 4$, $n/n_c = 0.1$, $\omega_1 = 0.6\omega_2$.

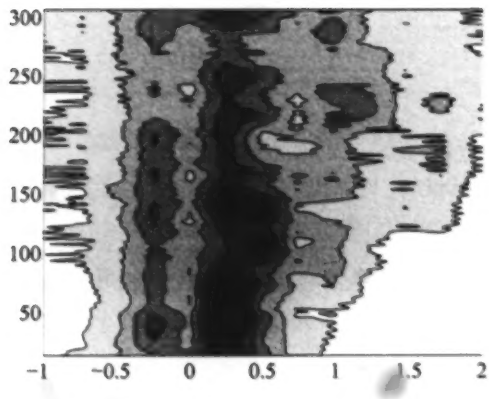

Figure 6.13: Frequency spectrum of the transmitted light for the case of beams with different intensities and different frequencies. The parameters of the run are as in Fig. (6.12).

Bibliography

[1] M. R. Amin, D. E. Capjack, P. Frycz, W. Rozmus, and V. T. Tikhonchuk, Phys. Fluids B, **5** (1993) 3748.

[2] H. A. Baldis, C. Labaune, E. Schifano, N. Renard, and A. Michard, Phys. Rev. Lett. **77**, 2957 (1996).

[3] B. I. Cohen B. F. Lasinski, A. B. Langdon, E. A. Williams, H. A. Baldis and C. Labaune, Phys. Plasmas **5**, 3402 (1998).

[4] B. I. Cohen B. F. Lasinski, A. B. Langdon, E. A. Williams, K. A. Wharton, R. K. Kirkwood, and K. G. Estabrook, Phys. Plasmas **5**, 3408 (1998).

[5] D. F. DuBois, B. Bezzerides, and H. A. Rose, Phys. Fluids **4**, 241 (1992).

[6] V.V. Eliseev, W. Rozmus, V.T. Tikhonchuk, C.E. Capjack, Phys. Plasmas **3**, 2215 (1996).

[7] V. V. Eliseev, I. Ourdev, W. Rozmus, V. T. Tikhonchuk, C. E. Capjack, and P. E. Young, Phys. Plasmas **4**, 4333 (1997).

[8] V. Eliseev, D. Pesme, W. Rozmus, V. T. Tikhonchuk, and C. E. Capjack, Phys. Scripta **T75**, 112 (1998).

[9] R. E. Giacone, C. J. McKinstrie, and T. Kolber, Phys. Plasmas **6**, 3587 (1999).

[10] R. K. Kirkwood, B. B. Afeyan, W. L. Kruer, B. J. MacGowan, J. D. Moody, D. S. Montgomery, D. M. Pennington, T. L. Weiland and S. C. Wilks, Phys. Rev. Lett. **76**, 2065 (1996).

[11] W. L. Kruer, S. C. Wilks, B. B. Afeyan, and R. K. Kirkwood, Phys. Plasmas **3**, 382 (1996).

[12] C. Labaune, H. A. Baldis, B. S. Bauer, E. Schifano, and B. I. Cohen, Phys. Rev. Lett. **82**, 3613 (1999).

[13] C. Labaune, H. A. Baldis, B. I. Cohen, W. Rozmus, S. Depierreux, E. Schifano, B. S. Bauer, and A. Michard, Phys. Plasmas **6**, 2048 (1999).

[14] C. Labaune, H. A. Baldis, E. Schifano, B. S. Bauer, A. Maximov, I. Ourdev, W. Rozmus, and D. Pesme, Phys. Rev. Lett. **85**, 1658 (2000).

[15] A. K. Lal, K. A. Marsh, C. E. Clayton, G. Joshi, C. J. McKinstrie, J. S. Li, T. W. Johnston, Phys. Rev. Lett. **78**, 670 (1997).

[16] W. L. Lindl, Phys. Plasmas **2**, 3933 (1995).

[17] A. V. Maximov, I. Ourdev, D. Pesme, W. Rozmus, and V. T. Tikhonchuk, Phys. of Plasmas **8**, 1319 (2001).

[18] C.J. McKinstrie, J.S. Li, R.E. Giacone, and H.X. Vu, Phys. Plasmas **3**, 2686 (1996).

[19] J. D. Moody, B. J. MacGowan, S. H. Glenzer, R. K. Kirkwood, W. L. Kruer, A. J. Schmitt, E. A. Williams, and G. F. Stone, Phys. Rev. Lett. **83**, 1783 (1999).

[20] D. Pesme, W. Rozmus, V. T. Tikhonchuk, A. V. Maximov, I. Ourdev, and C. H. Still, Phys. Rev. Lett. **84**, 278 (2000).

[21] H. A. Rose and S. Ghosal, Phys. Plasmas **5**, 1461 (1998).

[22] A. J. Schmitt, and B.B. Afeyan, Phys. Plasmas **5**, 503 (1998).

[23] S. C. Wilks, P. E. Young, J. Hammer, M. Tabak, and W. L. Kruer, Phys. Rev. Lett. **73**, 2994 (1994).

[24] K. B. Wharton, R.K. Kirkwood, S. H. Glenzer, K. G. Estabrook, B. B. Afeyan, B. I. Cohen, J. D. Moody, and C. Joshi, Phys. Rev. Lett. **81**, 2248 (1998).

[25] P. E. Young, J. H. Hammer, S. C. Wilks, and W. L. Kruer, Phys. Plasmas **2**, 2825 (1995).

Chapter 7

Summary and conclusions

We have presented numerical and theoretical studies of different laser beam interactions with underdense plasmas involving ion wave instabilities. Our investigations have been motivated and guided by experimental results where intense laser pulses interact with exploding foil plasmas. For the experimental parameters, our 2D simulations displayed results consistent with the observations, particularly in relation to the angular spread and spectral distribution of the transmitted light. We have emphasized the important role of near-forward and backward SBS, which coexist with filamentation and self-focussing instabilities.

The simulations considered a homogeneous plasma with a longitudinal dimension of $L_x = 160\mu m$. This length corresponds to the scale lengths typical of the experimental velocity and density gradients. The non-paraxiality of our model has allowed for a unique study of the interaction between different ion wave instabilities. The interplay between self-focussing, filamentation and SBS constitutes an important component of our results.

We studied these instabilities for three different classes of laser beam intensity profiles, namely single non-Gaussian speckle, single RPP beam and two crossed RPP beams. For all the cases we established a close correspondence between the simulations and experimental results.

The actual scenario of the ion response depends on the intensity distribution

of the laser pump. For the case of *single non-Gaussian speckle*, Chapter 4, we have carefully matched the experimental intensity profiles at the best focus position by using the superposition of two Gaussian beams with different f-numbers. The existence of a narrow Gaussian leads to SFI of the central portion of the laser pump, while the broader part of the laser pump support the FI and near-forward SBS. The self-focussing of the narrow part of the laser beam develops on a relatively fast time scale and produces density perturbations, which in turn seed the FI of the broader part of the beam.

We found that the backscattered SBS develops first and becomes localized in the front part of the interaction region close to the laser entrance boundary. In our simulations, in order to control the backward SBS reflectivity at the reasonable levels corresponding to the experimental data, we impose a relatively high damping for the sound waves produced by backward SBS at $2k_0$. The strong damping approximately replaces the effects of inhomogeneous plasma flow and nonlinear evolution of IAW. The backward reflectivity determines the laser power reaching the rear part of the target. The ion acoustic waves produced by filamentation, self-focussing or near-forward SBS are damped by Landau and collisional damping.

The seeding of transversely propagating sound waves by self-focussing of the narrow parts of Gaussian beams increases amplification of the filamentation instability. The FI can then compete with the near-forward SBS. We have examined these two processes by using linear theory. We have shown that the FI can be effective during the initial time evolution. However, on the time scale defined by an experimental pulse duration ($\sim 100ps$) near-forward SBS will dominate. We certainly found strong indications from our numerical results that SBS controls the characteristic properties of the transmitted light. After accounting for the non-linear broadening of the laser pump due to self-focussing, the FI and

the sound wave propagation, we obtained a good agreement between theory and simulations. We provided convincing evidence for near-forward SBS by demonstrating a spectral shift of the transmitted light along different directions, which is in good agreement with weakly coupled SBS theory. We also demonstrated an increasing angular spreading of the light produced by the near-forward SBS with increasing plasma density of laser plasma intensity.

One of the most interesting results in this case was the development of the angular and spectral spreading of the transmitted light due to plasma instabilities, such as filamentation, self-focussing and near-forward SBS [cf. Fig.(4.13)]. As we pointed out, this effect can increase plasma induced smoothing of the laser beams and increase the threshold for scattering instabilities deeper in the target, thus reducing their detrimental effect in fusion scale experiments. This is an important result, since the nonlinear evolution of randomized laser beams in laser produced plasmas is an ongoing concern in the inertial confinement fusion studies and in other applications of intense laser pulses including x-ray sources and laser particle accelerators. Different beam smoothing techniques have been designed to improve uniformity of plasma illumination. All of them involve a random phase plate, which breaks laser beam into many independent beamlets whose interference pattern in the laser focal spot creates an ensemble of statistically independent speckles. This improves uniformity of the intensity pattern, however, as we showed, within the speckle distribution there is always a significant number of hot spots with large intensity, many times above the average value. These intense hot spots give rise to nonlinear effects, which can alter properties of laser beams at the macroscopic level.

Thus, as a part of our investigation of a single speckle evolution, we considered the stability of laser light filaments in a homogeneous isothermal plasma with respect to coupled electromagnetic and density perturbations [cf. Chapter 3].

The speckle evolution is usually studied on the basis of the stationary approximation described by the nonlinear Schrödinger (NLS) equation. The speckle evolves into a filament by forming elongated density channel with a trapped light propagating along its axis, if the laser light power in the speckle is above the critical value for self-focussing. An equilibrium state of a nonlinear filament corresponds to a balance between light ponderomotive and plasma pressures. The validity of the stationary approximation is limited by the filament modulational instability, which develops on a long ion-acoustic time scale and involves relatively long wavelength spatial perturbations. It involves dynamical ion wave response and an absolute growth in time. However, recent studies have shown the total destruction of a single nonlinear filament on a very short time scale.

We have explained the filament destruction by a new kind of a parametric interaction, called resonant instability of nonlinear filaments, in which a fundamental waveguide mode of a trapped electromagnetic radiation is coupled to the next excited state in the waveguide. This coupling involves a supersonic density response and displays similarities to the strongly driven forward stimulated Brillouin scattering. However, we found that contrary to the forward SBS of plane waves or broad laser beams, the scattering in a filament is characterized by a narrow maximum in the growth rate as a function of the wave number. This maximum reaches values comparable with the growth rate of backscattered SBS. This well defined resonant wave number of the perturbation enables identification of the instability in simulations and allows experimental verification.

The resonance filament instability is important for the randomized laser beams. It might repeat itself many times in different locations if the laser beam duration is much longer than the filament formation time. The secondary filament formation and its subsequent instability has been observed in the simulations $10 - 20$ ps after the primary filament explosion. The secondary filament

has smaller size and contains less power due to the dephasing effect of remaining density fluctuations. As we showed later, Chapter 5, in the case of RPP beam the repeating resonance filament instability decrease the speckle size i.e. the effective f-number of the laser beam.

The sensitivity of the resonance instability on the plasma channel depth also offers a possibility to control it with the laser beam temporal smoothing technique. The instability could be suppressed if the beam coherence time is less than the time of filament formation. This effect has been also seen in simulations and experiments. Finally, the filament instability also has a significant effect on the backscattering parametric instabilities by diminishing the size of interaction region and the effective pump wave intensity.

The second part of the thesis concentrates on studying *spatially incoherent laser beams* in the regime where the average beam power in a speckle is approaching the self-focussing critical power. Such beams are widely used in laser-plasma experiments because of their capability to control the light intensity distribution and to potentially suppress parametric instabilities.

As we have shown in the first part of the thesis, a laser beam propagating in an underdense plasma develops angular spreading and spectral broadening with a shift toward longer wavelengths. Similar plasma induced angular spreading and red shift have been observed in experiments and are particularly pronounced for RPP beams. These results were explained in terms of forward SBS and filamentation instabilities. Numerical studies with RPP laser beams have shown that both angular divergence and temporal bandwidth of the transmitted light are larger that those of the incident light in the regimes where filamentation does not reach a steady state. We characterize quantitatively this ability of an underdense plasma to induce a temporal incoherence together with additional spatial incoherence to a propagating laser beam.

We interpreted the spectral broadening and red shift of the transmitted light as a result of multiple near-forward stimulated Brillouin scattering of the propagating laser beam. We also observed new features of SBS due to the mutual influence of forward and backward SBS. The changes in the characteristics of the transmitted light : angular spreading and decrease of time correlation quantify the results of self-induced smoothing of the beam in plasma. We showed that the modification of the transmitted light is due to changes in the hot spot ensemble in plasma. The angular and spectral broadening of the laser beam can be related to spatial and temporal statistical characteristics of the laser field. In order to characterize the spatial incoherence of the propagating beam, we demonstrated that both the longitudinal, $l_{\parallel}$, and transverse, $l_{\perp}$, speckle sizes decrease as the beam propagates through the plasma, while the ratio $l_{\parallel}/l_{\perp}^2$ does not change significantly in space and in time. In addition, the angular width $\langle\theta\rangle$ of the transmitted light was found to satisfy the standard relation of diffraction optics, $\langle\theta\rangle \sim 1/l_{\perp}$. These results made it possible to define a local (in space and time) f-number of the laser beam.

We analyzed the angle correlation function of the transmitted light. We found that the plasma induced spatial incoherence results in an angle correlation function similar to the correlation function of a RPP beam characterized by the effective f-number. We have also analyzed the plasma induced temporal incoherence. We found that the temporal correlation function is similar to that of a laser beam characterized by induced spatial incoherence, in the sense that it quickly decays with the time difference of its arguments.

In addition to the quantitative characterization of the plasma induced smoothing, we also suggested an interpretation of its origin. Our overall picture is the following: in the regime where the average power in a speckle approaches the self-focussing threshold, non-stationary filamentary structures form in the front

part of the plasma. The high-intensity filaments are unstable. The instability, the temporal growth rate of which is characteristic of the so-called strong coupling regime, corresponds to forward SBS growing inside the cavity formed by the density depletion associated with the filament. By contrast with forward SBS, backward SBS may grow in individual speckles. As a result of the onset of plasma induced smoothing in the main part of the plasma, the growth of backward SBS in individual speckles becomes, after the transient period of time, restricted to the plasma front part only. The resonant instability of filaments gives rise, in the front part of the plasma, to scattered waves, temporally incoherent and characterized by a large spectral red shift and a broad angular distribution. They can then be spatially amplified during their propagation through the plasma by the forward SBS instability, in the so-called "incoherent" regime of three-wave coupling. This incoherent spatial amplification involves a spatial domain larger than the size of a single hot spot. In Fourier space, it gives rise to an increase of the angular width and to the spectral broadening while propagating further inside the plasma. In real space, it results in speckle size and correlation time both decreasing with the longitudinal coordinate.

The ability of the plasma to introduce additional incoherence to a propagating laser beam has important implications concerning the growth of backscattering instabilities. As we showed, the additional spatial incoherence is able by itself to reduce backward instabilities, because the gain factor is smaller in the shorter speckles. We also demonstrated that even a small level of temporal incoherence is able to dramatically reduce the backscatter instabilities.

The third part of the thesis concentrates on the effects of the plasma-induced laser beam smoothing in the case of *two crossed spatially incoherent laser beams.*

The nonlinear enhancement of large angle forward scattering of two identical laser beams crossing in a preformed plasma has been observed experimentally

[Chapter 6]. The spectral analysis of the forward scattered light shows two components, one which is unshifted with respect to the initial laser light frequency, and the other which is red-shifted by a few Angstroms. We found that the red-shifted component is strongly enhanced in the case of crossed beam interaction in comparison with that of one beam illumination. The numerical simulations showed that this enhancement is due to large angle forward stimulated Brillouin scattering in which each beam serves as as seed for the forward scattering of the other.

As we saw in the case of single beam interactions, plasma induced smoothing gives rise to angular broadening, spectral broadening and red shift of the transmitted light. It involves the self-focussing instability of speckles containing more power than the critical power for self-focussing, and the subsequent dynamical evolution of laser filaments, coupled to forward SBS. In the case of the crossed beam illumination we found, plasma induced smoothing, in addition to these single beam effects, to dramatically enhance the large angle forward SBS by which the energy of one beam can be transferred to the other. It is an important feature, since the energy transfer between crossed-beams can destroy the carefully designed energy balance between the multiple laser beams in the inertial confinement fusion experiments, thus affecting the symmetry of a pellet illumination.

Using spectral analysis we show that initially, the main part of the spectrum lies in the unshifted component of the transmitted light. The onset of this red shifted component can be clearly identified as occurring at the moment when the average intensity of the beam speckles reaches the critical value for self-focussing. Thus, at this moment of time there is a large number of speckles which are unstable with respect to self-focussing and the subsequent instabilities of a light trapped in a filament. It is important to notice that it is approximately

at the same moment of time that a broad red shifted component appears in the single beam spectra.

We have found that whenever at least one of the interacting beams has a large red shifted component, it can act as a resonant seed for the large angle forward SBS of the unshifted part of the second beam. Such a forward SBS produces intense and broad red-shifted components of the first beam. This leads to an increase of the energy of the transmitted light of beam 1 when beam 2 is present. The spectral analysis confirms that this increase is mainly due to the amplification of the red-shifted component of beam 1. For two incident beams of equal intensity this implies an increase of the overall transmission. Such an increase is partly due to reduced collisional absorption because of the higher temperatures obtained with crossed beam irradiation, and partly due to smaller backward SBS during the late stages of the interaction.

We studied the enhancement of the red-shifted component as a function of the two beam characteristics. First, we have observed that the enhancement factor depends on the intensity of beam 2. We associated this increase with an increase of the overall intensity of the red-shifted component. The enhancement factor depends also on the intensity of beam 1. The enhancement factor was larger for a low intensity of beam 1 than the one with a higher intensity. We identified that the transfer of energy was taking place between the spectrally unshifted component of one beam and the red shifted part of the other.

We have observed that the presence of the second beam increases the energy which is scattered outside the solid angle of beam 1, and that the red-shifted component is mainly due to the light coming outside this beam cone. The near field spectra in the case of a single beam interaction show indeed that the spectral broadening associated with a plasma induced smoothing is important for directions corresponding to a transmission outside the incident cone only. Thus

the forward SBS of the unshifted part of beam 2 can be seeded only by these red shifted components of beam 1 which propagate outside the incident cone of beam 1.

Considering the fourier spectra of density fluctuations, we find that they display three distinct components corresponding to the stationary density perturbations, which get significantly broadened in comparison at later times. This broadening is a result of plasma induced smoothing effects for the two spectral components corresponding to the optical mixing of the interacting RPP beams, and of large angle forward SBS for the central part of the small k_x-spectrum. At the same time the backward SBS driven fluctuations are dramatically reduced, that was already observed in the case of a single speckle. We interpret it as resulting from the enhancement of the bandwidth and angular spread of the forward propagating light, leading to a reduction of the backward SBS gain coefficient. Suppression of backward SBS is explained as due to the IAW nonlinearity and is likely to be more important for plasma densities lower than the one considered here, as plasma induced beam smoothing is less effective for low plasma density.

A comparison with the single RPP case indicated that the crossed beam geometry irradiation makes plasma induced smoothing more efficient in reducing the backward SBS reflectivity.

In conclusion, we studied the plasma induced smoothing effects for beams with increasing complexity – single hot spot beam, single RPP beam and two crossed RPP beams. We demonstrated the effectiveness of the approach to controlling the growth of resonant parametric instabilities of the decay type by reducing the coherence of the pump wave. Such a control of the growth of the scattering instabilities is of fundamental importance for the concept of laser fusion and is going to be one of the essential elements for the success of the laser fusion program.